



**AFRL-AFOSR-VA-TR-2016-0380**

---

Flame Dynamics and Chemistry in LRE Combustion Instability

**Chung Law**  
**TRUSTEES OF PRINCETON UNIVERSITY**  
**1 NASSAU HALL**  
**PRINCETON, NJ 08544-0001**

---

**12/28/2016**  
**Final Report**

**DISTRIBUTION A: Distribution approved for public release.**

Air Force Research Laboratory  
AF Office Of Scientific Research (AFOSR)/RTA1

**REPORT DOCUMENTATION PAGE**

*Form Approved  
OMB No. 0704-0188*

The public reporting burden for this collection of information is estimated to average 1 hour per response, including the time for reviewing instructions, searching existing data sources, gathering and maintaining the data needed, and completing and reviewing the collection of information. Send comments regarding this burden estimate or any other aspect of this collection of information, including suggestions for reducing the burden, to Department of Defense, Washington Headquarters Services, Directorate for Information Operations and Reports (0704-0188), 1215 Jefferson Davis Highway, Suite 1204, Arlington, VA 22202-4302. Respondents should be aware that notwithstanding any other provision of law, no person shall be subject to any penalty for failing to comply with a collection of information if it does not display a currently valid OMB control number.

**PLEASE DO NOT RETURN YOUR FORM TO THE ABOVE ADDRESS.**

<b>1. REPORT DATE (DD-MM-YYYY)</b> 12/22/2016	<b>2. REPORT TYPE</b> Final	<b>3. DATES COVERED (From - To)</b> 09/01/2015-08/31/2016
--	--------------------------------	--

<b>4. TITLE AND SUBTITLE</b> Flame Dynamics and Chemistry in LRE Combustion Instability	<b>5a. CONTRACT NUMBER</b>
	<b>5b. GRANT NUMBER</b> FA9550-15-1-0338
	<b>5c. PROGRAM ELEMENT NUMBER</b>

<b>6. AUTHOR(S)</b> Chung K Law	<b>5d. PROJECT NUMBER</b>
	<b>5e. TASK NUMBER</b>
	<b>5f. WORK UNIT NUMBER</b>

<b>7. PERFORMING ORGANIZATION NAME(S) AND ADDRESS(ES)</b> The Trustees of Princeton University 87 Prospect Street Princeton, NJ 08544-2020	<b>8. PERFORMING ORGANIZATION REPORT NUMBER</b> AWD1004672
---	---

<b>9. SPONSORING/MONITORING AGENCY NAME(S) AND ADDRESS(ES)</b> Joyce A Burch AF Office of Scientific Research 875 N. Randolph Street - Room 3112 Arlington, VA 22203 Phone: 703/696-9729 Email: joyce.burch@us.af.mil	<b>10. SPONSOR/MONITOR'S ACRONYM(S)</b> AFOSR
	<b>11. SPONSOR/MONITOR'S REPORT NUMBER(S)</b>

**12. DISTRIBUTION/AVAILABILITY STATEMENT**  
DISTRIBUTION A: Distribution approved for public release.

**13. SUPPLEMENTARY NOTES**

**14. ABSTRACT**

**15. SUBJECT TERMS**  
Flame stabilization, auto-ignition, cool flames, tribrachial flames

<b>16. SECURITY CLASSIFICATION OF:</b>			<b>17. LIMITATION OF ABSTRACT</b>	<b>18. NUMBER OF PAGES</b>	<b>19a. NAME OF RESPONSIBLE PERSON</b>
<b>a. REPORT</b>	<b>b. ABSTRACT</b>	<b>c. THIS PAGE</b>			Chung K Law
			UU		<b>19b. TELEPHONE NUMBER (Include area code)</b> 609-258-5271

## INSTRUCTIONS FOR COMPLETING SF 298

**1. REPORT DATE.** Full publication date, including day, month, if available. Must cite at least the year and be Year 2000 compliant, e.g. 30-06-1998; xx-06-1998; xx-xx-1998.

**2. REPORT TYPE.** State the type of report, such as final, technical, interim, memorandum, master's thesis, progress, quarterly, research, special, group study, etc.

**3. DATE COVERED.** Indicate the time during which the work was performed and the report was written, e.g., Jun 1997 - Jun 1998; 1-10 Jun 1996; May - Nov 1998; Nov 1998.

**4. TITLE.** Enter title and subtitle with volume number and part number, if applicable. On classified documents, enter the title classification in parentheses.

**5a. CONTRACT NUMBER.** Enter all contract numbers as they appear in the report, e.g. F33315-86-C-5169.

**5b. GRANT NUMBER.** Enter all grant numbers as they appear in the report. e.g. AFOSR-82-1234.

**5c. PROGRAM ELEMENT NUMBER.** Enter all program element numbers as they appear in the report, e.g. 61101A.

**5e. TASK NUMBER.** Enter all task numbers as they appear in the report, e.g. 05; RF0330201; T4112.

**5f. WORK UNIT NUMBER.** Enter all work unit numbers as they appear in the report, e.g. 001; AFAPL30480105.

**6. AUTHOR(S).** Enter name(s) of person(s) responsible for writing the report, performing the research, or credited with the content of the report. The form of entry is the last name, first name, middle initial, and additional qualifiers separated by commas, e.g. Smith, Richard, J, Jr.

**7. PERFORMING ORGANIZATION NAME(S) AND ADDRESS(ES).** Self-explanatory.

**8. PERFORMING ORGANIZATION REPORT NUMBER.** Enter all unique alphanumeric report numbers assigned by the performing organization, e.g. BRL-1234; AFWL-TR-85-4017-Vol-21-PT-2.

**9. SPONSORING/MONITORING AGENCY NAME(S) AND ADDRESS(ES).** Enter the name and address of the organization(s) financially responsible for and monitoring the work.

**10. SPONSOR/MONITOR'S ACRONYM(S).** Enter, if available, e.g. BRL, ARDEC, NADC.

**11. SPONSOR/MONITOR'S REPORT NUMBER(S).** Enter report number as assigned by the sponsoring/monitoring agency, if available, e.g. BRL-TR-829; -215.

**12. DISTRIBUTION/AVAILABILITY STATEMENT.** Use agency-mandated availability statements to indicate the public availability or distribution limitations of the report. If additional limitations/ restrictions or special markings are indicated, follow agency authorization procedures, e.g. RD/FRD, PROPIN, ITAR, etc. Include copyright information.

**13. SUPPLEMENTARY NOTES.** Enter information not included elsewhere such as: prepared in cooperation with; translation of; report supersedes; old edition number, etc.

**14. ABSTRACT.** A brief (approximately 200 words) factual summary of the most significant information.

**15. SUBJECT TERMS.** Key words or phrases identifying major concepts in the report.

**16. SECURITY CLASSIFICATION.** Enter security classification in accordance with security classification regulations, e.g. U, C, S, etc. If this form contains classified information, stamp classification level on the top and bottom of this page.

**17. LIMITATION OF ABSTRACT.** This block must be completed to assign a distribution limitation to the abstract. Enter UU (Unclassified Unlimited) or SAR (Same as Report). An entry in this block is necessary if the abstract is to be limited.

Final Technical Report for AFOSR Grant No.:

FA9550-15-1-0338

**Flame Dynamics and Chemistry in LRE Combustion Instability**

Submitted by

Chung K. Law

Robert H. Goddard Professor

Department of Mechanical and Aerospace Engineering

Princeton University

For Consideration by

Dr. Mitat Birkan

Air Force Office of Scientific Research

December 15, 2016

## Overview

Nonpremixed jet flames have been extensively studied to understand the combustion processes in rocket engines. The stabilization and structure of jet flames determine the lift-off height of the flame and are therefore integral to engine design. In view of the nonpremixed nature of the fuel and oxidizer jets, there are two dominant modes of flame stabilization. The traditional view is that mixing between the two jets will eventually lead to a region of strong reactivity and hence auto-ignition. An alternate view, advanced recently and for largely non-autoignitive situations, is stabilization through the so-called tribrachial flame (also known as triple flame), in which a lean and a rich premixed flame wing with a trailing diffusion flame branch. The point where the three branches intersect, the triple point, is considered to be the stabilization point. The dynamic balance between the local flame propagation speed and the incoming flow speed is the stabilization mechanism.

Regardless of the mechanisms, assessment of flame stabilization must necessarily include the simultaneous and coupled considerations of the fluid flow in the combustion chamber, the mixing between the fuel and oxidizer jets, and the chemistry and dynamics either of the mixing layer or of the flame. In response to these considerations, a comprehensive research program comprised of experiment, computation and theory, has been conducted, yielding both qualitative understanding and quantitative data on the various issues of interest.

## Research Accomplishments

Broadly, the research has been conducted along two thrusts, namely: (1) the dynamics of flame stabilization in environments of various thermodynamic and dynamics characterizations, and (2) the chemistry and dynamics of strained flames, particularly those involving the cool flame, NTC (negative temperature coefficient) chemistry, noting that interests in cool flame chemistry and dynamics have been a major activity in recent fundamental combustion research. Highlights of the accomplishments are summarized next. A total of six papers reporting the work were published in leading journals, and are appended herein.

### 1. Dynamics of Flame Stabilization

1.1 Stabilization of nonpremixed coflow flames: The structure and stabilization mechanism of laminar nonpremixed autoignitive DME/air coflow flames were investigated. Computations were performed at 30 atmospheres with uniform inlet velocities of 3.2 m/s for both streams, and the coflow air boundary temperatures were 700, 800, 900, and 1100 K. The heat release rate and species profiles were examined for each case. Further investigation with Chemical Explosive Mode Analysis (CEMA) and Lagrangian Flamelet Analysis (LFA) were performed to identify the controlling chemistry and elucidate the dominant combustion mode and stabilization mechanism. At 700 - 900 K, autoignition was observed to be the dominant stabilization mechanism, and NTC chemistry determines the stabilization point in mixture fraction space. Conversely, at 1100 K, the kinematic balance between the premixed flame propagation velocity and the incoming flow velocity becomes the dominant stabilization mechanism, and the classical triple flame structure was observed. Extended stabilization regimes, in terms of increasing boundary temperature, are therefore identified, including frozen flow, kinetically stabilized, autoignition-propagation-coupled stabilized, kinematically stabilized, and burner stabilized regimes.

This work is reported in Publication #1: "Autoignition-affected stabilization of laminar nonpremixed DME/air coflow flames," by Sili Deng, Peng Zhao, Michael E. Mueller and Chung K. Law, *Combustion and Flame*, Vol. 162, pp. 3437-3445 (2015).

1.2 Dependence of Stabilization on Pressure and Co-flow Temperature: The structure and stabilization mechanism of the nonpremixed autoignitive coflow flames in 1.1 was investigated at elevated temperatures and pressures. Computations with detailed chemistry were performed at 30 atm with uniform inlet velocities imposed for both streams. The heat release rate profiles were first examined for each case to demonstrate a multibrachial thermal structure. Species concentrations and temperature were sampled along mixture fraction iso-contours, and CEMA was performed to identify the controlling chemistry at representative points. One-dimensional LFA was also performed and compared with the two-dimensional computations to elucidate the relative importance of diffusion processes parallel and normal to the mixture fraction gradient. Various coflow temperatures with different inlet velocities are examined to elucidate their influences on the multibrachial structure as well as the stabilization mechanism. NTC-affected inhomogeneous autoignition and the coupled effects with premixed flame propagation on stabilization are further studied. It is found that, at high coflow boundary temperatures or low inlet velocities, the classical tribrachial flame structure is achieved, and autoignition contributes less to the stabilization due to reduced heat and radical accumulation. The kinematic balance between the local flow speed and flame propagation speed is found to be the dominant stabilization mechanism. On the contrary, kinetic stabilization is achieved at lower coflow temperatures or higher inlet velocities as autoignition becomes dominant. Due to the transition of the dominant chemical pathways during autoignition, the kinetically stabilized structure is usually multibrachial. The transition of different stabilization mechanisms can be made by changing either the boundary velocity or temperature of the coflow. Based on these results, a regime diagram is constructed that identifies the possible stabilization regimes: blowout, kinetically stabilized, autoignition-propagation-coupled stabilized, kinematically stabilized, and burner stabilized.

This work is reported in Publication #2: "Stabilization of laminar nonpremixed DME/air coflow flames at elevated temperatures and pressures," by Sili Deng, Peng Zhao, Michael E. Mueller and Chung K. Law, *Combustion and Flame*, Vol. 162, pp. 4471-4478 (2015).

1.3 Stabilization in Oscillating Flows: The above study was then extended to stabilization in flows with sinusoidally oscillating inlet velocities in order to identify effects of oscillation frequency on the flame dynamics. To benchmark the unsteady cases, a normalized displacement velocity was defined to differentiate flame propagation from autoignition, and this definition was validated against the steady cases. In the oscillating reacting flow, transition between a multibrachial autoignition front and a tribrachial flame occurs periodically. However, unlike the harmonic velocity oscillation, the combustion mode transition is hysteretic. The oscillation cycle starts with the largest inlet velocity, with the multibrachial thermal structure, located downstream, being governed by autoignition chemistry. As flow velocity decreases, the autoignition front moves upstream and transitions to a tribrachial flame near the lower velocity limit, similar to the steady flow, as autoignition chemistry becomes weaker with decreasing upstream residence time. As the flow velocity increases again, the tribrachial flame is convected downstream and, ultimately, due to the radical and heat accumulation in time, autoignition eventually occurs and becomes the dominant pathway. The finite induction time for autoignition results in the hysteretic behavior during the decreasing- and increasing-velocity cycles. The hysteresis diminishes at lower oscillation frequency as there is more time for chemistry to respond to the hydrodynamic changes and consequently approach steady state. At the relatively low oscillation frequencies investigated, first-stage NTC chemistry is less affected by flow dynamics with only second-stage autoignition and flame chemistry, which accounts for the majority heat release, coupled with the flow oscillation.

This work is reported in Publication #3: "Flame dynamics in oscillating flows under autoignitive conditions," by Sili Deng, Peng Zhao, Michael E. Mueller and Chung K. Law, *Combustion and Flame*, Vol. 168, pp. 75-82 (2016).

1.4 Analysis of Stabilization of Triple Flame in Oscillating Flows: Combustion instability of a lifted triple flame downstream of the injector nozzle in an acoustic field is studied. The analysis is focused on the premixed flame segment, and is based on the linear equation for a perturbed flamefront. Assuming that the radius of the flamefront curvature is much larger than that of the internal flame structure, the premixed front is approximated as being quasi-planar. Both acoustic stabilization of the hydrodynamic flame instability and excitation of the parametric instability by sound waves are considered, and the limitation for stable/unstable regimes as a function of flame parameters and acoustic frequency/intensity is determined. The velocity-wise nature of the sound is scrutinized, namely, the acoustics are imitated by a pocket of harmonic flow oscillations. First, the Landau limit of infinitely thin flames is employed. Then the formulation is extended to account for the finite flame thickness, and it is demonstrated how unstable regimes are modified by the flame thickness.

This work is reported in Publication #4. "Coupling of harmonic flow oscillations to combustion instability in premixed segments of triple flames," by V'yacheslav Akkerman and Chung K. Law, *Combustion and Flame*, Vol. 172, pp. 342-348 (2016).

## 2. Cool Flame Chemistry in Flame Stabilization

2.1 Existence and Propagation of Premixed Cool Flames: Cool flames, being essential features of chemical kinetics of large hydrocarbon fuels, are closely related to the negative temperature coefficient phenomenon and engine knock. In this work, the coupling of cool flame chemistry and convective-diffusive transport is computationally and experimentally investigated. A 1-D planar premixed cool flame induced by a hot pocket is first simulated for DME/O<sub>2</sub>/N<sub>2</sub> mixtures with detailed chemistry and transport, demonstrating the existence of a residence time window for quasi-steady propagation. Then with residence time limited by aerodynamic straining, a steady-state premixed cool flame is simulated in a counterflow of heated N<sub>2</sub> against a DME/O<sub>2</sub>/N<sub>2</sub> mixture. It is found that with a high strain rate, corresponding to short residence time, low-temperature heat release is suppressed, resulting in a stretched low-temperature S-curve system response; and that with a sufficiently low strain rate, corresponding to long residence time, ignition induced by low-temperature chemistry would transition to a high-temperature, intensely burning flame. Consequently, a steady-state premixed cool flame exists only for residence time in a strain rate window. A symmetric counterflow configuration is then simulated to determine the cool flame temperature and flame speed at a fixed local strain rate, showing very different controlling chemistry and characteristics as compared to the normal laminar flames governed by high-temperature chemistry. In a companion experimental investigation, premixed cool flames in the counterflow were observed with a high-sensitivity CCD camera in the UV spectrum, with/without a bandpass filter corresponding to the characteristic wavelength of excited HCHO. The chemiluminescence from the cool flame is found to become more intense with increasing equivalence ratio, even for rich mixtures, while the position of the cool flame is insensitive to variation in the equivalence ratio at the same strain rate. These observations qualitatively agree with the numerical simulations, demonstrating the essential features of premixed cool flames.

This work is reported in Publication #5: "Initiation and propagation of laminar premixed cool flames," by Peng Zhao, Wenkai Liang, Sili Deng and Chung K. Law, *Fuel*, Vol. 166, pp. 477-487 (2016).

2.2 Ignition and Extinction of Nonpremixed Cool Flames: Following 2.1, and recognizing that the low-temperature chemical kinetics is promoted at elevated pressures, the ignition and extinction of nonpremixed cool flames at elevated pressures were experimentally and computationally investigated in the counterflow. Specifically, the hysteretic ignition and extinction behavior of the nonpremixed cool flame was for the first time observed and quantified. S-curve analysis was conducted to demonstrate the thermal and chemical structure of the cool flame and to elucidate the dominant chemical pathways

during the ignition and extinction processes. The dominant low-temperature chemical reactions shift from those responsible for radical runaway to exothermic reactions that sustain the cool flame. Increasing the ambient pressure and/or the oxygen concentration in the oxidizer stream promotes the heat release from the cool flame, and hence results in an extended hysteresis temperature window between ignition and extinction. It is further noted that while the observed cool flame ignition temperatures were well predicted by computation, significant discrepancies existed for the extinction temperatures based on the well-adopted reaction mechanism used.

This work is reported in Publication #6: "Ignition and extinction of strained nonpremixed cool flames at elevated pressures," by Sili Deng, Dong Han and Chung K. Law, *Combustion and Flame*, Vol. 176, pp. 143-150 (2017).

### Appendix: Reprints of Journal Papers Published under Sponsorship of the Program

1. "Autoignition-affected stabilization of laminar nonpremixed DME/air coflow flames," by Sili Deng, Peng Zhao, Michael E. Mueller and Chung K. Law, *Combustion and Flame*, Vol. 162, pp. 3437-3445 (2015).
2. "Stabilization of laminar nonpremixed DME/air coflow flames at elevated temperatures and pressures," by Sili Deng, Peng Zhao, Michael E. Mueller and Chung K. Law, *Combustion and Flame*, Vol. 162, pp. 4471-4478 (2015).
3. "Flame dynamics in oscillating flows under autoignitive conditions," by Sili Deng, Peng Zhao, Michael E. Mueller and Chung K. Law, *Combustion and Flame*, Vol. 168, pp. 75-82 (2016).
4. "Coupling of harmonic flow oscillations to combustion instability in premixed segments of triple flames," by V'yacheslav Akkerman and Chung K. Law, *Combustion and Flame*, Vol. 172, pp. 342-348 (2016).
5. "Initiation and propagation of laminar premixed cool flames," by Peng Zhao, Wenkai Liang, Sili Deng and Chung K. Law, *Fuel*, Vol. 166, pp. 477-487 (2016).
6. "Ignition and extinction of strained nonpremixed cool flames at elevated pressures," by Sili Deng, Dong Han and Chung K. Law, *Combustion and Flame*, Vol. 176, pp. 143-150 (2017).



# Autoignition-affected stabilization of laminar nonpremixed DME/air coflow flames



Sili Deng, Peng Zhao, Michael E. Mueller\*, Chung K. Law

Department of Mechanical and Aerospace Engineering, Princeton University, Princeton, NJ 08544, USA

## ARTICLE INFO

### Article history:

Received 20 December 2014

Received in revised form 3 June 2015

Accepted 7 June 2015

Available online 19 June 2015

### Keywords:

Stabilization

Nonpremixed coflow flame

Autoignition

Negative temperature coefficient (NTC)

Dimethyl ether (DME)

## ABSTRACT

The structure and stabilization mechanism of laminar nonpremixed autoignitive DME/air coflow flames were investigated. Computations were performed at 30 atmospheres with uniform inlet velocities of 3.2 m/s for both streams, and the coflow air boundary temperatures were 700, 800, 900, and 1100 K. The heat release rate and species profiles were examined for each case. Further investigation with Chemical Explosive Mode Analysis (CEMA) and Lagrangian Flamelet Analysis (LFA) were performed to identify the controlling chemistry and elucidate the dominant combustion mode and stabilization mechanism. At 700–900 K, autoignition was observed to be the dominant stabilization mechanism, and NTC chemistry determines the stabilization point in mixture fraction space. Conversely, at 1100 K, the kinematic balance between the premixed flame propagation velocity and the incoming flow velocity becomes the dominant stabilization mechanism, and the classical triple flame structure was observed. Extended stabilization regimes, in terms of increasing boundary temperature, are therefore identified, including frozen flow, kinetically stabilized, autoignition–propagation-coupled stabilized, kinematically stabilized, and burner stabilized regimes.

© 2015 The Combustion Institute. Published by Elsevier Inc. All rights reserved.

## 1. Introduction

Nonpremixed jet flames have been extensively studied to understand the combustion processes in rocket and diesel engines. The stabilization and structure of jet flames determine the lift-off height of the flame and are therefore integral to engine design. Due to the mixing process of the fuel and oxidizer streams in lifted flames at nonautoignitive conditions, the combustion mode is partially premixed, leading to the observation of a two-dimensional tribrachial flame (also known as triple flame) [1]; specifically, a lean and a rich premixed flame wing with a trailing diffusion flame branch. The point where the three branches intersect is called the triple point and is generally considered to be the stabilization point for nonautoignitive situations. The dynamic balance between the local flame propagation speed and the incoming flow speed is characterized as the stabilization mechanism. A recent review by Chung [2] discussed the stabilization, propagation, and instability of tribrachial flames, including the effects of concentration gradient [3–5], velocity gradient [6], and burned gas expansion [7–10]. These studies, however, were limited to nonautoignitive conditions, but real engines are operated at elevated pressures and

temperatures, where autoignition is activated and could interact with the tribrachial flame.

Chung and co-workers [11–13] further conducted a series of experiments to investigate the autoignition characteristics of laminar  $C_1$  to  $C_4$  fuel jets in a heated air coflow and found that, above certain coflow temperatures, lifted flames could be established through autoignition. In these studies, both the tribrachial structure for most autoignited cases and a repetitive behavior of extinction and reignition at the critical condition near blowout were observed. However, the role that autoignition plays in the stabilization mechanism as well as its influences on the tribrachial flame structure are still less understood.

Furthermore, practical hydrocarbon-based fuels generally have two-stage ignition processes, in which the first stage ignition is governed by low temperature chemistry and the second stage ignition by high temperature chemistry. In both low and high temperature regimes, the ignition delay time decreases as the initial temperature increases. However, in the intermediate temperature regime, the transition of the ignition chemistry results in increased overall ignition delay time as the initial temperature increases, exhibiting the negative temperature coefficient (NTC) phenomena, which has been extensively studied in homogeneous systems as a major feature of large hydrocarbon autoignition [14]. For engine applications, however, the coupling between NTC chemistry and transport processes should be considered, for nonuniformities

\* Corresponding author.

E-mail address: [muellerm@princeton.edu](mailto:muellerm@princeton.edu) (M.E. Mueller).

invariably exist in realistic combustion systems. When the transport time scale becomes comparable to that of the NTC chemical time scale, the two processes are expected to be strongly coupled. As a consequence, the global response of the inhomogeneous system can also be affected by NTC chemistry. Recently, a series of computational and experimental studies adopting the non-premixed counterflow configuration by Law and co-workers [15–17] have demonstrated that, with the existence of nonuniformities in the flow, species, and temperature fields, the ignition characteristics of nonpremixed flames can be fundamentally affected by NTC effects, especially at elevated pressures and/or reduced strain rates.

Therefore, NTC-affected stabilization of nonpremixed lifted jet flames can be potentially important, yet few literatures provide detailed analysis. Krisman et al. [18] recently conducted a numerical study of dimethyl ether (DME)/air mixing layer at 40 atmospheres and air coflow temperatures ranging from 700 to 1500 K and observed multibrachial structures in the heat release rate profiles. The mixture fractions corresponding to the stabilization points defined based on the hydroxyl radical (OH) mass fraction and the first stage autoignition kernels based on the methoxymethylperoxy radical ( $\text{CH}_3\text{OCH}_2\text{O}_2$ ) were compared with the most reactive mixture fractions computed from homogeneous autoignition under the same initial conditions. A transport budget analysis based on selected species was performed to differentiate deflagration from autoignition.

In light of the reported multibrachial structure, showing a modified flame shape from autoignition in the mixing layer, further investigation is warranted to identify the detailed chemical structure and stabilization mechanism of the multibrachial flame. For example, tools for computational diagnostics, especially for identifying locally dominant chemical reactions, can be employed to understand the controlling chemistry. Moreover, a direct comparison to homogeneous autoignition is insufficient to understand the transport processes in the current configuration. In the two-dimensional mixing layer, transport processes in two directions are important: parallel and normal to the mixture fraction gradient, which are due to transverse stratification of temperature and species and streamwise flow and (flame back) diffusion, respectively. These considerations would significantly improve the understanding of the role of autoignition upstream of the flame structure and quantitatively identify the controlling kinetics and stabilization mechanism.

In the present study, nonpremixed DME/air coflow flames were computed at 30 atmospheres with the oxidizer stream heated to activate autoignition. With fixed inlet velocities, only the oxidizer stream boundary temperature was varied to investigate the corresponding lifted flame morphology, chemical structure, and dominant reaction pathways. In the following we shall first present the computational details of the study. The thermal and chemical structures are then described with heat release rate and selected species profiles in Section 3. The evolution of the controlling chemical pathways are subsequently identified with Chemical Explosive Mode Analysis (CEMA) and the stabilization mechanism determined with Lagrangian Flamelet Analysis (LFA) in Section 4. Finally, the transition of the dominant stabilization mechanism is analyzed in Section 5, with extended stabilization regimes constructed for completeness.

## 2. Computational details

The flow configuration is an axisymmetric DME stream at 300 K in a heated coflow of air (700, 800, 900, and 1100 K) at 30 atmospheres. The fuel nozzle diameter  $D$  is 0.8 mm, and the fuel and air are initially separated with an adiabatic, no-slip wall with thickness  $D/20$ . The coflow outer boundary is specified as an

adiabatic slip wall, and its diameter is large enough such that increasing the width of the domain does not influence the computation. Uniform inlet velocities of 3.2 m/s were specified for both fuel and air streams and kept the same for all the cases to establish lifted flames. For the unsteady establishment of the flame, a convective outflow is utilized at the outlet boundary, which simplifies to a Neumann condition for the steady problem.

The flow field was initialized on a coarse mesh within a large domain. At first, all the chemical source terms were set to zero until the nonreacting flow reached steady-state. Chemical source terms were then activated; the mixture autoignited; and the flow field reached steady-state. The domain was then truncated, and the mesh was refined to fully resolve the chemical structure. All the results presented in the present work were obtained from the steady-state solutions.

The Navier–Stokes equation with buoyancy in the streamwise direction and the conservation equations of mass, species, and energy were solved. The species diffusivities were determined from a constant, nonunity Lewis number. The Lewis numbers for individual species (summarized in the [Supplementary Data](#)) were pre-calculated from a one-dimensional flamelet with the same boundary conditions and the mixture-averaged transport model and evaluated at the maximum temperature location. The conserved scalar mixture fraction  $Z$  was specified as unity and zero for the fuel jet and coflow at the inlet, respectively, and computed by solving its transport equation with unity Lewis number [19]. This definition of mixture fraction is consistent with the one used in the flamelet calculation in Section 4.2.

Dimethyl ether was chosen in this work, for it is a clean biofuel and one of the smallest hydrocarbons exhibiting NTC behavior. Detailed reaction models for low and high temperature DME oxidation [20–23] have been developed and validated in burner-stabilized flames [24], nonpremixed counterflow ignition [25], and laminar flame speeds [26]. The present computations were conducted using a skeletal mechanism of 39 species [27], including both low and high temperature oxidation pathways, which was reduced from the well validated detailed mechanism of Zhao et al. [23].

The low-Mach number formulation of the governing equations is solved using NGA, which is based on the numerical methods of Desjardins et al. [28]. The momentum and scalar equations are discretized with a second-order centered scheme and a third-order WENO scheme [29], respectively, on a staggered mesh. The iterative second-order semi-implicit Crank–Nicolson scheme of Pierce and Moin [30] is adopted for temporal integration. At each time step, the chemical source terms for the species and energy equations are evaluated independently from the transport terms using the CVODE package [31].

Uniform grids in the axial direction were adopted for the computations, and the grid spacing was set as  $\Delta x = 2.2 \mu\text{m}$ . A nonuniform grid was used in the radial direction with a minimum spacing of  $2.5 \mu\text{m}$  to resolve the mixing layer corresponding to the separation wall and geometric progression stretch rates less than 3% towards both the centerline and the outer boundary. The dimensions of and number of grid points in the computational domain for each computation are summarized in [Table 1](#).

**Table 1**  
Computational domain and number of grid points.

Coflow temperature [K]	700	800	900	1100
$L_x$ [mm]	28	7	3.5	3
$L_r$ [mm]	6	3.9	3.9	6
$N_x$	12,290	3072	1536	1282
$N_r$	192	176	176	192

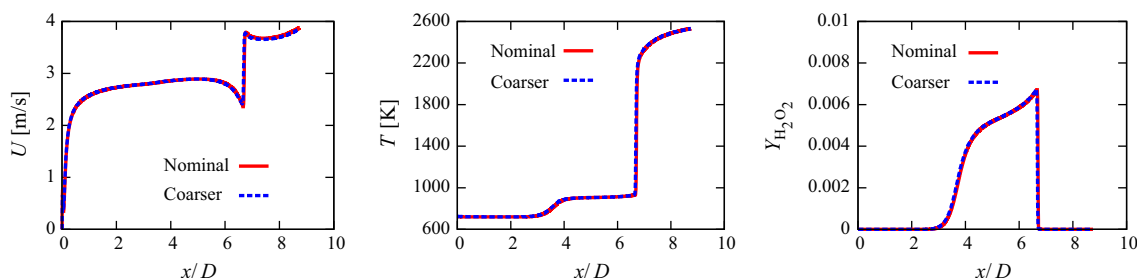


**Fig. 1.** Velocity, temperature, and  $\text{H}_2\text{O}_2$  profiles along  $Z_{st}$  on the nominal and two times coarser (in each direction) meshes for an air temperature of 800 K.

A grid convergence study was performed for the air temperature 800 K case, for it has the most complex structure, which is discussed in the following sections. As shown in Fig. 1, grid convergence was achieved for velocity, temperature, and species profiles. Grid convergence was also verified for the air temperature 1100 K case, which shows similar results and is therefore not shown here.

### 3. Thermal and chemical structure

To visualize the flame structures, the heat release rate profiles for the four cases (700, 800, 900, and 1100 K) are shown in Fig. 2. Qualitatively, the most upstream point on the largest heat release contour (the leading point), colored<sup>1</sup> by red, will be referred to as the stabilization point.

At 700 K, a tribrachial thermal structure is observed, and the stabilization point is located around  $Z = 0.15$ , which is richer than the triple point, where the three branches intersect. Moreover, compared to the classical triple flame structure, the middle heat release rate branch, corresponding to the nonpremixed flame, is significantly weaker than the other two branches.

At 800 K, the stabilization point is not located on the tribrachial structure any more. Instead, it is located near  $Z = 0.23$  and connects two trailing heat release branches, where a tribrachial flame structure is attached to the leaner branch (LB) of the bibrachial reacting front. A schematic of the structure is shown in Fig. 3.

As the air boundary temperature increases to 900 K, the stabilization point shifts back to  $Z = 0.14$ . Moreover, a long trailing branch at richer mixture fraction is attached to the main tribrachial structure, resulting in a tetrabrachial structure. Compared with the structure shown in the 800 K case, the main tribrachial structure stabilizes further upstream, for it depends less on the radical accumulation ahead of the flame. Therefore, it catches up with the reacting front at richer mixture fraction, and they merge into the apparent tetrabrachial structure.

A further increase in the boundary temperature results in a structure that is very similar to the classical triple flame, except for the fact that there is also heat release ahead of the stabilization point at  $Z = 0.13$ . Some of the multibrachial structures were also observed by Krisman et al. [18], using different definitions for branches, and it was concluded that the autoignition chemistry could affect the flame structure and the stabilization mechanism.

To first qualitatively demonstrate the chemical structure of the flame, selected species profiles were examined, shown in Figs. 4–7. The methoxymethylperoxy radical ( $\text{CH}_3\text{OCH}_2\text{O}_2$ ) and hydroxyl radical (OH) were chosen as indicators of low and high temperature chemistry, respectively. The hydroperoxyl radical ( $\text{HO}_2$ ) and hydrogen peroxide ( $\text{H}_2\text{O}_2$ ) were chosen, for they form in the preheat

zone of a flame or before autoignition but quickly vanish in the post flame zone or after ignition [32].

For all four cases, similar profiles can be seen for some species. First, low temperature chemistry, indicated by the  $\text{CH}_3\text{OCH}_2\text{O}_2$  radical, is found to be important at richer mixture fractions, where the temperature is also lower. Second, the OH radical peaks at and downstream of the maximum heat release locations and correlates well with the tribrachial structure shown in the heat release rate profiles, indicating the presence of high temperature chemistry. Third, the  $\text{HO}_2$  mass fraction peaks in a thin region. Compared with the heat release rate contours, this thin region outlines the flame front and the reactive mixture at the rich mixture fractions and indicates the importance of the exothermic three-body recombination reaction  $\text{H} + \text{O}_2 + \text{M} \rightleftharpoons \text{HO}_2 + \text{M}$ .

However, there are also differences in the chemical structure among the different cases. For example, for the 800 and 900 K cases, another OH local maxima, which is two orders of magnitude smaller than the peak value on the tribrachial structure, appears at richer mixture fractions, immediately downstream of where the  $\text{CH}_3\text{OCH}_2\text{O}_2$  radical and  $\text{H}_2\text{O}_2$  disappear, indicating autoignition. Moreover, more pronounced differences between the three lower boundary temperature cases and the 1100 K case are shown in the  $\text{H}_2\text{O}_2$  profiles: for the lower boundary temperature cases,  $\text{H}_2\text{O}_2$  accumulates along the mixture fraction iso-contours until it decomposes in the flame region, while, for the 1100 K case, the  $\text{H}_2\text{O}_2$  accumulation is an order of magnitude lower, due to the reduced residence time from the nozzle exit to the flame base.

### 4. Computational diagnostics and analysis

The above heat release rate and species profiles demonstrate the thermal and chemical structure of the reacting fronts at different boundary temperatures. However, more detailed computational diagnostics and analysis are needed to further demonstrate the controlling chemistry and the stabilization mechanism.

#### 4.1. Chemical explosive mode analysis

In addition to the analysis based on selected species profiles, Chemical Explosive Mode Analysis (CEMA) [33,34] was conducted to identify the controlling chemistry in these complex reacting flows. Briefly, the eigenvalues of the Jacobian matrix of the chemical source term based on the local species concentrations and temperature are evaluated and determined as the chemical modes. The largest real part of all eigenvalues, which is defined as the chemical explosive mode, describes the rate of system runaway. The normalized contribution of each reaction to the chemical explosive mode is quantified with a participation index [34].

In the present study, the dominant reactions at representative locations, such as those upstream and near the flame base, are identified, based on the explosive mode and participation index.

<sup>1</sup> For interpretation of color in Fig. 2, the reader is referred to the web version of this article.

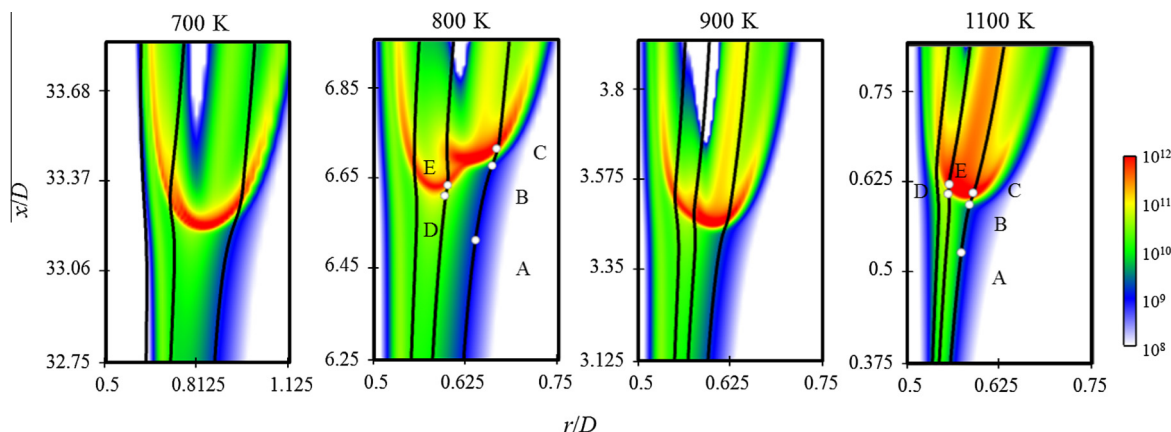


Fig. 2. Heat release rate [ $\text{J}/\text{m}^3 \text{ s}$ ] profiles. The iso-contours of  $Z_{st}$ ,  $Z = 0.2$ , and  $Z = 0.3$  are outlined from right to left in solid lines, respectively. The CEMA sampling points at 800 and 1100 K are indicated along the iso-contours.

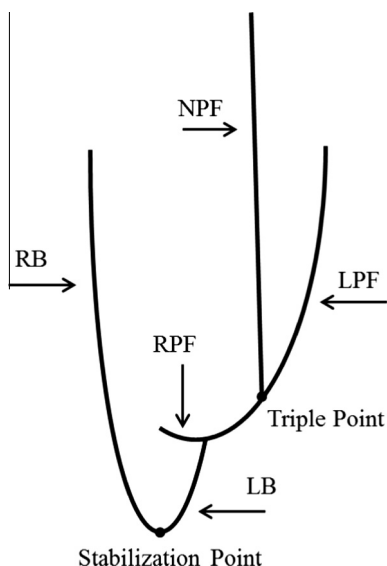


Fig. 3. A schematic of the thermal structure of the 800 K case. LPF, RPF, and NPF denotes the lean premixed, rich premixed, and nonpremixed flame branches on the tribrachial structure, respectively. LB and RB denotes the leaner and richer branches of the reacting front, respectively.

For each case, the local species concentrations and temperature were sampled along the  $Z_{st}$ ,  $Z = 0.2$ , and  $Z = 0.3$  iso-contours, as indicated in Fig. 2, and processed by CEMA to demonstrate the evolution of the dominant reactions.

The results are summarized in Fig. 8, where three representative locations along the  $Z_{st}$  iso-contour approaching the flame front and two locations ahead of and at the reaction front at  $Z = 0.2$  were sampled. For the three lower coflow temperature cases, similar chemical patterns were found. Upstream of the flame front, the chemical explosive mode is positive, indicating that the mixtures have the potential to explode; downstream of the flame front, the chemical explosive mode becomes negative, meaning that the mixtures are composed of burned products. Following the  $Z_{st}$  iso-contour, the hydrogen peroxide chain branching reaction ( $\text{H}_2\text{O}_2 + \text{M} \rightleftharpoons \text{OH} + \text{OH} + \text{M}$ ) is the reaction that has the largest contribution to the explosive mode, showing the dominant role of autoignition chain branching [35]. The characteristic DME low temperature chemistry is also important upstream of the flame, where methoxymethylperoxy radical formation ( $\text{CH}_3\text{OCH}_2 + \text{O}_2 \rightleftharpoons \text{CH}_3\text{OCH}_2\text{O}_2$ ) and isomerization ( $\text{CH}_3\text{OCH}_2\text{O}_2 \rightleftharpoons \text{CH}_2\text{OCH}_2\text{O}_2\text{H}$ ) promote the explosion, while the  $\beta$ -scission reaction ( $\text{CH}_2\text{OCH}_2\text{O}_2\text{H} \rightleftharpoons \text{OH} + \text{CH}_2\text{O} + \text{CH}_2\text{O}$ ) retards the explosion. Approaching the flame front, the H radical recombination reaction ( $\text{H} + \text{O}_2 + \text{M} \rightleftharpoons \text{HO}_2 + \text{M}$ ) becomes important for the 700–900 K cases, due to the fact that the H radicals generated at the reaction zone diffuse upstream and undergo three-body recombination reactions under the high pressure, low temperature condition. Further downstream where the heat release rate peaks, the hydrogen branching reaction ( $\text{H} + \text{O}_2 \rightleftharpoons \text{O} + \text{OH}$ ) becomes the most important chain branching reaction as it is activated at high temperatures [35].

CEMA conducted along the  $Z = 0.2$  iso-contour, which crosses the rich heat release front in the 800 and 900 K cases, shows

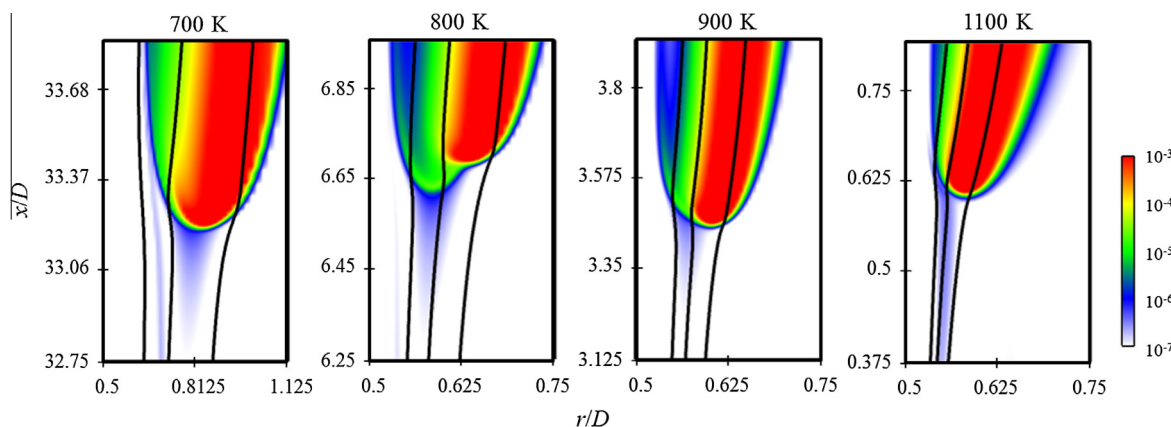


Fig. 4. Hydroxyl (OH) radical mass fraction profiles. The mixture fraction iso-contours are the same as in Fig. 2.

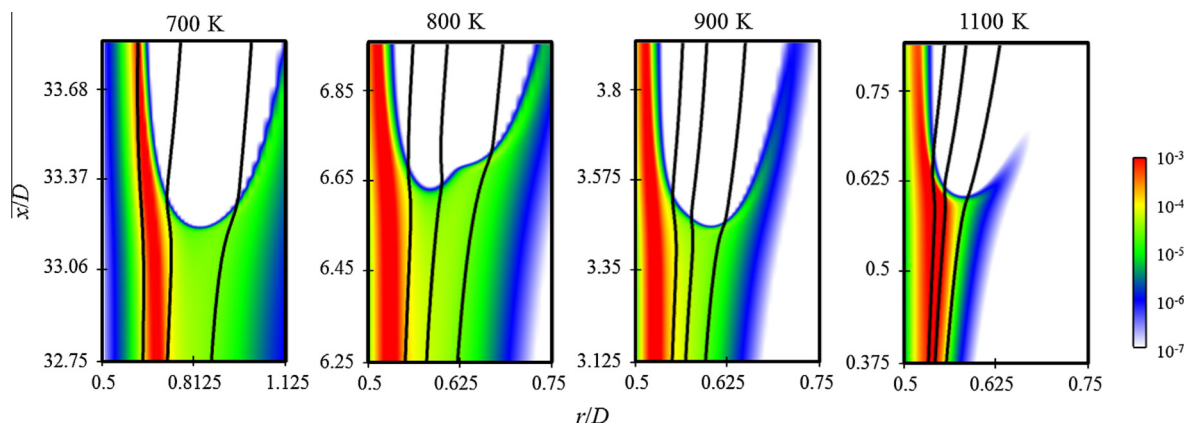


Fig. 5. Methoxymethylperoxy ( $\text{CH}_3\text{OCH}_2\text{O}_2$ ) radical mass fraction profiles. The mixture fraction iso-contours are the same as in Fig. 2.

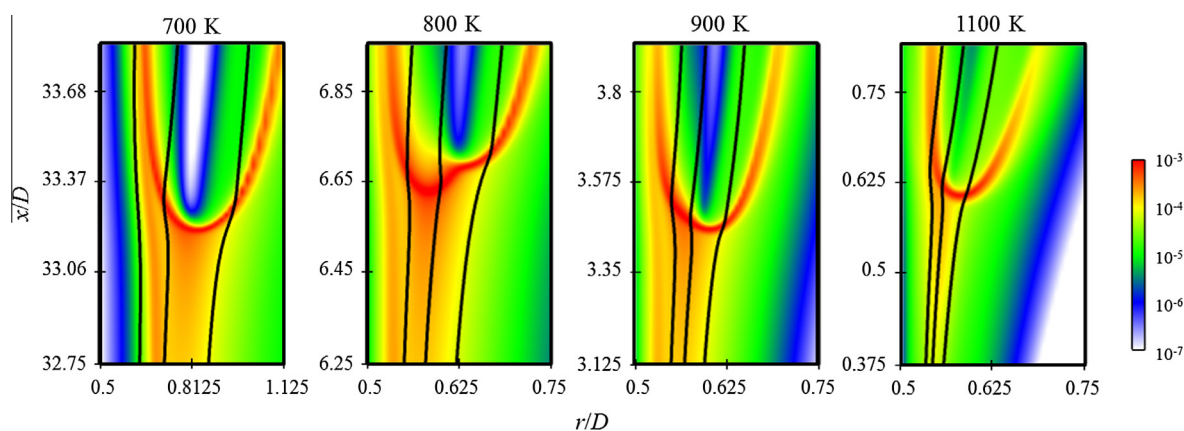


Fig. 6. Hydroperoxyl ( $\text{HO}_2$ ) radical mass fraction profiles. The mixture fraction iso-contours are the same as in Fig. 2.

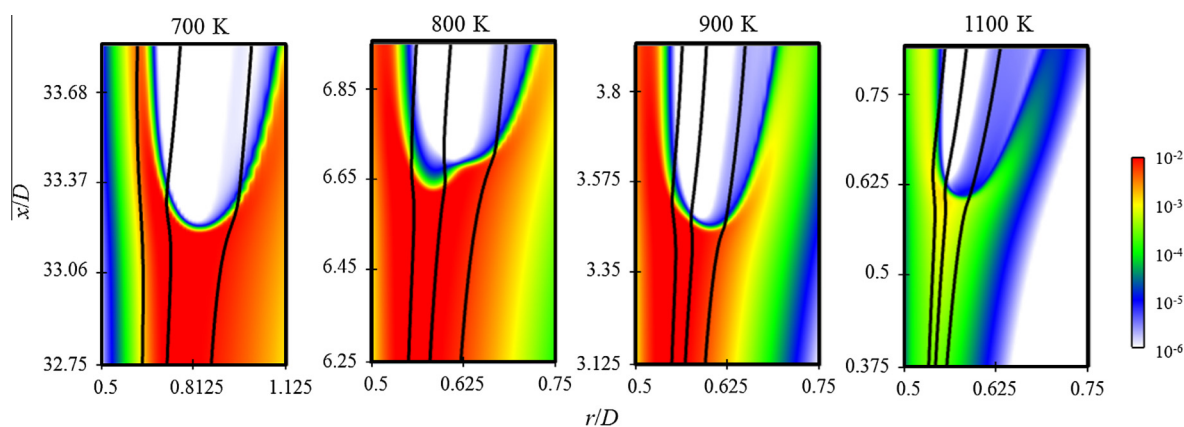


Fig. 7. Hydrogen peroxide ( $\text{H}_2\text{O}_2$ ) mass fraction profiles. The mixture fraction iso-contours are the same as in Fig. 2.

different chemical mode evolution. The  $\text{H}_2\text{O}_2$  chain branching reaction is always the dominant reaction that promotes the explosive mode, while the H radical recombination reaction and the H branching reaction are less important ahead of the rich heat release front and at the front.

On the contrary, although low temperature chemistry is still important for the 1100 K case upstream of the reaction zone and the hydrogen chain branching reaction promotes explosion in the reaction zone, the hydrogen peroxide chain branching reaction is not very important for all the sampled locations. Since the hydrogen peroxide reaction is the crucial chain branching reaction for

the autoignition process, it is concluded that the 1100 K case is less affected by autoignition chemistry than the lower boundary temperature cases.

#### 4.2. Lagrangian flamelet analysis

The above species profile analysis and CEMA results have demonstrated that autoignition chemistry is crucial to the complex flame structure in the 700–900 K cases. However, the role that autoignition plays in the stabilization still needs further investigation. To elucidate the role of autoignition for the current flow

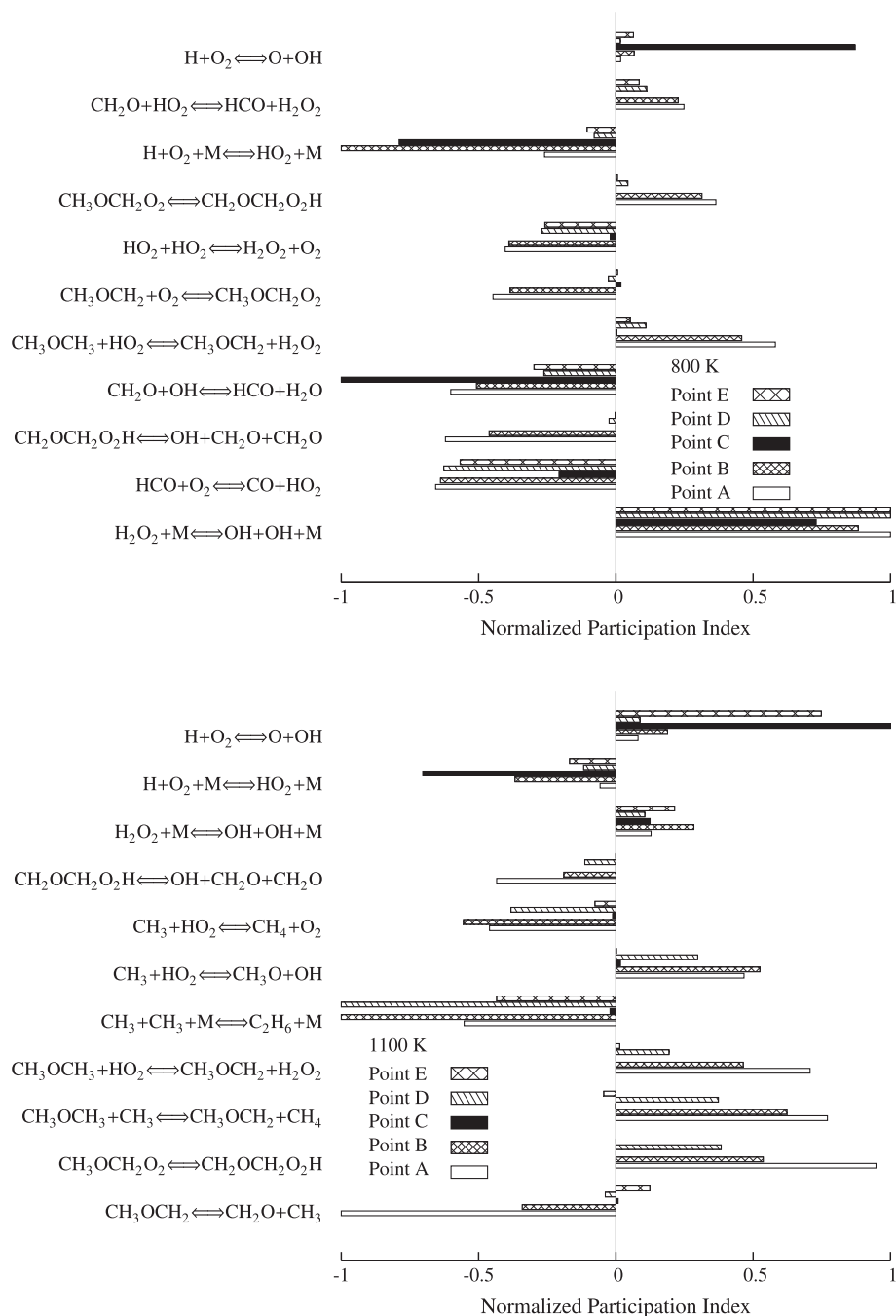


Fig. 8. Normalized participation index at 800 K and 1100 K. Sampled locations are indicated in Fig. 2.

configuration, a direct comparison with the homogeneous counterpart for a Lagrangian flow particle is insufficient, for no transport process is considered in homogeneous autoignition. In the current two-dimensional configuration, however, transport processes are present in two directions: parallel and normal to the mixture fraction gradient. These transport processes might be important: first, the temperature and species stratification parallel to the mixture fraction gradient can significantly modify the ignition characteristics, especially for fuels with NTC chemistry [15,17]. Second, flame propagation normal to the mixture fraction gradient can also influence the autoignition front through thermal and radical back diffusion.

To demonstrate the dominant transport direction as well as the stabilization mechanism in the current work, one-dimensional

unsteady flamelet analysis was conducted to account for unsteadiness (convection), chemical reactions, and diffusion parallel to the mixture fraction gradient, while neglecting the transport process in the normal direction. As a consequence, the unsteady flamelet is able to capture inhomogeneous autoignition, with diffusion allowed only in one direction. Following the mixture fraction iso-contour, the spatial information from the two-dimensional computation could be interpreted as the time history of the corresponding mixture in the Lagrangian frame. If the one-dimensional unsteady flamelet predicts this time history, only the transport processes parallel to the mixture fraction gradient are important, and, therefore, the thermal structure is stabilized by inhomogeneous autoignition. Conversely, if the unsteady flamelet solutions do not agree with the two-dimensional computations, the

transport processes along the mixture fraction iso-contour are not negligible compared to the gradient direction. Therefore, premixed flame propagation is the dominant stabilization mechanism, or, at least, stabilization is strongly affected by flame back diffusion.

In the present work, the unsteady flamelet model developed by Pitsch et al. [36], referred to as Lagrangian Flamelet Analysis (LFA), was adopted. Due to the mixing processes, the scalar dissipation rate  $\chi$ , which can influence the flamelet solution significantly, decreases in the streamwise direction. Therefore, this dissipation rate variation must be considered when computing a flamelet as it evolves downstream.

In the present study, the unsteady flamelet was computed with FlameMaster [37], and the dissipation rate was specified as a function of the flamelet time. The flamelet time was computed from the two-dimensional computational results, along the stoichiometric mixture fraction  $Z_{st}$  iso-contour:

$$t = \int_0^x \frac{1}{(u + u_z)(x')|Z = Z_{st}} dx'. \quad (1)$$

This formulation is otherwise the same as that of Pitsch et al. [36], except that, in addition to the axial component of fluid convection velocity  $u$ , the axial component of the mixture fraction iso-contour propagation speed relative to the fluid convection  $u_z$  is also taken into account. The expression for the constant property scalar iso-surface velocity relative to the local fluid motion was derived by Pope [38], and the current work adopts the formulation derived by Lignell et al. [39] for variable properties:

$$\mathbf{u}_z = -\frac{\nabla \cdot (\rho D_z \nabla Z)}{\rho |\nabla Z|} \mathbf{n}, \quad (2)$$

where  $D_z$  is the mixture fraction diffusivity, which is defined in Section 2, and  $\rho$  the density. The normal vector  $\mathbf{n}$ , defined as

$$\mathbf{n} = \frac{\nabla Z}{|\nabla Z|}, \quad (3)$$

indicates the direction of this diffusion induced relative velocity. The dissipation rate along the  $Z_{st} = 0.1005$  iso-contour obtained from the two-dimensional computation was then correlated with this flamelet time and provided as the input for the LFA calculation. The dissipation rates at other mixture fractions were computed assuming the following form [40]:

$$\chi(Z) = \chi(Z_{st}) \frac{\exp(-2[\operatorname{erfc}^{-1}(2Z)]^2)}{\exp(-2[\operatorname{erfc}^{-1}(2Z_{st})]^2)} = \chi(Z_{st})f(Z; Z_{st}). \quad (4)$$

To validate this formulation in the current configuration, the dissipation rates along different mixture fraction iso-contours were sampled from the two-dimensional computations, normalized using Eq. (4), and compared with the sampling along the  $Z_{st}$  iso-contour. As shown in Fig. 9, the normalized dissipation rates at different mixture fractions all collapse to the value at  $Z_{st}$ . Therefore, only the dissipation rate samplings along the  $Z_{st}$  iso-contour were needed to perform the unsteady flamelet calculation.

To account for the differential diffusion, species Lewis numbers for LFA were specified the same as in the two-dimensional computations. The governing equations for species and temperature follow Eqs. (24) and (25) in Pitsch and Peters [19].

In the current work, the time history of the dissipation rate  $\chi_{st}$  was specified in LFA according to the two-dimensional computation. To avoid the ill-defined Lagrangian time in the recirculation zone, time zero was defined at a downstream location ten times the thickness of the wall. Accordingly, the species and temperature profiles along the radial cut at this location were specified as the initial conditions for the flamelet. Based on these initial conditions and  $\chi_{st}$  time history profiles, the unsteady flamelets were

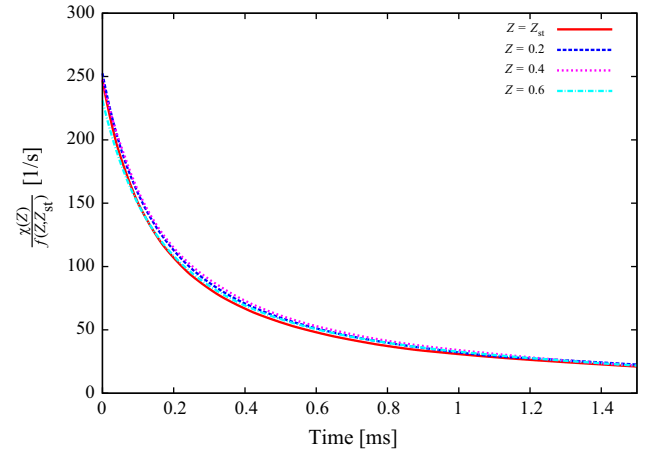


Fig. 9.  $\frac{\chi(Z)}{f(Z; Z_{st})}$ , using Eq. (4), from the two-dimensional calculations at 800 K.

calculated and compared with the two-dimensional computational results for  $Z_{st}$ ,  $Z = 0.2$ , and  $Z = 0.3$ .

As shown in Fig. 10, two ignition stages can be seen at  $Z_{st}$  and  $Z = 0.2$  for the 700 K case, while at  $Z = 0.3$  only one ignition dominated by low temperature chemistry is observed, due to the reduced initial temperature. At all three mixture fractions examined, the flamelets agree with the two-dimensional computations very well. For the 800 K case, both the flamelet and two-dimensional computation experience almost identical time histories, where two-stage ignition occurs at all three mixture fractions. As the initial temperature further increases, corresponding to the increase in the boundary temperatures in the CFD computation, the two-stage ignition phenomenon is less pronounced. However, the 900 K case still shows good agreement between the flamelet profile with the time history of the two-dimensional computation at  $Z = 0.2$  and  $0.3$ , while LFA slightly lags behind the CFD computation at  $Z_{st}$ , similar to the 800 K case.

On the contrary, for the 1100 K case, the ignition delay time computed with the one-dimensional flamelet assumption is significantly longer than the two-dimensional counterpart, indicating that transport processes along the mixture fraction iso-contours must be important and that autoignition is less important to the stabilization mechanism.

## 5. Stabilization mechanism

With the above analysis based on species profiles, Chemical Explosive Mode Analysis, and Lagrangian Flamelet Analysis, the transition of the stabilization mechanism and the coupling between autoignition chemistry and flame propagation can be clearly identified. In the current study, two fundamental stabilization mechanisms are relevant: the *kinetic* stabilization mechanism, due to the balance between the autoignition delay time and flow residence time, and the *kinematic* stabilization mechanism, due to the balance between the local premixed flame propagation velocity and the local flow velocity.

In this stratified composition and temperature field, autoignition and flame propagation are coupled through thermal and radical interactions, for the accumulation of the upstream radicals and heat release from autoignition accelerate the flame propagation velocity. The flame also transfers heat and radicals through back diffusion processes to the upstream, which could also facilitate autoignition.

In the current study, the stabilization mechanism was determined by comparing the two-dimensional computations with the one-dimensional inhomogeneous autoignition predicted by LFA.

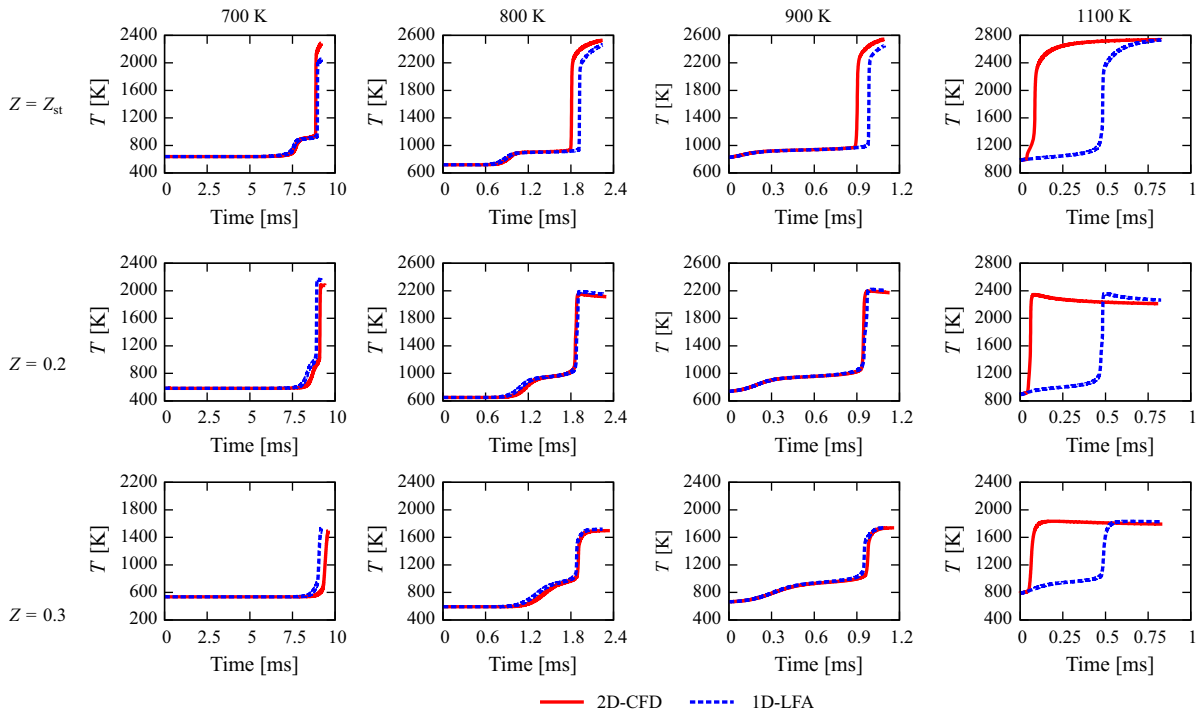


Fig. 10. Comparison between 2D-CFD and 1D-LFA results.

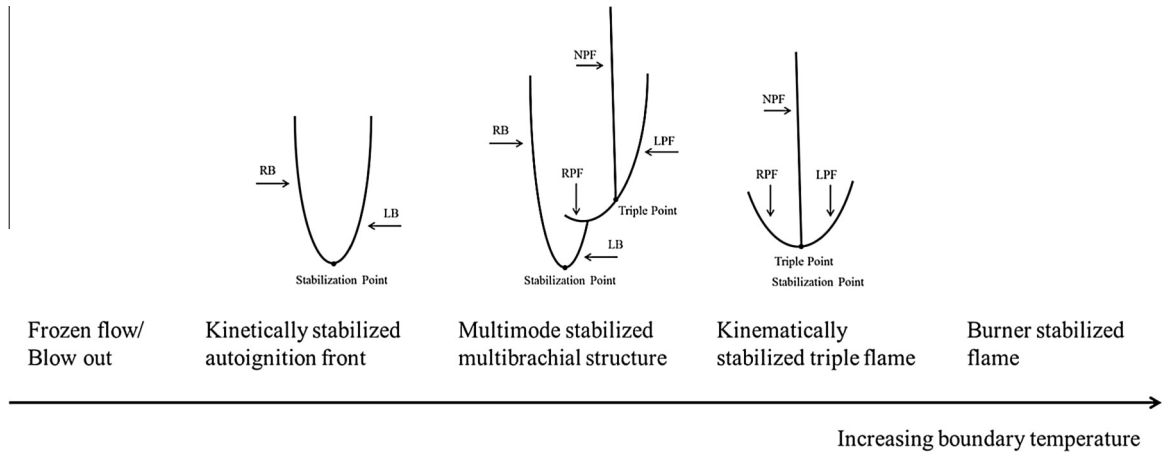


Fig. 11. Extended regimes of the stabilization mechanism as the coflow boundary temperature increases.

When these two time history profiles agree well, the case is characterized as *kinetically* stabilized. Specifically, at 700 K, the one-dimensional LFA agrees very well with the two-dimensional computation at all of the mixture fractions examined. Therefore, the 700 K case is characterized as *kinetically* stabilized. As the boundary temperature increases, the influences from premixed flame propagation become important, as predictions by LFA lag behind the CFD results for some mixture fractions. At 800 K, an autoignition front stabilizes the multibrachial structure at rich mixture fractions, due to the shorter ignition delay time resulting from the NTC chemistry, and a modified triple flame structure stabilizes slightly downstream of this front at leaner mixture fractions, as shown in Fig. 2. Further increasing the boundary temperature results in higher flame propagation velocities. Therefore, the flame front at leaner mixture fraction depends less on radical accumulation ahead of the flame and propagates

upstream, and the stabilization is influenced by both inhomogeneous autoignition and premixed flame propagation. The transition to a *kinematically* stabilized flame structure is achieved for the 1100 K case, where the local flame propagation velocity balances the incoming flow velocity. Therefore, the flame structure stabilizes close to the nozzle exit and depends least on radical accumulation from upstream. Consequently, the one-dimensional LFA predictions depart from the two-dimensional computation significantly.

Based on the understanding obtained from the current study, further extension of the stabilization regime can be made, as shown in Fig. 11. For fixed inlet flow velocity, when the boundary temperature is sufficiently low, the mixture cannot be autoignited, and it is essentially a frozen flow. Even when an external ignition source is applied, the flame cannot keep up with the excessive high flow velocity, such that the flame blows out. When the boundary

temperature is high enough to activate autoignition, it occurs far downstream, but the flame propagation velocity still cannot keep up with the flow velocity. As a consequence, a pure *kinetically* stabilized autoignition front can be achieved, which is similar to the 700 K case. Conversely, when the boundary temperature is sufficiently high, the flame stabilizes close to the inlet, where the upstream can be treated as frozen, due to reduced residence time, which is similar to the 1100 K case. Therefore, a *kinematically* stabilized classical triple flame structure is achieved. Further increase in the boundary temperature results in an attached flame with the increased flame speed. Although not included in the current paper, an attached flame was computed at 1500 K. In between the *kinetically* and *kinematically* stabilized regimes, there is a transitional regime governed by both mechanisms, which corresponds to the 800 and 900 K cases. Due to the NTC behavior of the autoignition chemistry, the stabilization point, in terms of mixture fraction space, varies, and the complex multibrachial flame structure appears.

## 6. Conclusions

In the present study, two-dimensional nonpremixed DME flames in heated air coflows were computed. The computations were conducted at 30 atmospheres to observe the influence of NTC chemistry on the stabilization mechanism. A uniform and fixed inlet boundary velocity was specified, and four coflow temperature (700, 800, 900, and 1100 K) cases were studied.

The heat release rate profile and characteristic species profiles for low and high temperature chemistry, autoignition, and premixed flame propagation were examined. Further investigation based on Chemical Explosive Mode Analysis and Lagrangian Flamelet Analysis enabled the determination of the evolution of the controlling chemical pathways and the stabilization mechanism.

The 700 K case was characterized as *kinetically* stabilized, for, neglecting the diffusion processes along mixture fraction iso-contours, the one-dimensional LFA agrees with the two-dimensional CFD responses. As the boundary temperature increases, the leading point of the heat release profile shifts to richer mixture fractions and then shifts back due to the NTC effect on the autoignition process and the coupling between autoignition and premixed flame propagation chemistry. Stabilization is also affected by both inhomogeneous autoignition and premixed flame propagation, as in the 800 and 900 K cases. The 1100 K case was characterized as *kinematically* stabilized, for it exhibits the classical triple flame structure, with stabilization achieved due to the balance between the premixed flame propagation velocity and the local incoming flow velocity.

Based on the present study, the following extended stabilization regimes are identified. For sufficiently high inlet velocity, as the boundary temperature increases from the cold case, the flow is chemically frozen, and the mixture is nonautoignitive; even the flame generated by an external ignition source will blow out. When the mixture can be autoignited, the *kinetically* stabilized autoignition front gradually transits to a *kinematically* stabilized classical triple flame, where the premixed flame front propagation velocity balances the local incoming flow velocity. The triple flame will eventually become attached when the boundary temperature is sufficiently high, and the flame speed is sufficiently fast.

Further study on the effects of fuel dilution and inlet velocity on the lift-off height, stabilized flame structure, and stabilization mechanism, is suggested. For example, the boundary velocity can be varied to change the flow residence time, and dilution can be

added to the fuel stream to change the chemical time scale. Moreover, if autoignition is the dominant stabilization mechanism and the scalar dissipation rate sufficiently low, the nonmonotonic lifted height variation can be observed as the boundary temperature changes, which is plausible based on homogeneous autoignition and nonpremixed counterflow observations [17]. Finally, high pressure experiments are needed to provide potential experimental substantiation of these predicted multibrachial structures.

## Acknowledgments

This research was supported in part by the Air Force Office of Scientific Research (AFOSR) under the technical management of Dr. Mitat Birkan.

## Appendix A. Supplementary material

Supplementary data associated with this article can be found, in the online version, at <http://dx.doi.org/10.1016/j.combustflame.2015.06.007>.

## References

- [1] J. Buckmaster, *Prog. Energy Combust. Sci.* 28 (2002) 435–475.
- [2] S.H. Chung, *Proc. Combust. Inst.* 31 (2007) 877–892.
- [3] J.W. Dold, *Combust. Flame* 76 (1989) 71–88.
- [4] L.J. Hartley, J.W. Dold, *Combust. Sci. Technol.* 80 (1991) 23–46.
- [5] S. Ghosal, L. Vervisch, *J. Fluid Mech.* 415 (2000) 227–260.
- [6] M.K. Kim, S.H. Won, S.H. Chung, *Proc. Combust. Inst.* 31 (2007) 901–908.
- [7] G.R. Ruetsch, L. Vervisch, A. Liñán, *Phys. Fluids* 7 (1995) 1447.
- [8] B.J. Lee, S.H. Chung, *Combust. Flame* 109 (1997) 163–172.
- [9] T. Plessing, P. Terhoeven, N. Peters, M.S. Mansour, *Combust. Flame* 115 (1998) 335–353.
- [10] P.N. Ki-oni, K.N.C. Bray, D.A. Greenhalgh, B. Rogg, *Combust. Flame* 116 (1999) 192–206.
- [11] B.C. Choi, K.N. Kim, S.H. Chung, *Combust. Flame* 156 (2009) 396–404.
- [12] B.C. Choi, S.H. Chung, *Combust. Flame* 157 (2010) 2348–2356.
- [13] B.C. Choi, S.H. Chung, *Combust. Flame* 159 (2012) 1481–1488.
- [14] J. Zádor, C.A. Taatjes, R.X. Fernandes, *Prog. Energy Combust. Sci.* 37 (2011) 371–421.
- [15] C.K. Law, P. Zhao, *Combust. Flame* 159 (2012) 1044–1054.
- [16] P. Zhao, C.K. Law, *Combust. Flame* 160 (2013) 2352–2358.
- [17] S. Deng, P. Zhao, D. Zhu, C.K. Law, *Combust. Flame* 161 (2014) 1993–1997.
- [18] A. Krisman, E.R. Hawkes, M. Talei, A. Bhagatwala, J.H. Chen, *Proc. Combust. Inst.* 35 (2015) 999–1006.
- [19] H. Pitsch, N. Peters, *Combust. Flame* 114 (1998) 26–40.
- [20] H.J. Curran, W.J. Pitz, C.K. Westbrook, P. Dagaut, J.-C. Boettner, M. Cathonnet, *Int. J. Chem. Kinet.* 30 (1998) 229–241.
- [21] S.L. Fischer, F.L. Dryer, H.J. Curran, *Int. J. Chem. Kinet.* 32 (2000) 713–740.
- [22] H.J. Curran, S.L. Fischer, F.L. Dryer, *Int. J. Chem. Kinet.* 32 (2000) 741–759.
- [23] Z. Zhao, M. Chaos, A. Kazakov, F.L. Dryer, *Int. J. Chem. Kinet.* 40 (2008) 1–18.
- [24] E.W. Kaiser, T.J. Wallington, M.D. Hurley, J. Platz, H.J. Curran, W.J. Pitz, C.K. Westbrook, T.J. Wallington, *J. Phys. Chem. A* 104 (2000) 8194–8206.
- [25] X.L. Zheng, T.F. Lu, C.K. Law, C.K. Westbrook, H.J. Curran, T. Berces, F.L. Dryer, *Proc. Combust. Inst.* 30 (2005) 1101–1109.
- [26] X. Qin, Y. Ju, *Proc. Combust. Inst.* 30 (2005) 233–240.
- [27] A. Bhagatwala, Z. Luo, H. Shen, J.A. Sutton, T. Lu, J.H. Chen, *Proc. Combust. Inst.* 35 (2015) 1157–1166.
- [28] O. Desjardins, G. Blanquart, G. Balarac, H. Pitsch, *J. Comput. Phys.* 227 (2008) 7125–7159.
- [29] X. Liu, S. Osher, T. Chan, *J. Comput. Phys.* 115 (1994) 200–212.
- [30] C.D. Pierce, P. Moin, *Progress-Variable Approach for Large-Eddy Simulation of Turbulent Combustion*, Ph.D. Thesis, Stanford University, 2001.
- [31] S.D. Cohen, A.C. Hindmarsh, P.F. Dubois, *Comput. Phys.* 10 (1996) 138.
- [32] C.S. Yoo, R. Sankaran, J.H. Chen, *J. Fluid Mech.* 640 (2009) 453–481.
- [33] T.F. Lu, C.S. Yoo, J.H. Chen, C.K. Law, *J. Fluid Mech.* 652 (2010) 45–64.
- [34] R. Shan, C.S. Yoo, J.H. Chen, T. Lu, *Combust. Flame* 159 (2012) 3119–3127.
- [35] C.K. Westbrook, *Proc. Combust. Inst.* 28 (2000) 1563–1577.
- [36] H. Pitsch, M. Chen, N. Peters, *Proc. Combust. Inst.* 27 (1998) 1057–1064.
- [37] H. Pitsch, *FlameMaster*, A C++ Computer Program for OD Combustion and 1D Laminar Flame Calculations.
- [38] S.B. Pope, *Int. J. Eng. Sci.* 26 (1988) 445–469.
- [39] D.O. Lignell, J.H. Chen, P.J. Smith, T. Lu, C.K. Law, *Combust. Flame* 151 (2007) 2–28.
- [40] N. Peters, *Turbulent Combustion*, Cambridge University Press, 2000.



# Stabilization of laminar nonpremixed DME/air coflow flames at elevated temperatures and pressures



Sili Deng, Peng Zhao, Michael E. Mueller\*, Chung K. Law

Department of Mechanical and Aerospace Engineering, Princeton University, Princeton, NJ 08544, USA

## ARTICLE INFO

### Article history:

Received 17 June 2015

Revised 25 August 2015

Accepted 26 August 2015

Available online 29 September 2015

### Keywords:

Stabilization

Nonpremixed coflow flame

Autoignition

Negative temperature coefficient (NTC)

Dimethyl ether (DME)

## ABSTRACT

The structure and stabilization mechanism of laminar nonpremixed autoignitive DME/air coflow flames was investigated at elevated temperatures and pressures. Computations with detailed chemistry were performed for DME and heated coflow air at 30 atm with uniform inlet velocities (2.4, 3.2, and 8.0 m/s) imposed for both streams. The heat release rate profiles are first examined for each case to demonstrate a multibrachial thermal structure. Species concentrations and temperature were sampled along mixture fraction iso-contours, and Chemical Explosive Mode Analysis (CEMA) was performed to identify the controlling chemistry at representative points. One-dimensional Lagrangian Flamelet Analysis (LFA) was also performed and compared with the two-dimensional computations to elucidate the relative importance of diffusion processes parallel and normal to the mixture fraction gradient. Various coflow temperatures with different inlet velocities are examined to elucidate their influences on the multibrachial structure as well as the stabilization mechanism. NTC (negative temperature coefficient)-affected inhomogeneous autoignition and the coupled effects with premixed flame propagation on stabilization are further studied. It is found that, at high coflow boundary temperatures or low inlet velocities, the classical tribrachial flame structure is achieved, and autoignition contributes less to the stabilization due to reduced heat and radical accumulation. The kinematic balance between the local flow speed and flame propagation speed is the dominant stabilization mechanism. On the contrary, kinetic stabilization is achieved at lower coflow temperatures or higher inlet velocities as autoignition becomes dominant. Due to the transition of the dominant chemical pathways during autoignition, the kinetically stabilized structure is usually multibrachial. The transition of different stabilization mechanisms can be made by changing either the boundary velocity or temperature of the coflow. Based on these results and previous work (Deng et al., 2015) [12], a regime diagram is constructed that identifies the possible stabilization regimes: blow out, kinetically stabilized, autoignition-propagation-coupled stabilized, kinematically stabilized, and burner stabilized.

© 2015 The Combustion Institute. Published by Elsevier Inc. All rights reserved.

## 1. Introduction

Two-dimensional tribrachial structures (also known as triple flames) [1] are observed in nonpremixed laminar lifted flames at nonautoignitive conditions. The dynamic balance between the local flame propagation speed and the incoming flow speed at the triple point is generally considered as the stabilization mechanism [2]. However, practical engines operate at elevated pressures and temperatures. As a consequence, the propensity for autoignition is significantly enhanced, and, therefore, the thermal and chemical structure of the tribrachial flame, as well as the stabilization mechanism, could be affected by the autoignition process. For example, experimentally, Chung and co-workers have investigated autoignited

lifted propane/nitrogen [3], methane/hydrogen [4], and other neat  $C_1$ – $C_4$  hydrocarbon flames [5], and compared their lift-off heights with homogeneous autoignition delay time. Furthermore, the autoignition process of most large hydrocarbons under practical engine conditions could possibly lie in the negative temperature coefficient (NTC) regime, in which the overall ignition delay time increases as the initial temperature increases. The NTC phenomenon is relevant to engine knock [6] and has been extensively studied in homogeneous systems [7]. As Law and co-workers [8–10] recently demonstrated, ignition characteristics in a nonpremixed system can also be affected by NTC chemistry, especially at elevated pressures and/or extended residence times. These computational and experimental studies were conducted in the nonpremixed counterflow system where the residence time is well characterized. When the flow residence time and NTC chemistry timescales are comparable, the two processes are strongly coupled, resulting in modified system response, such as autoignition behavior.

\* Corresponding author.

E-mail addresses: [silideng@princeton.edu](mailto:silideng@princeton.edu), [silideng@gmail.com](mailto:silideng@gmail.com) (S. Deng), [muellerm@princeton.edu](mailto:muellerm@princeton.edu) (M.E. Mueller).

To investigate autoignition with NTC chemistry effects in non-premixed lifted flame stabilization, Krisman et al. [11] recently conducted a numerical study of dimethyl ether (DME)/air nonpremixed flames at 40 atmospheres and elevated air coflow temperatures (700–1500 K) and observed multibrachial thermal structures. The autoignition response in the two-dimensional computation was compared with that of homogeneous autoignition under the same initial conditions. A transport budget analysis of methoxymethylperoxy ( $\text{CH}_3\text{OCH}_2\text{O}_2$ ) and hydroxyl (OH) radicals, which represent the low and high temperature chemistry, respectively, was performed to differentiate deflagration from autoignition. The stabilization points of the multibrachial structure was determined with  $\text{CH}_3\text{OCH}_2\text{O}_2$  and OH radical mass fractions for low and high temperature autoignition chemistry, respectively, and varied as boundary temperature and velocity changed.

More recently, to further elucidate the chemical structure of the multibrachial structure and the roles of autoignition and flame chemistry in the stabilization mechanism, the authors [12] performed a numerical study of nonpremixed DME/air coflow flames. Chemical Explosive Mode Analysis (CEMA) was adopted to identify locally dominant reactions, and Lagrangian Flamelet Analysis (LFA) was adopted to identify the dominant combustion mode. The comparison with the two-dimensional computation was able to quantify the relative importance of transport processes parallel and normal to the mixture fraction gradient and elucidate the dominant stabilization mechanism. For increasing coflow boundary temperature at constant inlet velocities, the stabilization mechanism transitioned from kinetic to kinematic stabilization.

In the present study, nonpremixed DME/air coflow flames at elevated temperatures and pressures were further studied. The objective of the current work is fourfold: first, to elucidate transport effects on stabilization, parallel to the previous work [12], which focused on chemical effects; second, to demonstrate the effects of NTC chemistry on the multibrachial structure; third, to understand the transition between *kinetic* and *kinematic* stabilization mechanism and the coupling effects; and, fourth, to structure a complete regime diagram that includes both chemical and transport effects.

As a final note, practical engine conditions are highly turbulent, and the autoignition phenomenon depends on both chemistry and turbulent mixing. For example, in a DNS study, Yoo et al. [13] observed the cyclic movement of the stabilization point of a turbulent lifted ethylene jet flame in highly-heated coflow, which is a consequence of consecutive autoignition events in the high-speed jet and coflow. When fuels involve more complicated chemical characteristics, such as NTC effects, turbulence plays different and potentially competing roles. As demonstrated in a more recent computational work by Echehki and Ahmed [14], although scalar dissipation rate tends to delay ignition due to heat and radical losses from nascent kernels, enhanced mixing ensures much larger volumetric heat release rate after ignition. However, neither of these works has considered high pressure regimes and analyzed the complicating effects of NTC in detail. Therefore, in order to better understand flame stabilization and provide insights for future studies on turbulent lifted flames at elevated temperatures and pressures, the current work focuses on laminar conditions.

## 2. Computational details

An axisymmetric DME stream at 300 K is surrounded by heated coflow air at 30 atmospheres. The fuel nozzle diameter  $D$  is 0.8 mm, and the fuel and air are initially separated by an adiabatic, no-slip wall with thickness  $D/20$ . The diameter of the coflow is 3.9 mm with adiabatic, slip wall boundary conditions. This diameter was chosen to be wide enough such that further widening of the domain did not influence the computational results. Uniform inlet velocities of 2.4, 3.2, and 8.0 m/s for both streams were specified. The outlet boundary

**Table 1**  
Computational domain and number of grid points.

Inlet velocity [m/s]	2.4	3.2	8.0
$L_x$ [mm]	3.5	3.5	15
$N_x$	1536	1536	3072
$N_r$	176	176	176

condition is a convective outflow, which is a Neumann condition at steady-state.

The governing equations, transport model, and chemical model were adopted to be the same as in Deng et al. [12]. In brief, the Navier-Stokes equation with buoyancy effects in the streamwise direction and the conservation equations of mass, species, and energy were solved. The species diffusivities are determined assuming a constant, nonunity Lewis number and kept the same as in the previous work [12]. The conserved scalar mixture fraction  $Z$  is specified as unity and zero for the fuel stream and coflow, respectively, and is computed by solving a conserved scalar transport equation with unity Lewis number [15]. A DME skeletal mechanism of 39 species [16], which was reduced from the well-validated detailed mechanism of Zhao et al. [17], was adopted as the chemical model.

The governing equations with the low-Mach number formulation are solved using NGA [18]. The momentum and scalar equations are discretized with a second-order centered scheme and a third-order WENO scheme [19], respectively, on a staggered mesh. An iterative second-order semi-implicit Crank–Nicolson scheme is adopted for temporal integration [20]. The chemical source terms for the species and energy equations are integrated using the CVODE package [21].

Leveraging previous grid convergence studies [12], uniform grid spacing in the axial direction was set to  $\Delta x = 2.2\text{--}4.8 \mu\text{m}$ , depending on the case. Nonuniform grid spacing in the radial direction was set to minimum  $\Delta r = 2.5 \mu\text{m}$  to resolve the mixing layer near the thin wall, and the grid stretch rate was less than 3%. Details about the numerical discretization are summarized in Table 1.

## 3. Transport effects

Transport effects on nonpremixed coflow flame stabilization were demonstrated by fixing the coflow temperature at 900 K while varying the uniform inlet velocities as 2.4, 3.2, and 8.0 m/s. The 3.2 m/s case was computed in previous work [12].

### 3.1. Thermal and chemical structure

The heat release rate profiles for the three cases are shown in Fig. 1. A qualitative determination of the stabilization point is the most upstream point on the largest heat release contour (the leading point), colored by red. The mixture fraction iso-contours of  $Z_{st} = 0.1005$ ,  $Z = 0.2$ , and  $Z = 0.3$  are delineated in solid black lines, from right to left.

When the inlet velocity is the lowest, 2.4 m/s, a tribrachial thermal structure is observed very similar to that of the classical triple flame. The triple point at  $Z = 0.15$ , where the three large heat release branches intersect, is also the stabilization point. Some heat release can be found upstream of the tribrachial thermal structure for the partially reacting mixture at elevated temperature but is much less than the heat release from the flame structure. As the inlet velocity increases to 3.2 m/s, another branch with large heat release is found attached to the tribrachial structure around  $Z = 0.2$ . The stabilization point is, again, the same as the triple point. This structure has been analyzed in our previous work [12]. However, as the inlet velocity further increases to 8.0 m/s, the stabilization point is no longer on the tribrachial structure. Instead, it is found to be near  $Z = 0.25$  and is the intersection point of two trailing heat release branches. Attached to the leaner branch, there is a tribrachial structure that

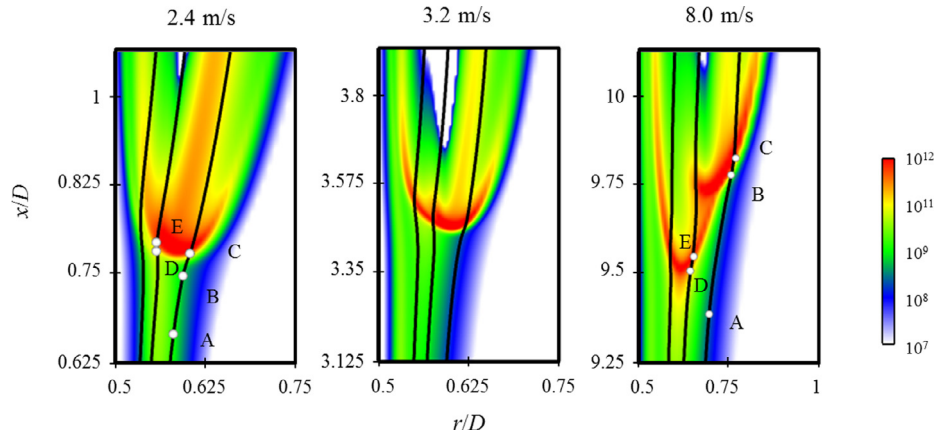


**Fig. 1.** Heat release rate [ $\text{J}/\text{m}^3 \text{ s}$ ] profiles. The iso-contours of  $Z_{st}$ ,  $Z = 0.2$ , and  $Z = 0.3$  are outlined from right to left in solid lines, respectively. The CEMA sampling points for 2.4 and 8.0 m/s cases are marked along the iso-contours. (For interpretation of the references to color in this figure, the reader is referred to the web version of this article.)

appears similar to the triple flame structure. This multibrachial structure is similar to the one found in previous work at a higher oxidizer temperature (800 K) but lower velocity (3.2 m/s) [12].

The controlling chemistry of the three cases was studied with CEMA [22,23]. Briefly, local species concentrations and temperature are sampled from the two-dimensional computation and input into CEMA to evaluate the eigenvalues of the Jacobian matrix ( $K + 1$  by  $K + 1$ , where  $K$  is the number of species) of the chemical source terms. The eigenmode associated with the eigenvalue  $\lambda_e$ , which has the largest real part among all the eigenvalues, is defined as a chemical explosive mode, if

$$\text{Re}(\lambda_e) > 0, \lambda_e = \mathbf{b}_e \mathbf{J}_\omega \mathbf{a}_e, \quad (1)$$

where  $\mathbf{b}_e$  and  $\mathbf{a}_e$  are the left and right eigenvectors, respectively, associated with  $\lambda_e$ , and  $\mathbf{J}_\omega$  is the chemical Jacobian matrix. The existence of the chemical explosive mode indicates the propensity of local mixture autoignition given an isolated, adiabatic, and constant volume environment. Furthermore, the detailed chemical reactions that contribute to the chemical explosive mode can be quantified by the explosion participation index:

$$\text{PI} = \frac{|\mathbf{b}_e \cdot \mathbf{S}| \otimes \mathbf{R}}{\text{sum}(|\mathbf{b}_e \cdot \mathbf{S}| \otimes \mathbf{R})}, \quad (2)$$

where  $\mathbf{S}$  is the stoichiometric coefficient matrix,  $\mathbf{R}$  is the vector of the net rates for the reactions, and  $\otimes$  denotes elementwise multiplication of two vectors.

In the present study, such samplings were conducted along  $Z_{st}$ ,  $Z = 0.2$ , and  $Z = 0.3$  iso-contours, as shown in Fig. 1. Based on the explosive mode and participation index, the evolution of the dominant reactions is shown in Fig. 2.

At 2.4 m/s, the dominant reactions along  $Z_{st}$  and  $\rightleftharpoons Z = 0.2$  iso-contours evolve in similar ways: upstream of the tribrachial structure (points A, B, and D), low temperature chemistry, characterized by reactions involving  $\text{CH}_3\text{OCH}_2\text{O}_2$  radicals, is active. Due to the high diffusivity of H radicals and the elevated pressure, the H radical recombination reaction ( $\text{H} + \text{O}_2 + \text{M} \rightleftharpoons \text{HO}_2 + \text{M}$ ) is important. At the most reactive region (points C and E), the H radical branching reaction ( $\text{H} + \text{O}_2 \rightleftharpoons \text{O} + \text{OH}$ ) becomes the most important chain branching reaction, indicating the transition to high temperature chemistry. On the contrary, for the 8.0 m/s case, while low temperature chemistry is still active upstream of the multibrachial structure, the dominant chain branching reaction is the hydrogen peroxide branching reaction ( $\text{H}_2\text{O}_2 + \text{M} \rightleftharpoons \text{OH} + \text{OH} + \text{M}$ ). Moreover, the dominant reactions along the  $Z_{st}$  and  $Z = 0.2$  iso-contours evolve in different ways. Along the  $Z = 0.2$  iso-contour, from point D to E, the hydrogen peroxide branching reaction is always the dominant reaction, indicating the role of low-to-intermediate temperature autoignition chemistry

[24]. Although this is the case at point A on the  $Z_{st}$  iso-contour, the H radical chain branching reaction becomes dominant at point C, the most reactive zone, indicating that the dominant chemical pathway shifts to high temperature chemistry. CEMA results for the 3.2 m/s case show similar transitions as those of the 8.0 m/s case, although their thermal structures appear different. Therefore, further computational diagnostics is needed to identify the dominant combustion mode.

### 3.2. Stabilization mechanism

The above CEMA results have demonstrated the importance of autoignition chemistry in the multibrachial structure. However, further analysis is still needed to elucidate the role that autoignition plays in the stabilization mechanism. As conducted previously [12], LFA [25] utilizes the initial conditions provided by the two-dimensional computation to provide the time history of the one-dimensional inhomogeneous autoignition. As only the diffusion processes parallel to the mixture fraction gradient direction are accounted for in this analysis, the comparison of this one-dimensional flamelet and the two-dimensional result gives the relative importance of transport parallel and normal to the mixture fraction gradient and thus the relative importance of inhomogeneous autoignition and premixed flame propagation to the stabilization mechanism.

Specifically, the unsteady flamelets were computed with FlameMaster [26]. Species mass fractions and temperature were sampled at ten times the wall thickness downstream of the inlet to avoid the influence from the recirculation zone (behind the thin wall) on the initial condition in LFA. The time history of the scalar dissipation rate was sampled along the  $Z_{st}$  iso-contour from the two-dimensional computation. The flamelet time was computed from the two-dimensional computational results, along the  $Z_{st}$  iso-contour:

$$t = \int_0^x \frac{1}{(u + u_z)(x')|Z = Z_{st}} dx'. \quad (3)$$

The axial component of the mixture fraction iso-contour propagation speed relative to the fluid convection  $u_z$  is taken into consideration in addition to the axial component of the fluid convection velocity  $u$ . The expression for  $u_z$  is adopted from Lignell et al. [27]:

$$\mathbf{u}_z = - \frac{\nabla \cdot (\rho D_z \nabla Z)}{\rho |\nabla Z|} \mathbf{n}, \quad (4)$$

where  $D_z$  is the mixture fraction diffusivity, with unity Lewis number, and  $\rho$  is the density. The normal vector  $\mathbf{n}$ , defined as

$$\mathbf{n} = \frac{\nabla Z}{|\nabla Z|}, \quad (5)$$

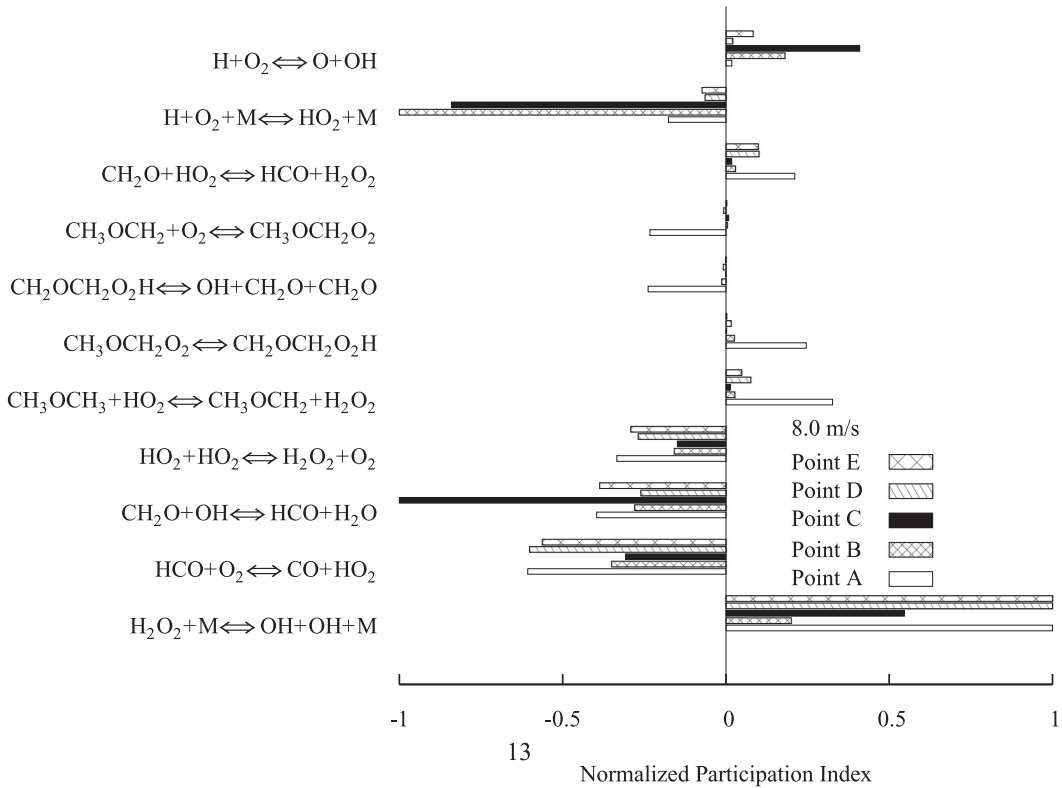
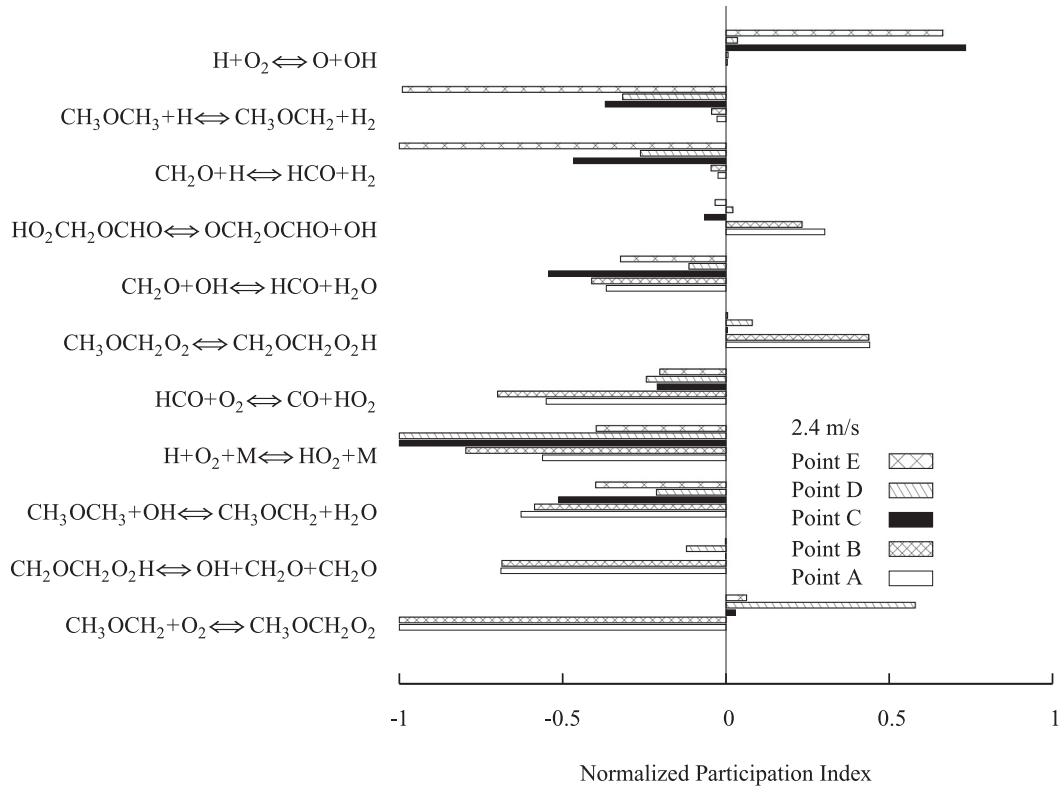


Fig. 2. Normalized participation index at 2.4 and 8.0 m/s. Sampled locations are delineated in Fig. 1.

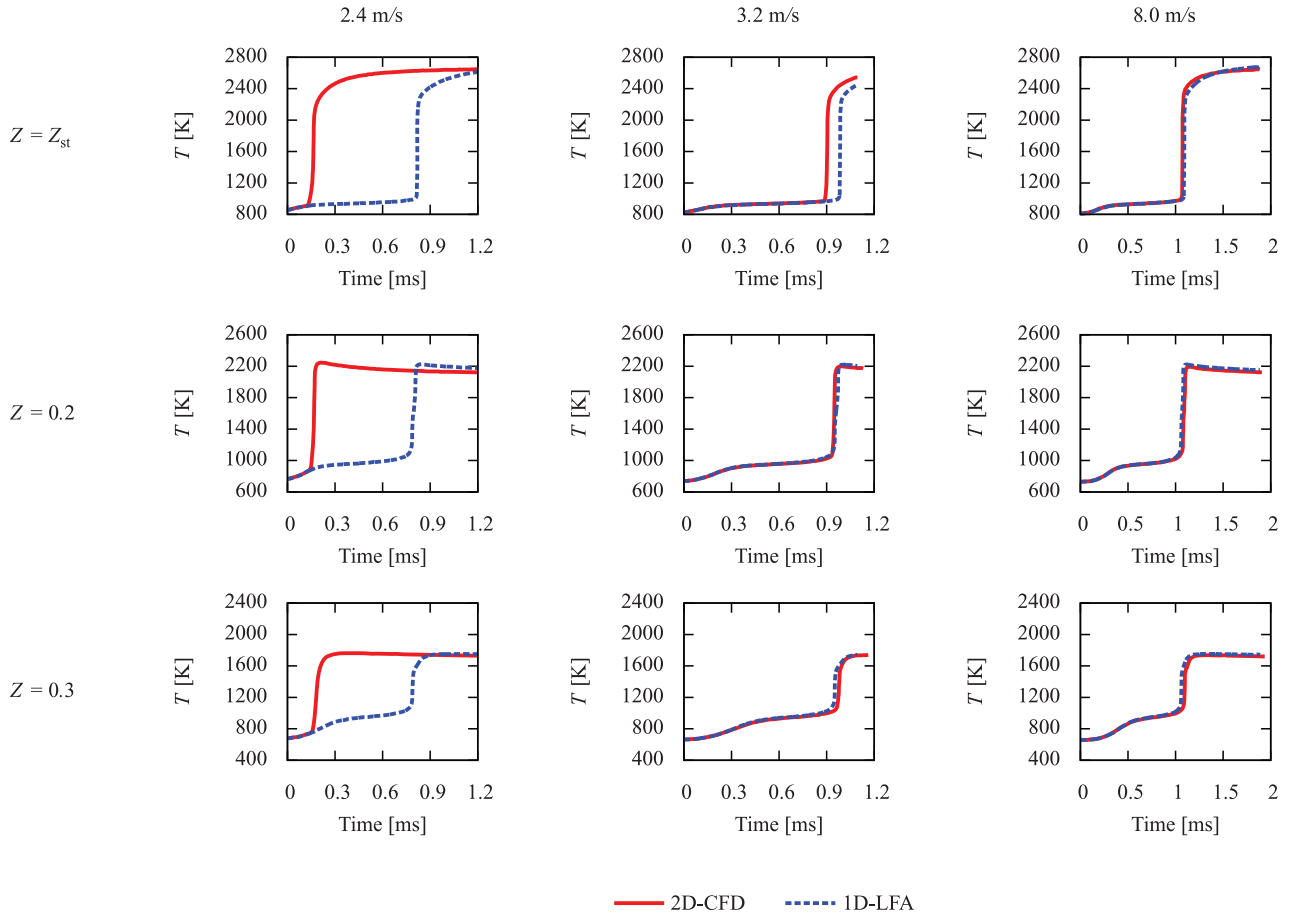


Fig. 3. Comparison between CFD and LFA results.

indicates the direction of this diffusion induced relative velocity. Only the scalar dissipation rate at stoichiometric mixture fraction is sampled from the two-dimensional computations; the dissipation rates at other mixture fractions were computed assuming the following form [28]:

$$\chi(Z) = \chi(Z_{st}) \frac{\exp(-2[\operatorname{erfc}^{-1}(2Z)]^2)}{\exp(-2[\operatorname{erfc}^{-1}(2Z_{st})]^2)} = \chi(Z_{st})f(Z; Z_{st}). \quad (6)$$

Validation of this expression was provided in previous work [12].

The Lagrangian time history profiles of the two-dimensional computation and one-dimensional LFA are shown in Fig. 3. For each inlet velocity case, the temperature profiles are compared along  $Z_{st}$ ,  $Z = 0.2$ , and  $Z = 0.3$ .

For the 2.4 m/s case, LFA fails to match the two-dimensional result at all three mixture fractions, indicating that transport processes normal to the mixture fraction gradient are crucial, which further indicates that flame propagation is the dominant stabilization mechanism. At 3.2 m/s, LFA slightly lags behind the two-dimensional result at  $Z_{st}$  but matches well at  $Z = 0.2$  and  $Z = 0.3$ . Recalling the heat release profile in Fig. 1, these results indicate that the tetrabrachial structure consists of a tribrachial structure, at which flame propagation is not negligible, and the richer branch that intersects with the tribrachial flame is an autoignition front, whose response is well captured with the one-dimensional flamelet model. As a result, stabilization of the 3.2 m/s case is characterized as a mixed mode of inhomogeneous autoignition and premixed flame propagation, depending on the local mixture fraction. At 8.0 m/s, LFA agrees well with the two-dimensional result at all mixture fractions, indicating that the transport processes normal to the mixture fraction gradient are negligible.

Therefore, the stabilization mechanism is characterized as inhomogeneous autoignition.

### 3.3. Autoignition and flame interaction

As shown by LFA, under some conditions, inhomogeneous autoignition and premixed flame propagation both contribute to flame stabilization, resulting in a multimode stabilized regime. Furthermore, the interaction between autoignition and flame propagation is tightly coupled. If the thermal structure is mainly kinetically stabilized, heat and radicals generated by autoignition will modify the downstream thermal and chemical environment and thus the local flame speed. On the contrary, if stabilization is mainly kinematic in nature then heat and radicals generated by the flame can back diffuse upstream, modifying the reactivity upstream.

To demonstrate these complex interactions and understand the transition between kinetic and kinematic stabilization mechanisms, the LFA results for the 2.4 m/s case were further analyzed. As shown in Fig. 3, if there was a kinetically stabilized inhomogeneous autoignition front, this front would stabilize further downstream than the kinematically stabilized flame front. Although not shown, CEMA of these LFA solutions show the same evolution of the controlling chemistry as the 8.0 m/s case. In particular, the low-to-intermediate temperature hydrogen peroxide chain branching reaction dominates the transition to autoignition. Therefore, the nature and the qualitative structures of the inhomogeneous autoignition fronts, as predicted by LFA in Fig. 3 for the two lower inlet velocity cases, are essentially the same as the 8.0 m/s case.

A general description of the initiation of these multibrachial inhomogeneous autoignition fronts in all three cases is that, due to

radical accumulation and heat release, the controlling chemistry shifts from low temperature chemistry, represented by  $\text{CH}_3\text{OCH}_2\text{O}_2$  reactions, to hydrogen peroxide branching reactions. At some mixture fractions, higher temperatures and more oxidizer supply enable the dominant chemistry to transition further to high temperature chemistry, as characterized by the H radical branching reaction. As shown in Fig. 4, there are double or triple heat release peaks, depending on the mixture fraction. However, for all mixture fractions, these peaks correlate very well with the inflection points on the temperature profiles and peaks on the OH radical profiles. Comparing them with the  $\text{CH}_3\text{OCH}_2\text{O}_2$  radical profile, it is clear that low temperature chemistry results in the first peak of heat release profile and produces OH radicals. Hydrogen peroxide accumulates until it decomposes at the second heat release peak and produces OH radicals through  $\text{H}_2\text{O}_2 + \text{M} \rightleftharpoons \text{OH} + \text{OH} + \text{M}$ . At  $Z_{\text{st}}$  and  $Z = 0.2$ , there is a third heat release and OH radical peak, which is due to the  $\text{H} + \text{O}_2 \rightleftharpoons \text{O} + \text{OH}$  reaction. At  $Z_{\text{st}}$ , the second and third peaks appear to be much closer compared with those at  $Z = 0.2$ , probably due to higher temperature and more abundant oxidizer, such that the H radical chain branching reaction is activated earlier. Due to the lack of oxidizer, the third peak is not observed at  $Z = 0.3$ .

The multibrachial structure of the inhomogeneous autoignition front is due to the variation in ignition delay time at different mixture fractions. As shown in Fig. 1, the stabilization point is determined based on the threshold value of heat release rate. Therefore, the ignition delay time of inhomogeneous autoignition can be determined accordingly, which corresponds to the heat release rate peak that exceeds  $10^{12} \text{ J/m}^3 \cdot \text{s}$ . For the 8.0 m/s case shown in Fig. 5, the mixture is autoignited first at  $Z = 0.24$ , which corresponds to the stabilization point in Fig. 1. Although the first stage ignition delay time, defined by the first heat release peak through low temperature chemistry, increases monotonically as mixture fraction increases (temperature decreases), the overall ignition delay time reaches the shortest at  $Z = 0.24$  due to the compensation of larger heat release after the first ignition stage [8], as shown in Fig. 4. As a consequence, although low temperature chemistry is not the dominant chemical pathway at the stabilization point for the *kinetically* stabilized case, it still influences the location of the stabilization point through the mixture fraction dependent heat and radical accumulation upstream.

However, although the cases in the current study are all initiated by inhomogeneous autoignition, the stabilization of the final structure depends on the dominant transport processes, which are influenced by the inlet velocities. At 8.0 m/s, heat and radical back diffusion from the autoignition front to upstream is not able to keep up with convection; therefore, the reacting front is *kinetically* stabilized. At 3.2 m/s, as flow convection is weaker, diffusion processes become inherently important and couple with chemical reactions to induce a flame front propagating upstream. However, the propagation speed of the flame varies with composition and temperature. As a consequence, around  $Z_{\text{st}}$ , where higher temperature and near-stoichiometric mixture composition enable higher local flame speed, the propagation of the reacting front balances the incoming flow velocity. However, such a balance fails at richer mixture fractions where *kinetic* stabilization dominates due to enhanced NTC-affected autoignition at richer mixture fractions as demonstrated in Fig. 5. At 2.4 m/s, back diffusion is important at all mixture fractions such that the reacting front propagates upstream at the local flame speed, as determined by the local composition and temperature. Due to the increased temperature and species stratification and the reduced thermal and radical accumulation from autoignition, the propagation speed of this reacting front is less influenced by inhomogeneous autoignition, as demonstrated with CEMA and LFA. The structure of this *kinematically* stabilized reacting front, which is generally tribrachial, is therefore determined by the variation of the local flame speed.

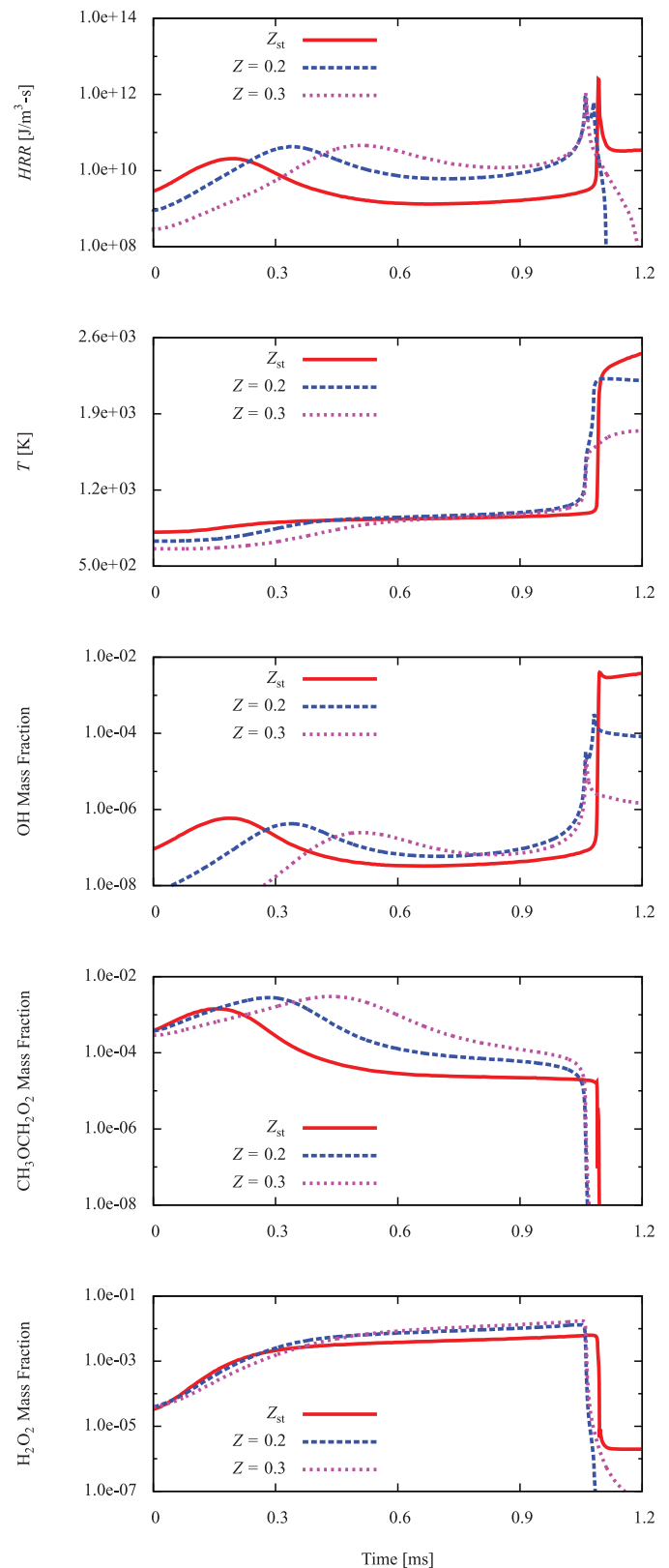


Fig. 4. LFA profiles along  $Z_{\text{st}}$ ,  $Z = 0.2$ , and  $Z = 0.3$  of the 8.0 m/s case.

#### 4. Stabilization regime diagram

The above sections have demonstrated the transport effects on the thermal and chemical structure of the lifted coflow flames as well as the stabilization mechanisms. Combining these results with

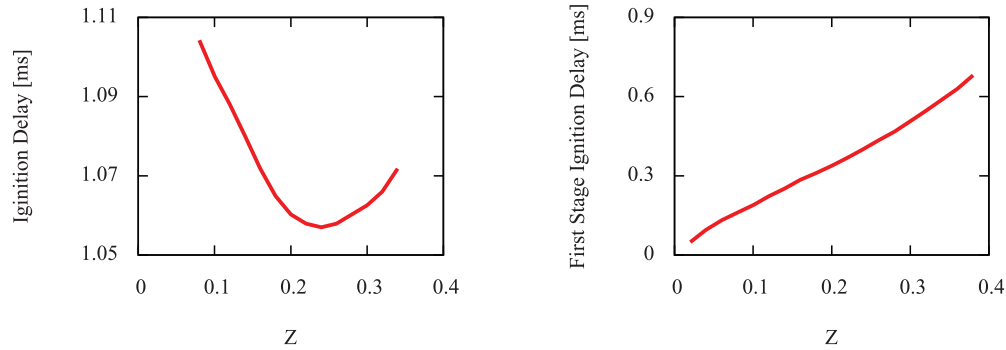


Fig. 5. LFA results on the mixture fraction dependent total and first stage ignition delay times of the 8.0 m/s case.

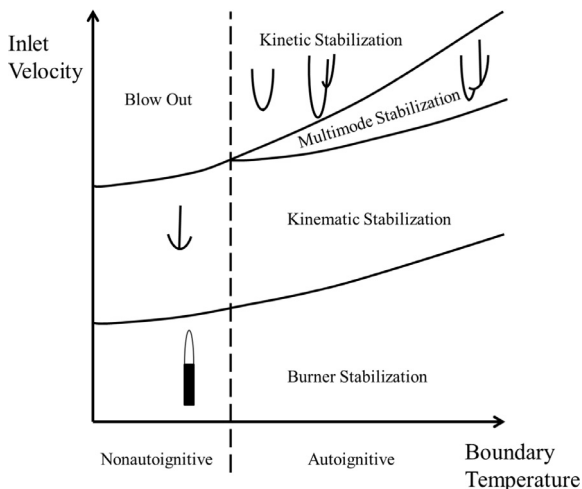


Fig. 6. A qualitative regime diagram for the stabilization mechanisms as the boundary temperature and inlet velocity vary.

the chemical effects demonstrated by changing the coflow boundary temperature from our previous study [12], a two-dimensional stabilization regime diagram is proposed, as shown in Fig. 6.

Qualitatively, when the boundary temperature is not high enough to activate autoignition, the lifted flame appears as the classical triple flame and is *kinematically* stabilized. When the inlet velocity is below or above certain threshold values, the triple flame becomes attached to the burner or is blown out, respectively.

As the boundary temperature is elevated enough to activate autoignition, increasing the inlet velocity while keeping constant boundary temperature, the flame stabilization mechanism transits from burner stabilization to a *kinematic* balance between flame speed and incoming flow velocity, then to multimode stabilization influenced by both flame propagation and inhomogeneous autoignition, and finally to *kinetic* stabilization governed by inhomogeneous autoignition. It is expected that the crossover velocities between regimes increase with increasing boundary temperature because flame speed generally increases at higher temperature. However, it is difficult to quantify these boundaries as local composition and temperature vary in the streamwise direction, and, therefore, the reference flame speed cannot be calculated based on the upstream boundary conditions. Furthermore, local flame front curvature, cross-stream species stratification, and flow divergence approaching the flame front also modify the flame speed. As a consequence, only a qualitative trend is demonstrated in Fig. 6.

Similarly, if the boundary temperature increases at fixed inlet velocity, transition from blow out to burner stabilized regimes is

achieved by moving horizontally across the regime diagram, which was discussed in our previous work [12].

## 5. Conclusions

In the present work, axisymmetric two-dimensional laminar nonpremixed DME lifted coflow flames at elevated temperatures and pressures were computed. Transport effects on the structure and stabilization mechanism were demonstrated by changing the inlet velocities while keeping the coflow boundary temperature constant.

The heat release rate profiles were examined to describe the thermal structure, and CEMA was used to demonstrate the evolution of the controlling chemistry. Moreover, one-dimensional LFA that captures inhomogeneous autoignition was adopted to identify the dominant transport directions and therefore determine the dominant combustion mode and stabilization mechanism.

At 2.4 m/s, the lifted flame appears to be the classical triple flame stabilized by the balance between the local flame speed and incoming flow velocity, and it is therefore characterized as *kinematically* stabilized. As the inlet velocity increases, such a balance cannot be achieved at certain mixture fractions. Instead, inhomogeneous autoignition becomes the dominant combustion mode. As a consequence, the multibranch structure is stabilized by both premixed flame propagation and inhomogeneous autoignition and is characterized as multimode stabilized. At 8.0 m/s, the *kinematic* balance cannot be achieved anywhere in the flow field due to lack of back diffusion. A *kinetically* stabilized inhomogeneous autoignition front is formed where diffusion processes along the mixture fraction iso-contours are negligible compared to the gradient direction. In the *kinetically* stabilized autoignition front, NTC chemistry plays an important role, dictating the stabilization point. This point occurs at the mixture fraction with the shortest ignition delay time, which is a compromise of the first stage autoignition delay time and heat release from low temperature chemistry. Conversely, the *kinematically* stabilized flames are less affected by NTC chemistry, with only a minor effect on the local flame speed resulting from the upstream accumulation of heat and radicals. Combined with the extended stabilization regimes demonstrated in our previous study [12], an extended two-dimensional stabilization regime diagram was constructed, considering both transport (inlet velocity) and chemical (coflow boundary temperature) effects.

This work represents a significant contribution to the understanding of nonpremixed flames at autoignitive conditions. However, practical engines conditions are turbulent. In such flows, the unsteady motion of eddies and enhanced temperature and species dissipation can strongly influence stabilization. Therefore, further investigation is required to understand the role of turbulence in the stabilization of such flames and determine whether the stabilization mechanism is modified or not.

## Acknowledgments

This research was supported in part by the **Air Force Office of Scientific Research** (AFOSR) under the technical management of Dr. Mitat Birkan.

## References

- [1] J. Buckmaster, Edge-flames, *Prog. Energy Combust. Sci.* 28 (5) (2002) 435–475, doi:10.1016/S0360-1285(02)00008-4.
- [2] S.H. Chung, Stabilization, propagation and instability of tribrachial triple flames, *Proc. Combust. Inst.* 31 (1) (2007) 877–892, doi:10.1016/j.proci.2006.08.117.
- [3] B.C. Choi, K.N. Kim, S.H. Chung, Autoignited laminar lifted flames of propane in coflow jets with tribrachial edge and mild combustion, *Combust. Flame* 156 (2) (2009) 396–404, doi:10.1016/j.combustflame.2008.10.020.
- [4] B.C. Choi, S.H. Chung, Autoignited laminar lifted flames of methane/hydrogen mixtures in heated coflow air, *Combust. Flame* 159 (4) (2012) 1481–1488, doi:10.1016/j.combustflame.2011.11.016.
- [5] B.C. Choi, S.H. Chung, Autoignited laminar lifted flames of methane, ethylene, ethane, and n-butane jets in coflow air with elevated temperature, *Combust. Flame* 157 (12) (2010) 2348–2356, doi:10.1016/j.combustflame.2010.06.011.
- [6] F. Battin-Leclerc, Detailed chemical kinetic models for the low-temperature combustion of hydrocarbons with application to gasoline and diesel fuel surrogates, *Prog. Energy Combust. Sci.* 34 (2008) 440–498.
- [7] J. Zádor, C.A. Taatjes, R.X. Fernandes, Kinetics of elementary reactions in low-temperature autoignition chemistry, *Prog. Energy Combust. Sci.* 37 (4) (2011) 371–421, doi:10.1016/j.pecs.2010.06.006.
- [8] C.K. Law, P. Zhao, NTC-affected ignition in nonpremixed counterflow, *Combust. Flame* 159 (3) (2012) 1044–1054.
- [9] P. Zhao, C.K. Law, The role of global and detailed kinetics in the first-stage ignition delay in NTC-affected phenomena, *Combust. Flame* 160 (11) (2013) 2352–2358.
- [10] S. Deng, P. Zhao, D. Zhu, C.K. Law, NTC-affected ignition and low-temperature flames in nonpremixed DME/air counterflow, *Combust. Flame* 161 (8) (2014) 1993–1997, doi:10.1016/j.combustflame.2014.01.020.
- [11] A. Krisman, E.R. Hawkes, M. Talei, A. Bhagatwala, J.H. Chen, Polybrachial structures in dimethyl ether edge-flames at negative temperature coefficient conditions, *Proc. Combust. Inst.* 35 (2015) 999–1006, doi:10.1016/j.proci.2014.05.129.
- [12] S. Deng, P. Zhao, M.E. Mueller, C.K. Law, Autoignition-affected stabilization of laminar nonpremixed DME/air coflow flames, *Combust. Flame* 162 (2015) 3437–3445.
- [13] C.S. Yoo, E.S. Richardson, R. Sankaran, J.H. Chen, A DNS study on the stabilization mechanism of a turbulent lifted ethylene jet flame in highly-heated coflow, *Proc. Combust. Inst.* 33 (2011) 1619–1627.
- [14] T. Echekki, S.F. Ahmed, Autoignition of n-heptane in a turbulent co-flowing jet, *Combust. Flame* (2015), doi:10.1016/j.combustflame.2015.07.020.
- [15] H. Pitsch, N. Peters, A consistent flamelet formulation for non-premixed combustion considering differential diffusion effects, *Combust. Flame* 114 (1–2) (1998) 26–40, doi:10.1016/S0010-2180(97)00278-2.
- [16] A. Bhagatwala, Z. Luo, H. Shen, J.A. Sutton, T. Lu, J.H. Chen, Numerical and experimental investigation of turbulent DME jet flames, *Proc. Combust. Inst.* 35 (2015) 1157–1166.
- [17] Z. Zhao, M. Chaos, A. Kazakov, F.L. Dryer, Thermal decomposition reaction and a comprehensive kinetic model of dimethyl ether, *Int. J. Chem. Kinet.* 40 (1) (2008) 1–18.
- [18] O. Desjardins, G. Blanquart, G. Balarac, H. Pitsch, High order conservative finite difference scheme for variable density low Mach number turbulent flows, *J. Comput. Phys.* 227 (15) (2008) 7125–7159, doi:10.1016/j.jcp.2008.03.027.
- [19] X. Liu, S. Osher, T. Chan, Weighted Essentially Non-oscillatory Schemes, *J. Comput. Phys.* 115 (1) (1994) 200–212, doi:10.1006/jcph.1994.1187.
- [20] C.D. Pierce, *Progress-Variable Approach for Large-Eddy Simulation of Turbulent Combustion* (Ph.D. thesis), Stanford University, 2001.
- [21] S.D. Cohen, A.C. Hindmarsh, P.F. Dubois, CVODE, A stiff/nonstiff ODE solver in C, *Comput. Phys.* 10 (2) (1996) 138, doi:10.1063/1.4822377.
- [22] T.F. Lu, C.S. Yoo, J.H. Chen, C.K. Law, Three-dimensional direct numerical simulation of a turbulent lifted hydrogen jet flame in heated coflow: a chemical explosive mode analysis, *J. Fluid Mech.* 652 (2010) 45–64, doi:10.1017/S002211201000039X.
- [23] R. Shan, C.S. Yoo, J.H. Chen, T. Lu, Computational diagnostics for n-heptane flames with chemical explosive mode analysis, *Combust. Flame* 159 (10) (2012) 3119–3127, doi:10.1016/j.combustflame.2012.05.012.
- [24] C.K. Westbrook, Chemical kinetics of hydrocarbon ignition in practical combustion systems, *Proc. Combust. Inst.* 28 (2000) 1563–1577, doi:10.1016/S0082-0784(00)80554-8.
- [25] H. Pitsch, M. Chen, N. Peters, Unsteady flamelet modeling of turbulent hydrogen-air diffusion flames, *Symp. (Int.) Combust.* 27 (1) (1998) 1057–1064, doi:10.1016/S0082-0784(98)80506-7.
- [26] H. Pitsch, FlameMaster: a C++ computer program for 0D combustion and 1D laminar flame calculations.
- [27] D.O. Lignell, J.H. Chen, P.J. Smith, T. Lu, C.K. Law, The effect of flame structure on soot formation and transport in turbulent nonpremixed flames using direct numerical simulation, *Combust. Flame* 151 (1–2) (2007) 2–28, doi:10.1016/j.combustflame.2007.05.013.
- [28] N. Peters, *Turbulent Combustion*, Cambridge University Press, 2000.



# Flame dynamics in oscillating flows under autoignitive conditions



Sili Deng<sup>a</sup>, Peng Zhao<sup>a,b</sup>, Michael E. Mueller<sup>a,\*</sup>, Chung K. Law<sup>a</sup>

<sup>a</sup> Department of Mechanical and Aerospace Engineering, Princeton University, Princeton, NJ 08544, USA

<sup>b</sup> Department of Mechanical Engineering, Oakland University, Rochester, MI 48309, USA

## ARTICLE INFO

### Article history:

Received 15 February 2016

Revised 1 April 2016

Accepted 2 April 2016

### Keywords:

Flame dynamics

Nonpremixed coflow flame

Autoignition

Negative temperature coefficient (NTC)

Dimethyl ether (DME)

## ABSTRACT

The structure and dynamics of laminar nonpremixed dimethyl ether (DME)/air coflow flames were investigated at elevated temperatures and pressures. Computations with detailed chemistry were performed for DME and heated coflow air at 30 atm with uniform but sinusoidally oscillating inlet velocities. These unsteady cases were compared with the steady results from Deng et al. (2015)[14] to elucidate the effect of oscillation frequency on the flame dynamics. To benchmark the unsteady cases, a normalized displacement velocity was defined to differentiate flame propagation from autoignition, and this definition was validated against the steady cases. In the oscillating reacting flow, transition between a multibrachial autoignition front and a tribrachial flame occurs periodically. However, unlike the harmonic velocity oscillation, the combustion mode transition is hysteretic. The oscillation cycle starts with the largest inlet velocity, with the multibrachial thermal structure, located downstream, being governed by autoignition chemistry. As flow velocity decreases, the autoignition front moves upstream and transitions to a tribrachial flame near the lower velocity limit, similar to the steady flow, as autoignition chemistry becomes weaker with decreasing upstream residence time. As the flow velocity increases again, the tribrachial flame is convected downstream, and, ultimately, due to the radical and heat accumulation in time, autoignition eventually occurs and becomes the dominant pathway. The finite induction time for autoignition results in the hysteretic behavior during the decreasing- and increasing-velocity cycles, which diminishes at lower oscillation frequency as there is more time for chemistry to respond to the hydrodynamic changes and consequently approach steady state. At the relatively low oscillation frequencies investigated in the current study, first-stage NTC chemistry is less affected by flow dynamics with only second-stage autoignition and flame chemistry, which accounts for the majority heat release, coupled with the flow oscillation.

© 2016 The Combustion Institute. Published by Elsevier Inc. All rights reserved.

## 1. Introduction

Fuel injection and its subsequent mixing and reaction with either a coflowing air stream or a highly turbulent oxidizing environment is an integral process in the operation of many combustors. Due to experimental and computational limitations, simplifications are usually made to obtain fundamental understanding of these reacting flows that are then extrapolated to more complex conditions. For example, laminar nonpremixed coflow flames at normal ambient temperatures have been studied to elucidate the coupling between fluid dynamics and chemistry, leading to the observation that, in the fuel and oxidizer mixing layer, a two-dimensional tribrachial structure (also known as triple flame) [1] is obtained. Specifically, both lean and rich premixed

flame branches and a trailing diffusion flame tail intersect at a triple point. Based on the observation of such tribrachial laminar flames, the partially premixed flamelet model [2] was proposed to explain lifted flames in nonpremixed turbulent jets [3].

Previous studies have indicated that nonpremixed coflow flame structure can be modified in unsteady flows. For example, in the experimental investigation of Strawa and Cantwell [4], flow instability and flame breakup was achieved by imposing a small-amplitude, periodic velocity fluctuation to nonpremixed jet flames at elevated pressures and low Reynolds numbers. Later, in the computational study of Sánchez-Sanz et al. [5], perturbation frequency effects on the thermal and chemical properties of the flame in such periodically time-varying flows were evaluated. Three regimes were found depending on the flame's Strouhal number,  $S = Df/2U$ , with  $D$  and  $f$  denoting the fuel jet diameter and perturbation frequency, respectively. For small Strouhal numbers ( $S = 0.1$ ), perturbations can travel far downstream, resulting in an oscillating flame. Flame surface flickering was observed when  $S \approx 0.2$ ,

\* Corresponding author.

E-mail addresses: [silideng@gmail.com](mailto:silideng@gmail.com) (S. Deng), [muellerm@princeton.edu](mailto:muellerm@princeton.edu) (M.E. Mueller).

and vigorous flame pinch-off was observed at  $S = 0.5$ . Larger values of  $S$  confine the oscillation to the jet's near-exit region with the pulsation having minimal effects on temperature and concentration values. The unsteadiness in flickering flames also increases pollutant formation, such as soot [6] and carbon monoxide [7]. Mohammed et al. [8] followed by Dworkin et al. [9] conducted computational and experimental studies of 20 Hz periodically-forced methane/air coflow diffusion flames. Acetylene production increased [8] and the oxidation of CO to CO<sub>2</sub> was inhibited [9] in the downstream region of the flame at certain times during the flame's cyclic history.

Although demonstrating unsteady effects on flow-chemistry coupling, these experimental and computational investigations mainly focused on simple fuels, such as methane, and were limited to nonautoignitive conditions. However, as demonstrated by Chung and co-workers through a series of experiments on laminar lifted C<sub>0</sub> to C<sub>8</sub> flames in heated coflow, autoignition can be activated even at atmospheric pressure [10,11]. Although flames were initiated by autoignition, the lifted height did not always correlate well with the ignition delay time. Computationally, Krisman et al. [12] demonstrated that, under more realistic engine conditions of elevated temperature and pressure with practical fuels that have more complex chemical kinetics, the transport-chemistry coupling becomes more complicated. Depending on the conditions, either the traditional tribrachial flame or autoignition can be dominant. Their findings were confirmed and further discussed by Deng et al. [13,14] through a series of computational studies of nonpremixed dimethyl ether (DME)/air coflow flames at 30 atm with varying inlet velocities and coflow temperatures, recognizing that DME possesses the low-temperature chemistry (LTC), negative temperature coefficient (NTC) behavior. A regime diagram was proposed demonstrating that the tribrachial flame is favored at lower inlet velocity and higher coflow temperature, while autoignition is dominant at higher inlet velocity and relatively lower coflow temperature.

In the present study, unsteady nonpremixed DME/air coflow flames under autoignitive conditions are computationally studied to elucidate the coupling between unsteady fluid dynamics and chemical kinetics. Various oscillation frequencies were imposed on the inlet velocity, with the maximum and minimum velocities maintained the same as those in the previous steady study [14], which correspond to an autoignition front and a tribrachial flame, respectively. The current study focuses on low frequency oscillation ranging from 25 to 100 Hz, which covers buoyancy-driven instability frequencies [8,9] and acoustic-driven oscillation frequencies in gas turbines [15]. The objective of the current study is three-fold. The first objective is to capture the transition in combustion mode. As the steady cases correspond to different combustion modes, it is expected that, at certain frequencies of velocity oscillation, the dominant combustion process will shift between the nonpremixed tribrachial flame mode and the autoignition mode. The second objective is to assess the thermal and chemical differences during such transition and to elucidate the transition mechanism. The third objective is to demonstrate the effects of oscillation frequency on the coupling of fluid dynamics and chemical kinetics.

## 2. Computational details

The geometry in this work is the same as that in Deng et al. [14]. Briefly, axisymmetric coflow flames at 30 atmospheres were computed, in which a 300 K DME stream is surrounded by a 900 K air stream. The diameter ( $D$ ) of the fuel nozzle is 0.8 mm, which is 20 times the thickness of the adiabatic, no-slip wall, separating fuel and coflow. The outer diameter of the coflow is 3.9 mm. Adiabatic, slip wall conditions were specified at the outer radial

boundary. The same inlet velocities were imposed for both streams and are uniform in space and sinusoidally oscillating in time. The maximum (8.0 m/s) and minimum (2.4 m/s) velocities were set to match the fastest and slowest steady cases as in Deng et al. [14]. Three oscillation frequencies (25, 50, and 100 Hz) were investigated, with the maximum Strouhal number, based on the velocity and jet radius, estimated to be less than 0.02 to avoid flame pinch-off. The domain length is 15 mm, with a convective outflow boundary condition. The computational results were not affected by further widening or lengthening of the domain. Discretization of the domain was guided by previous convergence studies [13], with a 3072 ( $x$ ) by 176 ( $r$ ) grid. Uniform spacing in the axial direction was set to  $\Delta x = 4.8 \mu\text{m}$ , and nonuniform spacing in the radial direction was set to minimum  $\Delta r = 2.5 \mu\text{m}$  to resolve the mixing layer near the thin wall. The grid stretch rate is less than 3%.

The Navier–Stokes equations with buoyancy effects in the streamwise direction and the conservation equations of mass, species, and temperature were solved. The species diffusivities were determined assuming constant, nonunity Lewis numbers and kept the same as in Deng et al. [13]. The conserved scalar mixture fraction ( $Z$ ) was specified as unity and zero for the fuel stream and coflow, respectively, and was computed by solving a conserved scalar transport equation with unity Lewis number [16]. DME was chosen as the fuel, for it is one of the simplest fuels that has NTC chemistry [17], as noted earlier. A skeletal mechanism of 39 species [18], which was reduced from the well-validated detailed mechanism of Zhao et al. [19], was adopted as the chemical model.

A low-Mach number code NGA [20] was adopted to solve the discretized governing equations on a staggered mesh. A second-order centered scheme was used for the momentum equations, while a third-order WENO scheme [21] was used for the scalar equations. An iterative second-order semi-implicit midpoint scheme was adopted for temporal integration [22] utilizing Strang splitting between transport and chemistry in the scalar equations [23]. The chemical source terms for the species and temperature equations were integrated using the CVODE package [24].

## 3. Results and discussion

In this section, the thermal structure of the unsteady nonpremixed DME/air coflow flame is first described and compared qualitatively with the previous steady study by Deng et al. [14]. The definition of normalized displacement velocity is then introduced and validated against the steady cases to differentiate the combustion modes. Finally, oscillation frequency effects on the evolution of the combustion modes are analyzed.

### 3.1. Thermal structure

As the largest and smallest inlet velocity cases were designed to match the two extreme cases in Deng et al. [14], which are of different thermal structures, it is expected that similar thermal structures will be obtained. Furthermore, these thermal structures might transition back and forth in response to the oscillating flow field. Indeed, such transitions were observed for all three frequencies. For example, the evolution of the thermal structure of the 100 Hz case, in terms of the heat release rate profile, is demonstrated in Fig. 1. The oscillation cycle starts with the largest inlet velocity of 8.0 m/s, and the minimum inlet velocity (2.4 m/s) is achieved at half cycle.

At 8.0 m/s, the multibrachial thermal structure is located furthest downstream. The leading point, which is defined as the most upstream point that has the heat release rate value of  $10^{12} \text{ W/m}^3$ , is located at mixture fraction  $Z = 0.24$ . As the inlet velocity decreases, the multibrachial structure moves upstream, without obvious change of the leading point location, in terms of mixture

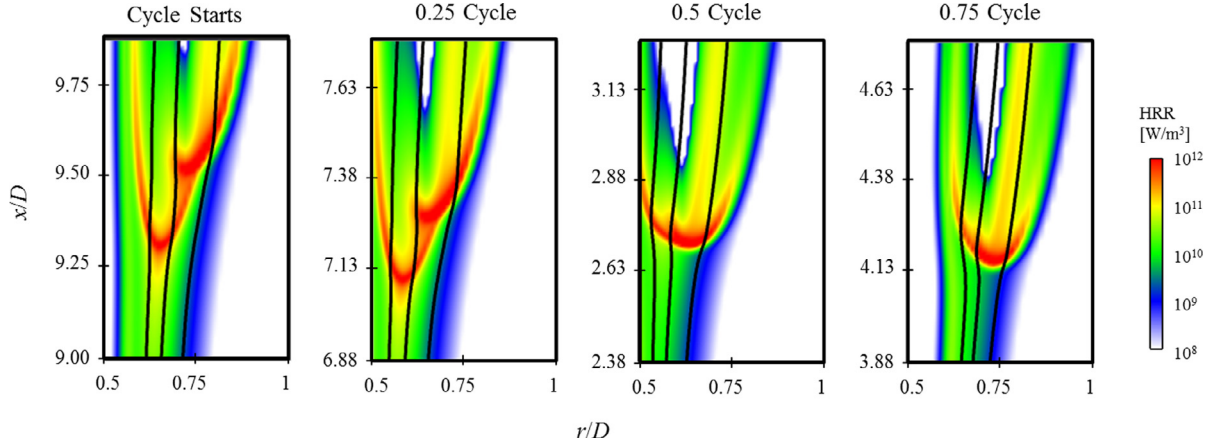


**Fig. 1.** Heat release rate [ $\text{W/m}^3$ ] profile evolution during one oscillation cycle at 100 Hz. The iso-contours of  $Z_{st} = 0.1$ ,  $Z = 0.2$ , and  $Z = 0.3$  are outlined from right to left in solid lines, respectively.

fraction. When the inlet velocity reaches its minimum, the multi-brachial structure transitions to a tribrachial structure, and the leading point switches to  $Z = 0.14$ . As the flow velocity increases, the tribrachial structure is pushed downstream, and both its tribrachial shape and its leading point mixture fraction remain unchanged. The thermal structure returns to that of multi-brachial when the flow velocity further increases. Such transitions in structure repeat once a new oscillation cycle starts.

### 3.2. Differentiation of combustion mode

As mentioned in the Introduction, Deng et al. [14] were able to relate the morphology of the thermal structures to two different combustion modes: tribrachial flame and autoignition. Specifically, at steady state, the multi-brachial structure in the 8.0 m/s case is an autoignition front, while the 2.4 m/s case is a tribrachial flame. In this previous study, species mass fraction profiles at the inlet of the two-dimensional computation were treated as the initial conditions for one-dimensional Lagrangian Flamelet Analysis [25], which only considers diffusion processes parallel to the mixture fraction gradient and neglects those in the normal direction. When the LFA prediction agreed with the CFD result, transport in the normal direction of the mixture fraction gradient was negligible, and autoignition was the dominant combustion process. However, due to the unsteadiness in the current study, such comparison between LFA and CFD is no longer applicable, and a new criterion to differentiate the modes of tribrachial flame and autoignition needs to be identified and validated against the steady cases.

A density-weighted displacement speed,  $S_d$ , is often used to distinguish between deflagrations and spontaneous ignition fronts in HCCI combustion [26], which is defined from an iso-line of species  $k$  as [27,28]:

$$S_d = \frac{1}{\rho_u |\nabla Y_k|} \left( \dot{\omega}_k - \frac{\partial \rho Y_k V_{j,k}}{\partial x_j} \right), \quad (1)$$

where  $Y_k$ ,  $V_{j,k}$ , and  $\dot{\omega}_k$  denote species mass fraction, diffusion velocity in the  $j$ -direction, and net production rate, respectively, and  $\rho_u$  is the density of the unburnt mixture. The choice of species  $k$  and its iso-line value can be ambiguous. Therefore, major products, such as  $\text{CO}_2$ ,  $\text{H}_2\text{O}$ ,  $\text{H}_2$ ,  $\text{CO}$ , and combinations of these products have been tested, and the sampling location is chosen as the leading point, as defined above, to enable further comparison with the steady cases.  $S_d$  at the leading point is insensitive to the choice of species in the current study, for less than 5% difference was observed across all the combinations. Consequently,  $\text{H}_2\text{O}$  was chosen for simplicity. Both the laminar flame speed  $S_L$  and the unburnt

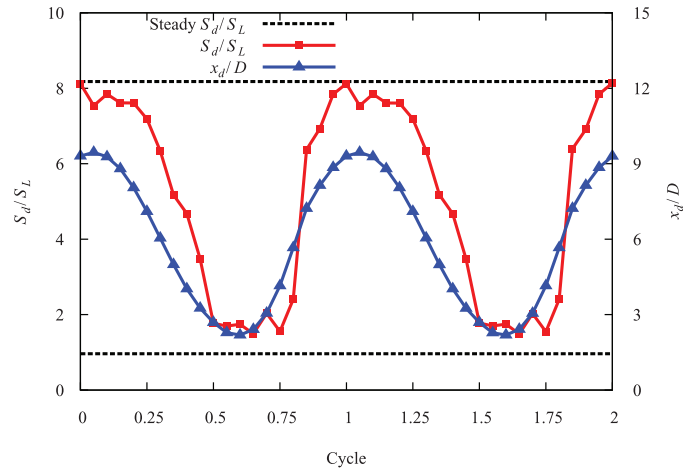


**Fig. 2.** Normalized displacement velocity (red) and leading point location (blue) time history profiles at 100 Hz. (For interpretation of the references to color in this figure legend, the reader is referred to the web version of this article.)

mixture density  $\rho_u$  were obtained from laminar flame speed calculations using the FlameMaster code [29]. The composition and temperature boundary conditions for the laminar flame speed calculations were based on the sampled mixture fraction at the leading point and linearly interpolated, in the mixture fraction space, between the corresponding inlet values of the fuel and coflow streams.

Following the above procedure, displacement velocities were calculated for all three oscillation frequency cases, with 20 points per cycle, to demonstrate their evolution. Furthermore, as shown in Fig. 2,  $S_d/S_L$  for the two steady cases (2.4 and 8.0 m/s) were similarly calculated to validate this definition of normalized displacement velocity and differentiate between tribrachial flame and autoignition. For clarity, only the 100 Hz case is included in Fig. 2 to elucidate its evolution, and the effect of the oscillation frequency will be discussed in Section 3.3.

The normalized displacement velocities for the steady autoignition front and tribrachial flame are shown in Fig. 2 as the top and bottom horizontal lines, respectively. The  $S_d/S_L$  for the steady tribrachial flame is around unity, while this value is around eight for the autoignition front. These values are similar to those in HCCI combustion studies [26] and therefore can be used to benchmark the unsteady cases. The periodic time history profile of  $S_d/S_L$  is bounded by but does not fully reach the two steady values,

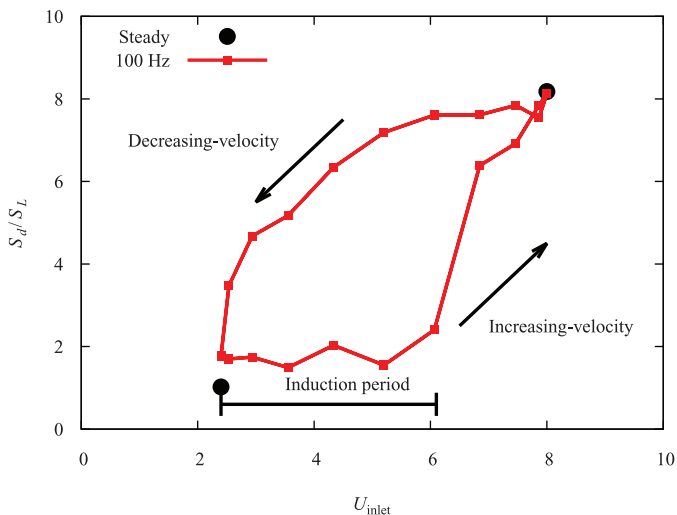


**Fig. 3.** Normalized displacement velocities at various inlet velocities for two steady cases and the 100 Hz oscillating unsteady cases.

indicating that, while the chemical structure responds to the flow dynamics, such response is not fast enough to reach steady-state.

When  $S_d/S_L$  approaches the tribrachial flame limit, its value is almost constant, while the change near the autoignition limit is more sinusoidal. Moreover,  $S_d/S_L$  changes more abruptly when the combustion mode switches from tribrachial flame to autoignition. Compared to the profile of the normalized leading point location ( $x_d/D$ ), which is almost sinusoidal, the profile of the normalized displacement velocity is asymmetric, indicating that the transition from tribrachial flame to autoignition as the inlet velocity increases is not an exact reverse process of the transition from autoignition to tribrachial flame. Indeed, as shown in Fig. 1, although the inlet velocities at 0.25 and 0.75 cycle are the same, the structures demonstrate different morphologies during the cycle of decreasing- and increasing-velocity: there is hysteresis during the transition.

Such hysteresis is demonstrated more clearly in Fig. 3, where  $S_d/S_L$  is plotted against the inlet velocity. Given the same inlet velocity, the reacting fronts have different displacement velocities during the cycle of decreasing- and increasing-velocity. Additional evidence of hysteresis, shown in Fig. 1, is the shift in the location of the leading point in the mixture fraction space:  $Z = 0.14$  when the tribrachial flame dominates and  $Z = 0.24$  when autoignition dominates. The shift in the leading point mixture fraction as well as the displacement velocity indicates different dominant chemical reactions, and analysis of the dominant chemical reactions will reveal the mechanism of the hysteresis.

From the steady case analysis [14], the dominant chemical pathways are found to be different at the leading point of the tribrachial flame and autoignition front. Specifically, the hydrogen peroxide branching reaction ( $H_2O_2 + M \rightleftharpoons OH + OH + M$ ) is the dominant chain branching reaction at the leading point of the autoignition front, while the H radical branching reaction ( $H + O_2 \rightleftharpoons O + OH$ ) is the most important chain branching reaction at the tribrachial flame leading point. Due to the longer residence time, hydrogen peroxide accumulation is much higher upstream of the autoignition front compared to the tribrachial flame front.

As hydrogen peroxide plays different roles in the tribrachial flame and autoignition front, its spatial profiles along the  $Z = 0.14$  and  $Z = 0.24$  iso-contours are compared in Fig. 4, with the left and right subfigures corresponding to the decreasing-velocity and increasing-velocity half cycles, respectively. Qualitatively, the evolution of the hydrogen peroxide profiles shows similar trends along both mixture fraction iso-contours. The left figures show that hy-

drogen peroxide accumulates until either autoignition occurs or it is consumed at the flame front, resulting in a sharp drop in its mass fraction. However, depending on the mixture fraction, the peak value of the hydrogen peroxide mass fraction differs by three to five times between a steady autoignition front (the steady 8.0 m/s case) and a tribrachial flame (the steady 2.4 m/s case), which implies its different significance in these two combustion modes and sets the benchmark for the unsteady evolution. As the inlet velocity decreases from 8.0 m/s, the peak  $Y_{H_2O_2}$  almost remains constant, indicating that the chemical structure is very close to the steady autoignition case. As a consequence, the dominant chemical pathway remains  $H_2O_2 + M \rightleftharpoons OH + OH + M$ , and autoignition is the dominant combustion process, resulting in larger  $S_d/S_L$ . However, as the flow velocity decreases, a larger gradient is achieved, resulting in steeper profiles and smaller  $S_d/S_L$ , according to Eq. (1). The large gradient results in enhanced back diffusion from the reacting front to the unburnt upstream mixture and ultimately drives the transition into a tribrachial flame.

Even when the inlet velocity reaches the minimum 2.4 m/s, which is the same as the steady case, the reacting front continues to move upstream. Inlet velocity changes slowest around the half cycle, allowing the chemical structure to respond to the hydrodynamic changes. As shown on the right of Fig. 4, the peak  $Y_{H_2O_2}$  decreases from 0.5 to 0.65 of the cycle. At this stage, autoignition is not fully activated, since the peak  $Y_{H_2O_2}$  is lower than the steady autoignition case. However, the peak  $Y_{H_2O_2}$  is still larger than the steady tribrachial flame. Therefore, the  $S_d/S_L$  of the tribrachial structure is close to but slightly larger than a steady flame, for it is propagating into a partially reacted mixture.

As the inlet velocity further increases from 0.65 to 0.75 of the cycle, the propagation speed of the tribrachial flame cannot keep up with the flow incoming velocity, and the flame structure is therefore convected downstream. During this flame blow-off process,  $S_d/S_L$  remains essentially constant, which is demonstrated as the flattened bottom in Fig. 3. Meanwhile, the unburnt mixture upstream of the flame accumulates radicals and heat as it moves downstream and eventually triggers autoignition, indicated by a sudden jump of  $S_d/S_L$ . The time difference between the half cycle (where the inlet velocity is 2.4 m/s) and the last sample point before the sudden jump of  $S_d/S_L$  is defined as the induction period, as indicated in Fig. 3.

### 3.3. Effects of oscillation frequency

To better understand the coupling between hydrodynamics and chemistry and the hysteretic behavior in Fig. 3, the effects of oscillation frequency are analyzed. Compared to the 100 Hz case, the other two cases of lower oscillation frequency are similar qualitatively but with some quantitative differences. Figure 5 shows the evolution of the normalized leading point location ( $x_d/D$ ) for the three oscillating cases, compared with the steady benchmark cases. The peak-to-peak variation represents the oscillation amplitude during a cycle. Two distinct trends are evident. First, as the oscillation frequency increases, the oscillation amplitude decreases. Extrapolating, if the oscillation frequency were much faster than any chemical or transport times scale, the oscillation amplitude would be zero, since the thermal structure could not respond to the velocity changes.

Second and more interestingly, for all three frequencies, the most downstream points during the oscillation are almost identical to the steady case at 8.0 m/s. However, as the frequency increases, the most upstream point during the oscillation deviates more from the steady case at 2.4 m/s. The different effects of oscillation frequency on the most downstream and upstream points are attributed to the difference in the combustion mode at these two locations. As demonstrated in Fig. 3, the 100 Hz oscillating

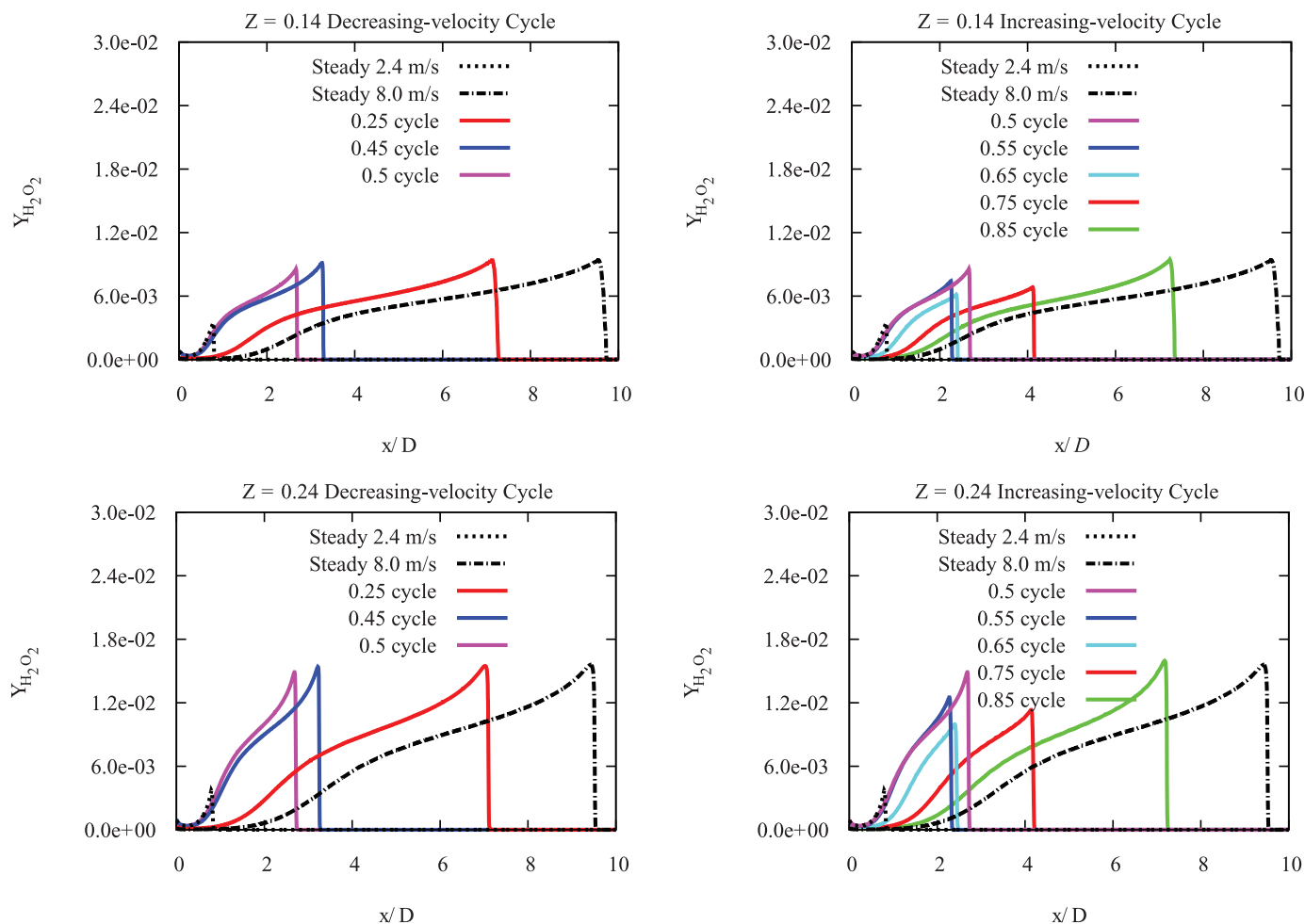


Fig. 4. Comparison of hydrogen peroxide mass fraction profiles along the  $Z = 0.14$  and  $Z = 0.24$  iso-contours at steady state and at 100 Hz during the decreasing-velocity cycle (left) and increasing-velocity cycle (right).

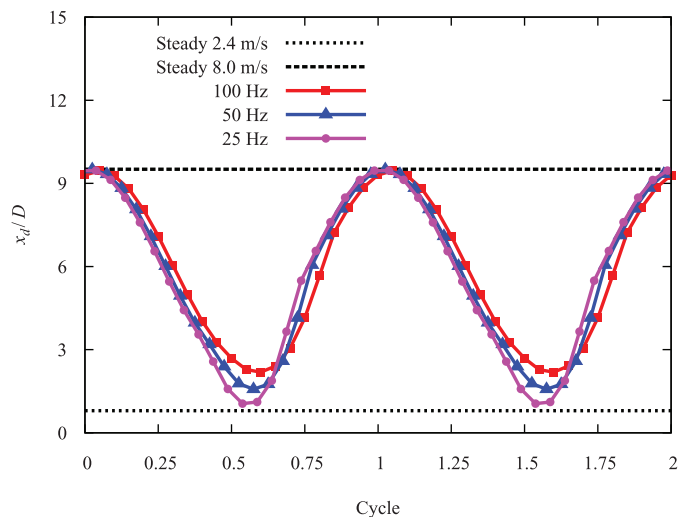
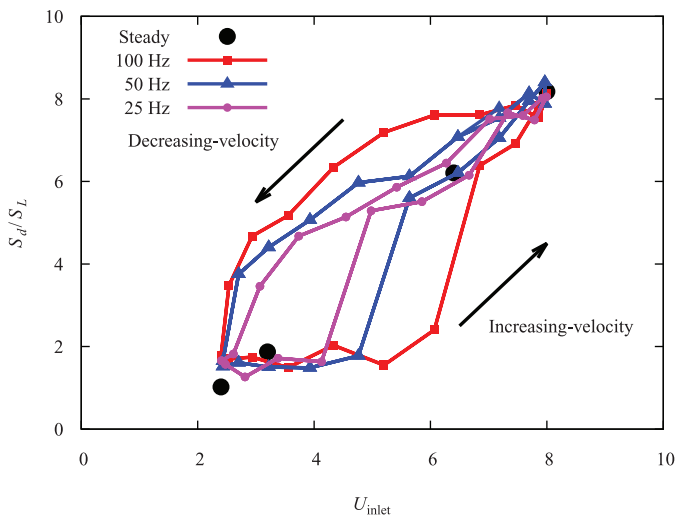


Fig. 5. Normalized leading point location time history profiles at 25, 50, and 100 Hz.

case has already established quasi-steady state when the boundary velocity is at 8.0 m/s when the combustion mode is kinetically controlled by autoignition. In a Lagrangian sense, the location of an autoignition front is directly related to the ignition delay time,

determined by chemical kinetics. Therefore, the location of the autoignition front at this quasi-steady state is almost the same as the steady case with the same boundary velocity, which can be crudely estimated as the product of the ignition delay time and the boundary velocity. For even lower frequency cases, such a quasi-steady state is even easier to achieve. Consequently, for all three oscillation frequencies, the most downstream points remain very close to the steady autoignition governed case with the boundary velocity of 8.0 m/s. Conversely, the stabilization mechanism for the steady case at 2.4 m/s is kinematically controlled by the balance between the tribrachial flame propagation speed and the incoming flow speed. For the 100 Hz case, however, such kinematic balance never achieves quasi-steady state, as discussed in the previous section. The location of the tribrachial flame is then determined kinematically both by the velocity difference between the unsteady tribrachial flame propagation speed and the flow speed and the time allowed for such displacement to occur. At lower oscillation frequencies, longer time is allowed for the tribrachial flame to propagate upstream into the partially reacted mixture, while the displacement velocity decreases gradually due to reduced reactivity upstream. The most upstream point location will then asymptotically approach the steady state case at 2.4 m/s more closely at lower oscillation frequency in Fig. 5.

Besides the oscillation amplitude, the hysteretic behavior is also affected by the oscillation frequency. As shown in Fig. 6, the



**Fig. 6.** Normalized displacement velocities at various inlet velocities for four steady cases and three oscillating unsteady cases at different frequencies. Induction periods for the unsteady cases can also be defined similar to Fig. 3 but are not shown here for clarity.

**Table 1**  
Induction time at different oscillation frequencies.

Frequency [Hz]	25	50	100
Induction time [ms]	6	4	2.5

hysteresis of decreasing and increasing velocity is diminished as the oscillation frequency decreases, denoted by the shrinking of the enclosed area. Hysteresis remains at slower inlet velocities since the decreasing-velocity branch is still autoignition dominated, but it takes finite induction time for the increasing-velocity unburnt mixture to achieve autoignition. At higher inlet velocities, both branches are autoignition dominant and therefore collapse to a single path at sufficiently low frequency, approaching the quasi-steady limit. Ideally, the quasi-steady limit could be achieved by investigating even lower frequencies, such as 0.1 Hz; however, such calculation would be extraordinarily intensive, requiring more than 20 million core-hours. Instead, three steady state cases reported previously [14] and a new steady case at the boundary velocity of 6.4 m/s are also included in Fig. 6 to illustrate the steady state limit. The 3.2 m/s case is kinematically stabilized, similar to the 2.4 m/s case, and therefore is closer to the increasing-velocity branches of the oscillating cases but is different from the decreasing-velocity branches for the same reason at the lower velocity condition, as discussed in the previous section. Conversely, the 6.4 m/s case is kinetically stabilized by autoignition, which can be approached by both the decreasing-velocity and increasing-velocity branches at lower oscillation frequency.

In terms of the relative portion of the oscillation cycle, the 100 Hz case demonstrates a more pronounced hysteresis and longer induction period. However, in term of the absolute time, shown in Table 1, the 25 Hz case takes a longer time to achieve the transition from small  $S_d/S_L$  to larger values during the increasing-velocity portion of the cycle, noting that the time intervals between sampling points in Fig. 6 are not the same for the three frequencies, being 0.5, 1.0, and 2.0 ms for 100, 50, and 25 Hz, respectively.

This counter-intuitive finding is explained with Fig. 7. Here, the temperature, hydrogen peroxide, and methoxymethylperoxy radical ( $\text{CH}_3\text{OCH}_2\text{O}_2$ ) profiles are compared for the three frequency cases for both decreasing- and increasing-velocity branches at the same inlet velocity of 3.2 m/s and benchmarked with the correspond-

ing steady computation. According to previous studies [13,14], this steady case is autoignition dominated and stabilized at  $Z = 0.24$ .

According to the temperature profiles, the steady and unsteady cases all demonstrate two heat release stages, with the first and second stage correlated well with the depletion of the  $\text{CH}_3\text{OCH}_2\text{O}_2$  radical and hydrogen peroxide, respectively. The  $\text{CH}_3\text{OCH}_2\text{O}_2$  radical is often chosen to represent the NTC chemistry [12]. As demonstrated in previous studies [13,14], NTC chemistry is important in the upstream of both tribrachial flame and autoignition front, and NTC chemistry is still important for the unsteady cases. It is seen from Fig. 7 that, irrespective of the oscillation frequency and traveling direction, at the same inlet velocity,  $Y_{\text{CH}_3\text{OCH}_2\text{O}_2}$  matches with its steady state profile, indicating that NTC chemistry responds to the flow oscillation relatively fast, and therefore is decoupled from flow dynamics.

Conversely, the coupling between fluid dynamics and second-stage autoignition/flame chemistry is important, for the hydrogen peroxide profiles of the unsteady cases fail to collapse onto that of the steady case. Although three unsteady profiles on the decreasing-velocity branch show similar peak values, the lower the frequency, the closer the profile matches the steady case, which is expected from Fig. 6. However, the unsteady profiles on the increasing-velocity branch show lower peak values than the steady structure, with the 100 Hz case profile being closer to the steady counterpart. Noting from Fig. 6 that the minimum  $S_d/S_L$  in all three cases are larger than the steady 2.4 m/s case and at lower frequency the unburnt mixture has longer time to relax to steady state, the 25 Hz case should match the 2.4 m/s steady case closer, that is, a tribrachial flame with low  $\text{H}_2\text{O}_2$  accumulation. Therefore, a longer time is required to accumulate this lost  $\text{H}_2\text{O}_2$  and activate autoignition. Conversely, the 100 Hz case allows less time to relax to a steady flame structure and therefore has larger  $Y_{\text{H}_2\text{O}_2}$  to start with during the increasing-velocity cycle, resulting in a shorter induction time for autoignition.

The different effects of oscillation frequency on the first-stage NTC chemistry and second-stage autoignition/flame chemistry can be understood by comparing the characteristic time scales of these processes. The ignition delay time for the first-stage ignition facilitated by NTC chemistry is relatively short ( $\sim 0.3$  ms [14]) compared to the major autoignition process induced by the hydrogen peroxide branching reaction ( $\sim 1$  ms [14]) and the characteristic hydrodynamic oscillation time (10–40 ms in the current work). Therefore, for the low frequency oscillations investigated in the current study, the fluid dynamics and second-stage autoignition/flame chemistry coupling is mainly responsible for the hysteretic behavior and deviation from the steady state.

At even higher oscillation frequencies, the NTC chemistry could interact with the hydrodynamics. Such conditions were attempted computationally, but the elevated frequency resulted in vortex shedding and local flame extinction, which add further complexity.

#### 4. Conclusions

Axisymmetric laminar nonpremixed DME coflow flames at elevated temperatures and pressures with sinusoidally oscillating inlet velocities were computationally investigated. The inlet velocity oscillates between 2.4 and 8.0 m/s at 25, 50, and 100 Hz. Flame dynamics in such oscillating flows and frequency effects on the hydrodynamics-chemistry coupling were analyzed.

The heat release rate profiles were examined to describe the thermal structure. The morphology of the thermal structure transitions between tribrachial and multibrachial. The multibrachial structure is favored when the inlet velocity is higher, although there is hysteresis during the transition. Such structures agree well with the steady cases in Deng et al. [14], which correspond to different combustion modes: tribrachial flame and autoignition.

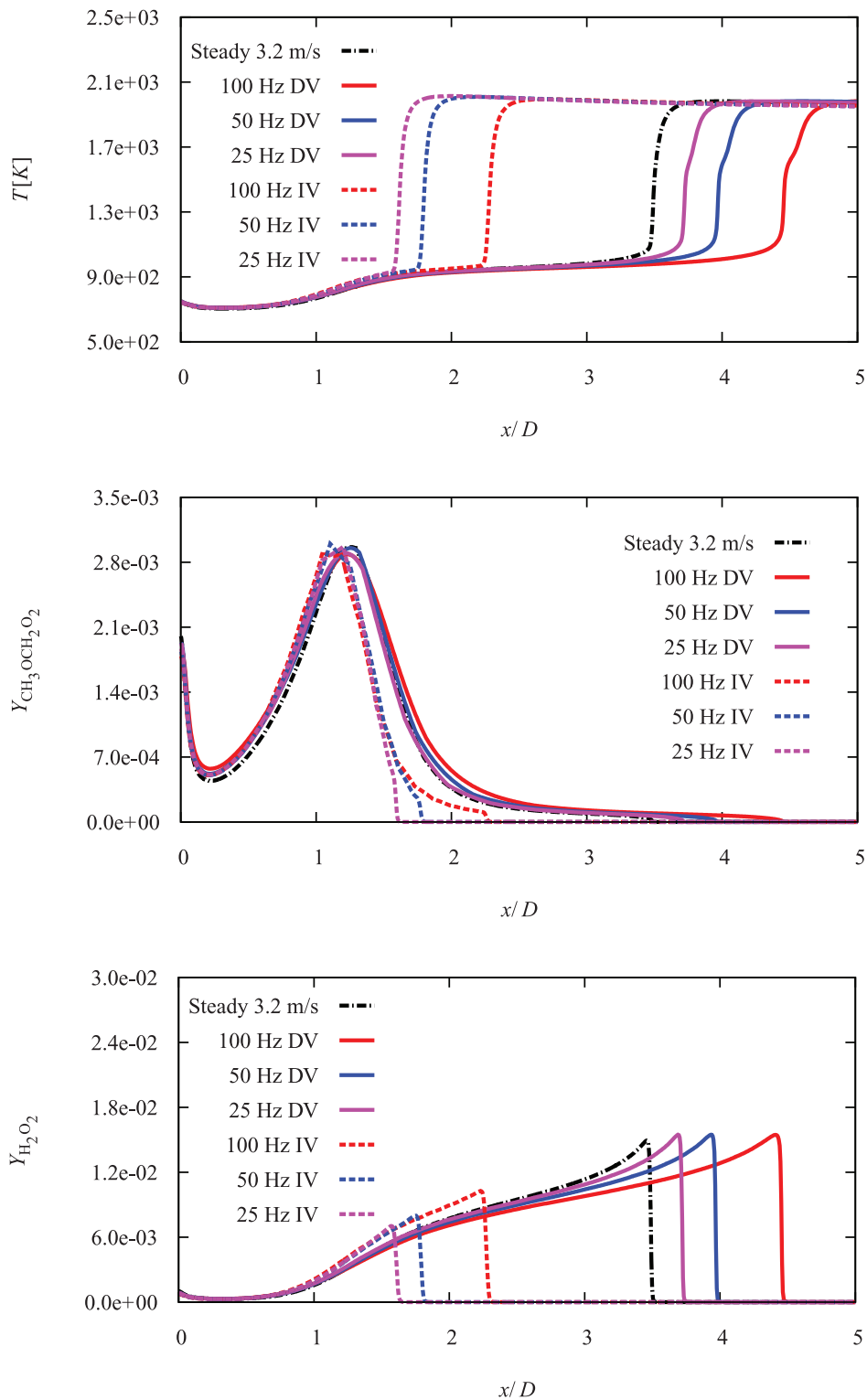


**Fig. 7.** Temperature, methoxy methylperoxy radical, and hydrogen peroxide mass fraction profiles along the  $Z = 0.24$  iso-contour at 3.2 m/s. DV: decreasing-velocity, and IV: increasing-velocity.

Normalized displacement velocity was defined to differentiate these two modes in the current study and compare with the steady cases.

According to the steady results, the normalized displacement velocity for a tribrachial flame is around unity and is larger for autoignition. The same criterion was applied to the unsteady cases to elucidate the evolution of combustion mode. As the inlet velocity

decreases, autoignition is the dominant combustion process until flame chemistry takes over around the most upstream location and slowest inlet velocity. The tribrachial flame is convected downstream as the flow velocity increases. The radical and heat accumulation upstream of the tribrachial flame finally results in autoignition, showing a sudden increase in the normalized displacement velocity.

Oscillation frequency effects on the hydrodynamics–chemistry coupling were analyzed by examining the profiles of temperature, methoxymethylperoxy radical, and hydrogen peroxide during the oscillation process. It is found that, at the three frequencies investigated, the tribrachial structure does not have sufficient time to reach steady state, and the transition from tribrachial flame to a multibrachial autoignition front occurs over a finite induction time as velocity increases. Consequently, the decreasing-velocity and increasing-velocity cycles have different normalized displacement velocities and hence demonstrate hysteresis. At lower frequencies, such hysteresis is less pronounced, for longer relaxation time is allowed to approach the quasi-steady state condition.

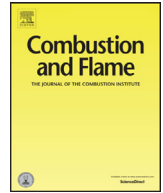
NTC chemistry represented by methoxymethylperoxy radical accumulation and depletion has shorter time scales, and therefore is able to respond to the hydrodynamic changes. However, autoignition and flame establishment have comparable time scales to the oscillation period and are therefore coupled with the flow dynamics. At lower oscillation frequencies, chemical kinetics is closer to reaching the two steady-state conditions with the maximum and minimum boundary velocities.

### Acknowledgments

This research was supported in part by the [Air Force Office of Scientific Research](#) (AFOSR) under the technical management of Dr. Mitat Birkan.

### References

- [1] J. Buckmaster, Edge-flames, *Prog. Energy Combust. Sci.* 28 (5) (2002) 435–475.
- [2] C.M. Müller, H. Breitbach, N. Peters, Partially premixed turbulent flame propagation in jet flames, *Symp. (Int.) Combust.* 25 (1994) 1099–1106.
- [3] S.H. Chung, Stabilization, propagation and instability of tribrachial triple flames, *Proc. Combust. Inst.* 31 (1) (2007) 877–892.
- [4] A.W. Strawa, B.J. Cantwell, Investigation of an excited jet diffusion flame at elevated pressure, *J. Fluid Mech.* 200 (1989) 309–336.
- [5] M. Sánchez-Sanz, B.A.V. Bennett, M.D. Smooke, A. Liñán, Influence of Strouhal number on pulsating methane-air coflow jet diffusion flames, *Combust. Theory Modell.* 14 (2010) 453–478.
- [6] C.R. Shaddix, J.E. Harrington, K.C. Smyth, Quantitative measurements of enhanced soot production in a flickering methane/air diffusion flame, *Combust. Flame* 99 (1994) 723–732.
- [7] R.R. Skaggs, J.H. Miller, Tunable diode laser absorption measurement of carbon monoxide and temperature in a time-varying methane-air non-premixed flame, *Symp. (Int.) Combust.* 26 (1996) 1181–1188.
- [8] R.K. Mohammed, M.A. Tanoff, M.D. Smooke, A.M. Schaffer, M.B. Long, Computational and experimental study of a forced, timevarying, axisymmetric, laminar diffusion flame, *Symp. (Int.) Combust.* 27 (1998) 693–702.
- [9] S.B. Dworkin, B.C. Connelly, A.M. Schaffer, B.V. Bennett, M.B. Long, M.D. Smooke, M.P. Puccio, B. McAndrews, J.H. Miller, Computational and experimental study of a forced, time-dependent, methane-air coflow diffusion flame, *Proc. Combust. Inst.* 31 (2007) 971–978.
- [10] B.C. Choi, S.H. Chung, Autoignited laminar lifted flames of methane, ethylene, ethane, and n-butane jets in coflow air with elevated temperature, *Combust. Flame* 157 (12) (2010) 2348–2356.
- [11] S.M. Al-Noman, S.K. Choi, S.H. Chung, Autoignition characteristics of laminar lifted jet flames of pre-vaporized iso-octane in heated coflow air, *Fuel* 162 (2015) 171–178.
- [12] A. Krisman, E.R. Hawkes, M. Talei, A. Bhagatwala, J.H. Chen, Polybrachial structures in dimethyl ether edge-flames at negative temperature coefficient conditions, *Proc. Combust. Inst.* 35 (2015) 999–1006.
- [13] S. Deng, P. Zhao, M.E. Mueller, C.K. Law, Autoignition-affected stabilization of laminar nonpremixed DME/air coflow flames, *Combust. Flame* 162 (2015) 3437–3445.
- [14] S. Deng, P. Zhao, M.E. Mueller, C.K. Law, Stabilization of laminar nonpremixed DME/air coflow flames at elevated temperatures and pressures, *Combust. Flame* 162 (2015) 4471–4478.
- [15] J.E. Temme, P.M. Allison, J.F. Driscoll, Low frequency combustion instabilities imaged in a gas turbine combustor flame tube, 50th AIAA Aerospace Sciences Meeting (AIAA 2012-0542).
- [16] H. Pitsch, N. Peters, A consistent flamelet formulation for non-premixed combustion considering differential diffusion effects, *Combust. Flame* 114 (1–2) (1998) 26–40.
- [17] S. Deng, P. Zhao, D. Zhu, C.K. Law, NTC-affected ignition and low-temperature flames in nonpremixed DME/air counterflow, *Combust. Flame* 161 (8) (2014) 1993–1997.
- [18] A. Bhagatwala, Z. Luo, H. Shen, J.A. Sutton, T. Lu, J.H. Chen, Numerical and experimental investigation of turbulent DME jet flames, *Proc. Combust. Inst.* 35 (2015) 1157–1166.
- [19] Z. Zhao, M. Chaos, A. Kazakov, F.L. Dryer, Thermal decomposition reaction and a comprehensive kinetic model of dimethyl ether, *Int. J. Chem. Kinet.* 40 (1) (2008) 1–18.
- [20] O. Desjardins, G. Blanquart, G. Balarac, H. Pitsch, High order conservative finite difference scheme for variable density low Mach number turbulent flows, *J. Comput. Phys.* 227 (15) (2008) 7125–7159.
- [21] X. Liu, S. Osher, T. Chan, Weighted essentially non-oscillatory Schemes, *J. Comput. Phys.* 115 (1) (1994) 200–212.
- [22] C.D. Pierce, Progress-variable approach for large-eddy simulation of turbulent combustion. Ph.D. thesis, Stanford University, 2001.
- [23] J.F. MacArt, M.E. Mueller, Semi-implicit iterative methods for low Mach number turbulent reacting flows: operator splitting vs. approximate factorization, *J. Comput. Phys.* (submitted for publication).
- [24] S.D. Cohen, A.C. Hindmarsh, P.F. Dubois, CVODE, a stiff/nonstiff ODE solver in C, *Comput. Phys.* 10 (2) (1996) 138–143.
- [25] H. Pitsch, M. Chen, N. Peters, Unsteady flamelet modeling of turbulent hydrogen-air diffusion flames, *Symp. (Int.) Combust.* 27 (1) (1998) 1057–1064.
- [26] C.S. Yoo, Z. Luo, T. Lu, H. Kim, J.H. Chen, A DNS study of ignition characteristics of a lean iso-octane/air mixture under HCCI and SACI conditions, *Proc. Combust. Inst.* 34 (2013) 2985–2993.
- [27] G.R. Ruetsch, L. Vervisch, A. Liñán, Effects of heat release on triple flames, *Phys. Fluids* 7 (6) (1995) 1447.
- [28] H.G. Im, J.H. Chen, Structure and propagation of triple flames in partially premixed hydrogen-air mixtures, *Combust. Flame* 119 (1999) 436–454.
- [29] H. Pitsch, FlameMaster, A C++ computer program for 0D combustion and 1D laminar flame calculations.



# Coupling of harmonic flow oscillations to combustion instability in premixed segments of triple flames



V'yacheslav Akkerman<sup>a,b,\*</sup>, Chung K. Law<sup>a</sup>

<sup>a</sup> Department of Mechanical and Aerospace Engineering, Princeton University, Princeton, NJ 08544-5263, USA

<sup>b</sup> Department of Mechanical and Aerospace Engineering, West Virginia University, Morgantown, WV 26506-6106, USA

## ARTICLE INFO

### Article history:

Received 2 November 2015

Revised 8 December 2015

Accepted 15 July 2016

### Keywords:

Combustion instability  
Darrieus–Landau instability  
Acoustic stabilization  
Parametric instability  
Triple (tribranchial) flames  
Flame–acoustic coupling

## ABSTRACT

Combustion instability of a lifted triple flame downstream of the injector nozzle in an acoustic field is studied, with implication on the combustion instability in liquid rocket engines. The analysis is focused on the premixed flame segment, and is based on the linear equation for a perturbed flamefront. Assuming that the radius of the flamefront curvature is much larger than that of the internal flame structure, the premixed front is approximated as being quasi-planar. Both acoustical stabilization of the hydrodynamic flame instability and excitation of the parametric instability by sound waves are considered, and the limitation for stable/unstable regimes as a function of flame parameters and acoustic frequency/intensity is determined. The velocity-wise nature of the sound is scrutinized, namely, the acoustics are imitated by a pocket of harmonic flow oscillations. First, the Landau limit of infinitely thin flames is employed. Then the formulation is extended to account for the finite flame thickness, and it is demonstrated how unstable regimes are modified by the flame thickness.

© 2016 The Combustion Institute. Published by Elsevier Inc. All rights reserved.

## 1. Introduction

Combustion instabilities in liquid rocket engines (LRE) are driven by various fundamental processes including mixing, flame dynamics, chemical kinetics and spray formation [1]. Besides, the dynamics of nozzle injection as well as the subsequent fuel-oxidizer mixing and combustion can also contribute to the instability onset. In particular, a resonance can develop through acoustic coupling between the chamber dynamics and the injection and combustion processes [2]. It is generally believed that combustion within LREs likely proceeds in the diffusion-flame mode and, due to the high density of the medium, the associated reactions occur infinitely fast as compared to the processes of heat and mass transport. Consequently, the majority of studies on the LRE combustion instabilities are focused on diffusion flame processes in the limit of flame-sheet combustion.

Generally speaking, four possible flame stabilization mechanisms have been proposed for the bulk diffusion flame, resulting from the separately injected fuel and oxidizer, namely, (i) that through the presence and extinction of diffusion flamelets generated by mixing [3]; (ii) stabilization by the recirculation zone

around the injection nozzle [4,5]; (iii) that through auto-ignition in a turbulent flow field, occurring when one of the reactants is introduced at a high temperature [6]; and, eventually, (iv) stabilization of the bulk flame through a triple flame structure at the base of the flame [7], which constitutes the focus of the present paper.

To be more specific with the latter, 4th stabilization mechanism, of Chung [7], we consider a flamefront propagating through a fuel/air mixing layer, where the fuel concentration is stratified from lean to rich. The resulting flame exhibits a tribrachial (triple) structure, consisting of a lean and a rich premixed flame wings together with a trailing diffusion flame, all extending from a single point [8]. The propagation speed and dynamics of these flame segments are dominantly influenced by the fuel concentration gradient, or the mixture fraction gradient upstream of the intersection point, since the local laminar burning velocities along the premixed flame wings depend sensitively on the fuel concentration, and the concentration gradient determines the effective thickness of a flammable region and, thereby, the curvature of the premixed wings [7]. When the flow rate from the nozzle is small, the flame is attached to the rim of the nozzle. In contrast, when the flow rate is sufficiently large, the flame can be lifted off as shown schematically in Fig. 1.

Stabilization and the structure of triple flames were addressed in Refs. [9] and [10], which were followed by the classical papers [8,11], see also Refs. [1] and [12] for details. In particular, the

\* Corresponding author at: Department of Mechanical and Aerospace Engineering, West Virginia University, Morgantown, WV 26506-6106, USA.

E-mail address: [Vyacheslav.Akkerman@mail.wvu.edu](mailto:Vyacheslav.Akkerman@mail.wvu.edu) (V. Akkerman).

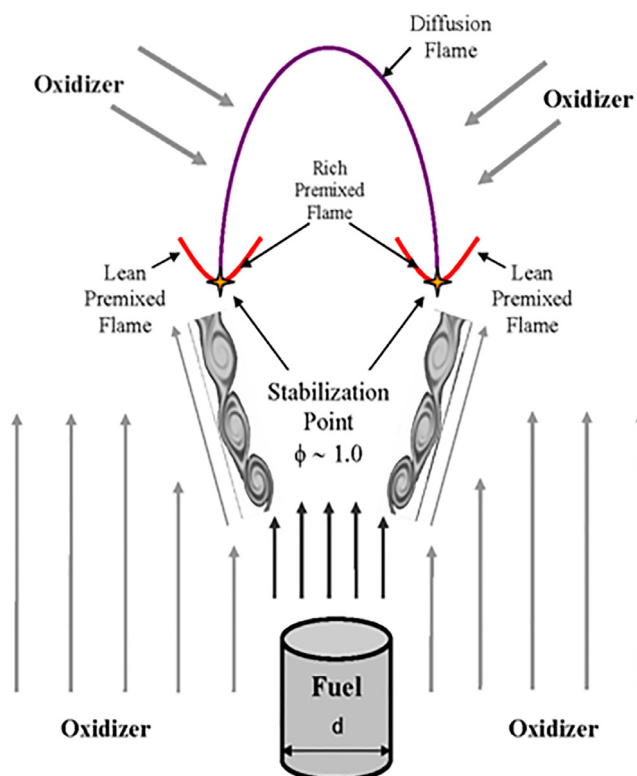


Fig. 1. Structure of a nozzle-generated and stabilized triple flame.

stabilization criterion have been determined in Ref. [11] recognizing that the point of stabilization for a triple flame is a locus where the lean-premixed, rich-premixed and diffusive flame segments meet, and where the fuel/oxidizer equivalence ratio is close to stoichiometric. Based on the fact that the local flame speed should balance the flow velocity, Ref. [11] calculated the stoichiometric laminar flame speed  $\tilde{S}_L$  as a function of the flame parameters such as the Schmidt number  $Sc$  and the fuel mass fraction  $Y$ , as well as the flow parameters, such as the nozzle diameter  $d$ , the inlet flow mean velocity  $u_0$ , and the flow velocity profile.

The formulation [11] has been extended in a series of studies. In particular, the substantial influence of the thermal expansion and mixture fraction on the triple flame speed has been found [13], and the stretch effect [14] as well as the heat release [15] were incorporated into the investigation. However, an analysis of the stability of the triple flame through that of the leading, premixed flame segment, when subjected to imposed oscillations like external or flame-generated acoustics, has not been performed. In this regard, we note that analyses of the hydrodynamic instability of premixed flames were performed in Refs. [16–19] and subsequently extended to flame–sound interactions in Refs. [20–23]. It was shown that high-frequency acoustics may either stabilize or amplify the hydrodynamic instability, depending on various flame and sound parameters. Furthermore, a flame accelerated normal to itself, such as due to flow oscillations normal to itself, may be subjected to the parametric instability. In addition, it is noted that a flame–acoustic resonance may lead to violent folding of a premixed flamefront [23,24] and, presumably, even flame turbulization [25,26].

In this regard, in the present work we investigate the effect of harmonic flow oscillations, such as might be induced by acoustic waves, on the stability of tribrachial lifted flames. For this purpose, the structure of a tribrachial flame [8,11], the dispersion relation for the intrinsic flame instability [17–19], and the flame–acoustic interactions [2,20–23] are combined. It is noted, in this respect, that complementary to a tangential component to the flamefront,

such as it would in the premixed flame segments, the flow may also involve wrinkles propagating along the flame surface.

The analysis is presented in the following four sections. The generalized formulation on the coupling of an imposed harmonic flow oscillation to an intrinsic instability mode is presented in Section 2. The local flame speed is described in Section 3. The development of the hydrodynamic instability in the presence of sound waves, either external or flame-generated, as well as the acoustically-excited parametric instability, are analyzed in Section 4 within the Landau limit of zero flame thickness. The effect of finite flame thickness is considered in Section 5. The paper ends with concluding remarks.

## 2. Generalized formulation

We consider a discontinuity surface of zero or finite thickness separating two fluids of different properties. The surface is corrugated by weak, linear, two-dimensional perturbations described by the function  $z = F(x, t) = \sum f_i(t) \cos(k_i x)$ . Hydrodynamic equations ahead and behind the front, the matching conditions across the front, and the reaction evolution equation can be incorporated into a linear dispersion relation for the perturbation amplitude  $f$  in a general form  $\hat{I}f = 0$ , where the instability operator  $\hat{I}$  describes the surface response to the perturbation, and it couples the instability growth rate  $\sigma$  to the perturbation wavenumber  $k$ ,  $\hat{I} = \hat{I}(\sigma, k)$ , which can also include a multitude of other hydrodynamic and thermal-chemical parameters inherent to the associated instability mode. If the system is subjected to an external oscillating field, such as that of acoustics, the dispersion relation reads  $\hat{I}f = \hat{\Phi}_a f$ . It is assumed that the forcing operator  $\hat{\Phi}_a$  is characterized mainly by a dominant acoustic mode of frequency  $\Omega$  and amplitude  $U_a$ ,  $\hat{\Phi}_a = (\Omega, U_a)$ , which are determined by the combustion chamber dynamics for implications to the amplitude and frequency of the LRE combustion instability.

Within linear approximation, there are two interacting frequency modes between the intrinsic instability and the acoustic oscillations, namely, (i) a resonant mode,  $\Omega = \omega$ , which modifies and weakens the intrinsic instability, and (ii) a doubling mode,  $\Omega = 2\omega$ , which can excite the parametric instability through the intrinsic-acoustic coupling if the sound is strong enough. For the resonant mode, we seek the solution to the dispersion relation  $\hat{I}f = \hat{\Phi}_a f$  in the form  $f = f_1(t) + f_2(t) \cos(\Omega t)$ , with  $f_1$  and  $f_2$  being “slow functions” that vary considerably during a time interval much larger than the oscillation period,  $2\pi/\Omega$ . For the parametric mode, a partial solution to the dispersion relation acquires the form  $f = \{f_3 \cos(\Omega t/2) + f_4 \sin(\Omega t/2)\} \exp(\sigma t)$ . In both branches we then arrive at the stability criterion given by  $\text{Re}\{\sigma\} < 0$ .

This formulation will be systematically employed to quantify the coupling between various intrinsic flamefront instability modes and the chamber acoustics. The instability modes of interest include, though not limited to: (i) the Rayleigh–Taylor (RT; body-force) instability for both premixed and diffusion flame segments; (ii) the Kelvin–Helmholtz (KH; shear-layer) instability which can be mostly important for diffusion flames because of the inherently different properties of the fuel and oxidizer jets; (iii) the diffusional-thermal (DT; nonequidiffusive) instability, which not only is pervasive for premixed flames, with its intensity diminishing with increasing pressure as the flame thickness reduces, but is also relevant for near-limit diffusion flames; and (iv) the Darrieus–Landau (DL; hydrodynamic) instability, inherent to all practical premixed flames. Furthermore, unlike the DT mode, the DL instability intensifies with increasing pressure and thereby is especially relevant to LRE premixed flame segments. All these instability modes and their relevance to the diffusive and premixed flame segments are summarized in Table 1. This approach has recently been employed to the KH instability in a non-reacting

**Table 1**  
Intrinsic and acoustic flamefront instability modes.

Instability mode	Premixed flame	Diffusion flame
Rayleigh–Taylor (RT)	Yes	Yes
Kelvin–Helmholtz (KH)	?	Yes
Diffusional-thermal (DT)	Pervasive, ↓ as p ↑	Near-limit situations
Darrius–Landau (DL)	↑ as p ↑ and L ↓	No
//////////	//////////	//////////
Acoustical/parametric	Yes	Yes

share-flow [27]. In the rest of this paper, we shall focus on the 4th, DL instability and its coupling to a resonant harmonic flow oscillation imitating an imposed or flame-generated sound wave.

### 3. Local flame speed at premixed flame segments

In this section, we briefly recall Chung’s theory of bulk flame stabilization through a triple flame structure at the base of the flame ensemble [7]. Upon mixing between the fuel and oxidizer downstream of a nozzle, a concentration gradient is established from the fuel side to the oxidizer side, leading to the formation of a premixed flame segment that varies from fuel-lean to fuel-rich over its surface. Downstream of this premixed flame segment, the unburned oxidizer from the fuel-lean segment further reacts with the unburned fuel from the fuel-rich segment, forming a diffusion flame, which eventually merges with the bulk diffusion flame. The flame structure therefore consists of a lean-premixed flame (LPF) segment, a rich-premixed flame (RPF) segment, and a downstream diffusion flame (DF) segment, as shown in Fig. 1. It is believed that stabilization of this structure is achieved through that of the concentration-stratified premixed flame base, at the stoichiometric location on its surface. It is emphasized that the flame dynamics near the attachment point has an essential influence on the overall flame dynamics for both premixed and diffusion flames. Specifically, these dynamics essentially appear as “boundary conditions” for the rest of the premixed or diffusion flamelet dynamics; see, for instance Refs. [28] and [29] as well as references therein.

According to Ref. [8], the triple flame is described by the similarity variable

$$\eta = \sqrt{\frac{3}{32}} Re \frac{r}{z}, \quad (1)$$

where the Reynolds number  $Re \equiv u_0 d / \nu$  is related to the inflow, and the coordinate  $\eta = \eta_S$  along the stoichiometric contour  $Y = Y_S$  may be expressed as

$$1 + \frac{\eta_S^2}{8} = \left[ \frac{2Sc + 1}{8\pi \nu z_S} \frac{I}{\rho Y_S} \right]^{1/2Sc} = \left[ \frac{2Sc + 1}{32 Y_S} \frac{Red}{z_S} \right]^{1/2Sc}, \quad (2)$$

with the mass flux of the fuel being  $I = \pi \rho u_0 d^2 / 4$ . As a result, we find

$$r_S = \frac{16 z_S}{\sqrt{3} Re} \sqrt{\left( \frac{2Sc + 1}{32 Y_S} \frac{Red}{z_S} \right)^{1/2Sc} - 1}. \quad (3)$$

If the first term under the square root in Eq. (3) is much greater than unity, then the shape of the stoichiometric contour  $Y = Y_S$  is described by the explicit self-similar formula

$$\frac{z_S}{d Re} = \left( \frac{32 Y_S}{2Sc + 1} \right)^{\frac{1}{4Sc-1}} \left( \frac{\sqrt{3}}{16} r_S \right)^{\frac{4Sc}{4Sc-1}}. \quad (4)$$

The z-velocity component of the flow and the fuel mass fraction along the similarity variable are then given by

$$u = \frac{3}{8\pi \nu z_S} \frac{J}{\rho} \frac{1}{(1 + \eta_S^2/8)^2} = \frac{3}{32} u_0 \frac{Red}{z_S} \frac{1}{(1 + \eta_S^2/8)^2}, \quad (5)$$

$$Y_S = \frac{2Sc + 1}{8\pi \nu z_S} \frac{I}{\rho} \frac{1}{(1 + \eta_S^2/8)^{2Sc}} = \frac{2Sc + 1}{32} \frac{Red}{z_S} \frac{1}{(1 + \eta_S^2/8)^{2Sc}}, \quad (6)$$

with the momentum flux  $J = u_0 I = \pi \rho u_0^2 d^2 / 4$ , and the lift-off height of the flame given by [8]

$$H_L = \frac{3}{24} \left( \frac{4Y_S}{2Sc + 1} \right)^{\frac{1}{Sc-1}} \left( \frac{u_0}{\tilde{S}_L} \right)^{\frac{2Sc-1}{Sc-1}} \frac{d^2 \tilde{S}_L}{\nu}. \quad (7)$$

Consequently, we have  $H_L \propto d^2 u_0^{(2Sc-1)/(Sc-1)}$ , where the proportionality factor is determined from the fuel characteristics. The lift-off height is proportional to the nozzle cross section, and the Schmidt number,  $Sc$ , is the key parameter for the stability of triple/lifted flames, in that a stabilized lifted flame can exist only for  $Sc < 0.5$  or  $Sc > 1$ . Eliminating  $\eta_S$  by combining Eqs. (5) and (6), and recognizing that the stoichiometric local flame speed is balanced by the axial flow velocity at the stabilization point,  $\tilde{S}_L = u(Y_S)$ , we obtain

$$\frac{\tilde{S}_L}{u_0} = 3 \left( \frac{Y_S}{2Sc + 1} \right)^{1/Sc} \left( \frac{Red}{32 z_S} \right)^{\frac{Sc-1}{Sc}}. \quad (8)$$

Together with Eq. (4), Eq. (8) yields

$$\tilde{S}_L = 3 u_0 \left( \frac{Y_S}{2Sc + 1} \right)^{\frac{3}{4Sc-1}} \left( 2\sqrt{3} \frac{r_S}{d} \right)^{\frac{4-4Sc}{4Sc-1}}. \quad (9)$$

Eq. (9) shows  $\tilde{S}_L$  as a function of the radial coordinate  $r_S$ . This is a given mixture parameter, which determines the flame stabilization condition. It is emphasized that unlike the standard one-dimensional unstretched laminar flame speed, which is a thermochemical parameter, the local quantity  $\tilde{S}_L$  is a result of both the flame and the flow. It depends on the fuel properties by means of  $Sc$  and  $Y_S$ , and on the flow parameters via  $d$  and  $u_0$ . Another parameter characterizing the fuel type is the density expansion factor  $\Theta = \rho_u / \rho_b$ . The latter plays the key role in the present work, as will be shown subsequently. Obviously, varying the fuel type we would change  $\tilde{S}_L$  and  $\Theta$ , and thereby modify the results.

It is also recognized that the analysis above, based on the Chung theory [7,8] does not consider transition to turbulence, thereby providing the limitation on the Reynolds number that can be employed. It is noted, in this respect, that according to the classical Hottel–Hawthorne work [30], when the jet velocity is low and the flow is laminar, the flame height increases with the jet velocity but only until a certain maximum at which the instability is observed at the flame tip. In contrast, with a further increase in the jet velocity, the flame becomes turbulent, and its height sharply decreases and, when scaled by the nozzle diameter, remains almost constant thereafter [1,30]. Such a turbulent flame is beyond the present work and will be considered elsewhere.

### 4. Coupling of harmonic flow oscillations to premixed flames

Eq. (3) describes a “quasi-steady” flame shape in the form  $z_S = F_0(r_S)$ . However, the steady formulation of Section 3 does not account for hydrodynamic flame instability as well as external and/or flame-generated acoustics and vortices, which, in turn, can lead to additional destabilization of the flame. Accounting for the fact that the radius of the curvature of the LPF/RPF sheet is much larger than the internal flame structure, we consider the entire premixed front as quasi-planar; and the local mass fraction of the fuel mixture  $Y$ , the local density expansion factor  $\Theta = \rho_u / \rho_b$ , and the local planar flame speed  $\tilde{S}_L$  are assumed to be constant. For simplicity, we first illustrate our formulation in the Landau limit of zero flame thickness, and then extend it to that of finite flame thickness.

We consider weak perturbations of any planar segment in the form  $\tilde{z} = F_0(r) + \tilde{F}(r, t)$ , with  $F_0(r)$  given by Eq. (4), and  $|\tilde{F}| \ll F_0$ . It

is nevertheless recognized that neglecting the radius of the curvature of the leading edge of the flamefront could potentially miss some physical effects such as the triple flame may actually appear at a point in the flow, where the velocity is noticeably larger than that evaluated as the laminar flame speed [29]. Furthermore, the oscillatory flow disturbances may cause an oscillation in curvature of the leading edge of the flame and, thereby, an oscillatory modification of the approach flow velocity. However, a detailed quantification of these effects requires a separate analysis and will be presented elsewhere. For simplicity, hereafter we deal with a two-dimensional configuration, though the formulation can be extended to a three-dimensional flow. In the Landau limit of zero flame thickness, the basic equations in a two-dimensional incompressible flow ( $u, w$ ) are the continuity equation

$$\frac{\partial u}{\partial z} + \frac{\partial w}{\partial r} = 0, \quad (10)$$

the Navier–Stokes equations

$$\frac{\partial u}{\partial t} + u \frac{\partial u}{\partial z} + w \frac{\partial u}{\partial r} = -\frac{1}{\rho} \frac{\partial P}{\partial z} + \nu \nabla^2 u + g_z, \quad (11)$$

$$\frac{\partial w}{\partial t} + u \frac{\partial w}{\partial z} + w \frac{\partial w}{\partial r} = -\frac{1}{\rho} \frac{\partial P}{\partial r} + \nu \nabla^2 w + g_r, \quad (12)$$

the matching conditions

$$u_+ - u_- - (w_+ - w_-) \frac{\partial \tilde{F}}{\partial r} = \tilde{S}_L (\Theta - 1) \sqrt{1 + \left( \frac{\partial \tilde{F}}{\partial r} \right)^2}, \quad (13)$$

$$w_+ - w_- + (u_+ - u_-) \frac{\partial \tilde{F}}{\partial r} = 0, \quad (14)$$

$$P_+ - P_- = -(\Theta - 1) \rho_u \tilde{S}_L^2, \quad (15)$$

and the flame evolution equation

$$\frac{\partial \tilde{F}}{\partial t} + w_- \frac{\partial \tilde{F}}{\partial r} - u_- + \tilde{S}_L \sqrt{1 + \left( \frac{\partial \tilde{F}}{\partial r} \right)^2}. \quad (16)$$

Eqs. (10)–(16) can be incorporated into the linear dispersion relation for the perturbation amplitude  $\tilde{F} = f(t) \exp(ikr)$  in the form [17–20]

$$\frac{\partial^2 f}{\partial t^2} + \frac{2\Theta}{\Theta + 1} \tilde{S}_L k \frac{\partial f}{\partial t} - A \Theta \tilde{S}_L^2 k^2 f = Ak \tilde{g} f \cos \alpha, \quad (17)$$

where  $A = (\Theta - 1)/(\Theta + 1)$  is the local Atwood number,  $\tilde{g}$  the general acceleration field, and  $\alpha$  the angle between the acceleration vector and the normal vector to the flame sheet. Eq. (17) describes the linear stage of the Darrieus–Landau and Rayleigh–Taylor instability modes in the acceleration field. Without external acceleration,  $\tilde{g} = 0$ , Eq. (17) reduces to the Darrieus–Landau dispersion relation [16]. In the present study, the acceleration field is that of acoustics. The sound wave is characterized by a dominant mode  $\tilde{u}_z = U \sin(\omega t)$ , with the amplitude  $U$  and frequency  $\omega$ . Then Eq. (17) becomes

$$\frac{\partial^2 f}{\partial t^2} + \frac{2\Theta}{\Theta + 1} \tilde{S}_L k \frac{\partial f}{\partial t} - A \Theta \tilde{S}_L^2 k^2 f = AkU\omega \cos(\omega t) f \cos \alpha. \quad (18)$$

We consider two situations, namely: (a) that of external acoustics, when  $U$  and  $\omega$  are free parameters of the problem, and (b) of flame-generated acoustics, when  $U$  and  $\omega$  depend on the flame/flow parameters.

It is noted that there are two modes of the flame–acoustic interaction: (i) the resonant mode,  $\Omega = \omega$ , describing the development of the Darrieus–Landau (DL) instability in the presence of acoustics, and thereby possible flame stabilization by sound; and (ii) the mode which frequency is twice that of the oscillating field,  $\Omega = 2\omega$ , that can excite the parametric instability of a corrugated flame segment.

#### 4.1. Stabilization of flame instability by a resonant harmonic oscillation

Recognizing that the stabilization of the intrinsic flamefront instabilities by sound waves is analogous to the stabilization of the Kapitsa pendulum [16], following the method of Bychkov [21], we seek the solution to Eq. (18) in the form

$$f = f_1(t) + f_2(t) \cos(\omega t), \quad (19)$$

where  $f_1$  and  $f_2$  are “slow functions” which do not change considerably during the acoustic time  $2\pi/\omega$ . Then  $d^2 f_2/dt^2 \propto \omega^2 f_2 \gg \tilde{S}_L k (df_2/dt) \gg \tilde{S}_L^2 k^2 f_2$ , and substituting Eq. (19) into Eq. (18), we find

$$\begin{aligned} \frac{\partial^2 f_1}{\partial t^2} - \omega^2 f_2 \cos(\omega t) + \frac{2\Theta}{\Theta - 1} \tilde{S}_L k \frac{df_1}{dt} \\ - A \Theta \tilde{S}_L^2 k^2 f_1 - A \omega U k f_1 \cos \alpha \cos(\omega t) \\ - A \omega U k f_2 \cos \alpha \frac{1 + \cos(2\omega t)}{2} = 0. \end{aligned} \quad (20)$$

Separating the terms of Eq. (20) oscillating with frequency  $\omega$ , we obtain

$$f_2 = -A U k f_1 \cos \alpha / \omega, \quad (21)$$

$$\frac{\partial^2 f_1}{\partial t^2} + \frac{2\Theta}{\Theta + 1} \tilde{S}_L k \frac{df_1}{dt} + \left( \frac{1}{2} A^2 U^2 \cos^2 \alpha - A \Theta \tilde{S}_L^2 \right) k^2 f_1 = 0. \quad (22)$$

Seeking the solution to Eq. (22) in the form  $f_1 \propto \exp(\sigma_1 t)$ , we obtain the dispersion relation

$$\sigma_1 = \frac{\Theta}{\Theta + 1} \left[ -1 + \sqrt{\frac{\Theta^2 + \Theta - 1}{\Theta} - \frac{1}{2} \left( \frac{(\Theta - 1) U \cos \alpha}{\tilde{S}_L} \right)^2} \right] \tilde{S}_L k. \quad (23)$$

Eq. (23) formally does not include the acoustic frequency  $\omega$  because it was derived with the assumption of high-frequency oscillations as compared to the characteristic DL growth rate. It is seen from Eq. (23) that the increase in the acoustic amplitude reduces the instability growth rate  $\sigma_1$ . The instability is completely suppressed by the sound waves if  $\text{Re}\{\sigma_1\} < 0$ , i.e. when

$$\left( \frac{U \cos \alpha}{\tilde{S}_L} \right)^2 > 2\Theta \frac{\Theta + 1}{\Theta - 1} = \frac{2\Theta}{A}, \quad (24)$$

or

$$U \cos \alpha > 3 \left( 2\Theta \frac{\Theta + 1}{\Theta - 1} \right)^{1/2} \left( \frac{Y_S}{2Sc + 1} \right)^{\frac{3}{4Sc - 1}} \left( 2\sqrt{3} \frac{r}{d} \right)^{\frac{4 - 4Sc}{4Sc - 1}} u_0, \quad (25)$$

accounting for the relation (9). Here we have considered the sound waves as an external force of the problem. In the event of flame-generated sound, we take  $\alpha \sim 0$ , and the local acoustic amplitude can be estimated by means of the local corrugated flame speed as

$$U \sim (\Theta - 1) \tilde{S}_L \sqrt{1 + (dF_0/dr)^2}. \quad (26)$$

With Eqs. (4) and (26), the inequality (24) becomes

$$\left( \frac{4Sc}{4Sc - 1} \text{Re} \right)^2 \left[ \frac{32 Y_S}{2Sc + 1} \left( \frac{\sqrt{3}}{16} \right)^4 \frac{r}{d} \right]^{\frac{2}{4Sc - 1}} > \frac{2\Theta(\Theta + 1)}{(\Theta - 1)^3} - 1. \quad (27)$$

The result (27) shows the criterion governing the suppression of the onset of the hydrodynamic instability at the premixed segment of a lifted triple flame by flame-generated acoustics. According to Eq. (27), the suppression occurs for arbitrary  $\text{Re}$ ,  $Sc$  and  $Y_S$  if  $\Theta > \Theta_c \approx 4.84$ , as the RHS of Eq. (27) is negative in this case.

#### 4.2. Parametric instability

Another effect of flame–acoustic interaction is the development of the parametric instability of a premixed flame segment, which is excited by the mode of twice the smaller frequency than that of sound. The parametric instability of a premixed flamefront in an oscillating field resembles the classical parametric instability of an oscillator [16,20]. Following Bychkov [21], we look for a partial solution to Eq. (18) in the form

$$f = \left[ f_3 \cos\left(\frac{\omega t}{2}\right) + f_4 \sin\left(\frac{\omega t}{2}\right) \right] \exp(\sigma_2 t), \quad (28)$$

where the coefficients  $f_3$  and  $f_4$  are the free parameters, and  $\sigma_2$  the growth rate of the parametric instability. Substituting Eq. (28) into Eq. (18), collecting the terms containing  $\cos(\omega t/2)$  and  $\sin(\omega t/2)$ , and omitting terms of higher frequencies, we find

$$f_3 \left( \sigma_2^2 + \frac{2\Theta}{\Theta+1} \tilde{\zeta}_L k \sigma_2 - A \Theta \tilde{\zeta}_L^2 k^2 - \frac{\omega^2}{4} - \frac{A}{2} U \omega k \right) + f_4 \left( \sigma_2 \omega + \frac{\Theta}{\Theta+1} \tilde{\zeta}_L k \omega \right) = 0, \quad (29)$$

$$f_4 \left( \sigma_2^2 + \frac{2\Theta}{\Theta+1} \tilde{\zeta}_L k \sigma_2 - A \Theta \tilde{\zeta}_L^2 k^2 - \frac{\omega^2}{4} + \frac{A}{2} U \omega k \right) + f_3 \left( \sigma_2 \omega + \frac{\Theta}{\Theta+1} \tilde{\zeta}_L k \omega \right) = 0, \quad (30)$$

and subsequently arrive at the dispersion relation for the parametric instability

$$\left( \sigma_2^2 + \frac{2\Theta}{\Theta+1} \tilde{\zeta}_L k \sigma_2 - A \Theta \tilde{\zeta}_L^2 k^2 - \frac{\omega^2}{4} \right)^2 + \left( \sigma_2 \omega + \frac{\Theta}{\Theta+1} \tilde{\zeta}_L k \omega \right)^2 = \left( \frac{A U \omega k}{2} \right)^2. \quad (31)$$

The parametric instability is excited if  $\text{Re}\{\sigma\} > 0$ , i.e. when

$$\left( \frac{U \cos \alpha}{\tilde{\zeta}_L} \right)^2 - \left( \frac{2\Theta}{\Theta-1} \right)^2 > \left( \frac{\omega^2 + 4A\Theta \tilde{\zeta}_L^2 k^2}{2A\tilde{\zeta}_L \omega k} \right)^2. \quad (32)$$

In the event of flame-generated sound, the acoustic amplitude can be estimated by Eqs. (4) and (26), while its frequency can be estimated by means of the speed of sound  $c_s$  and the combustor width  $L_{comb}$  or the lift-off height  $H_L$ , Eq. (7),

$$\omega \sim 2\pi c_s / L_{comb}, \quad \text{or} \quad \omega \sim 2\pi c_s / H_L, \quad (33)$$

respectively, depending on whether radial or axial sound waves are considered. Consequently, Eqs. (4), (7), (26), (32) and (33) constitute the criterion for the parametric instability excitation by flame-induced acoustics.

Obviously, the premixed flame segment can be stable if the result (32) exceeds the result (24) for any  $k$ ,  $\omega$  and  $r$ . Figure 2 shows Eq. (24), dashed, and Eq. (32), solid, with  $\Theta = 1.2$  and  $\Theta = 8$  in Figs. 2(a) and (b), respectively. We note that the solid line, Eq. (32), achieves its minimal value when the oscillation frequency is in resonance with the DL parameter of frequency dimension

$$\omega_0 = 2(A\Theta)^{1/2} \tilde{\zeta}_L k, \quad (34)$$

which is related to the characteristic time of development of the DL instability excited by a perturbation of the wavenumber  $k$ . A “stability band” observed for small thermal expansion in Fig. 2a designates absolute stability against perturbations of any wave

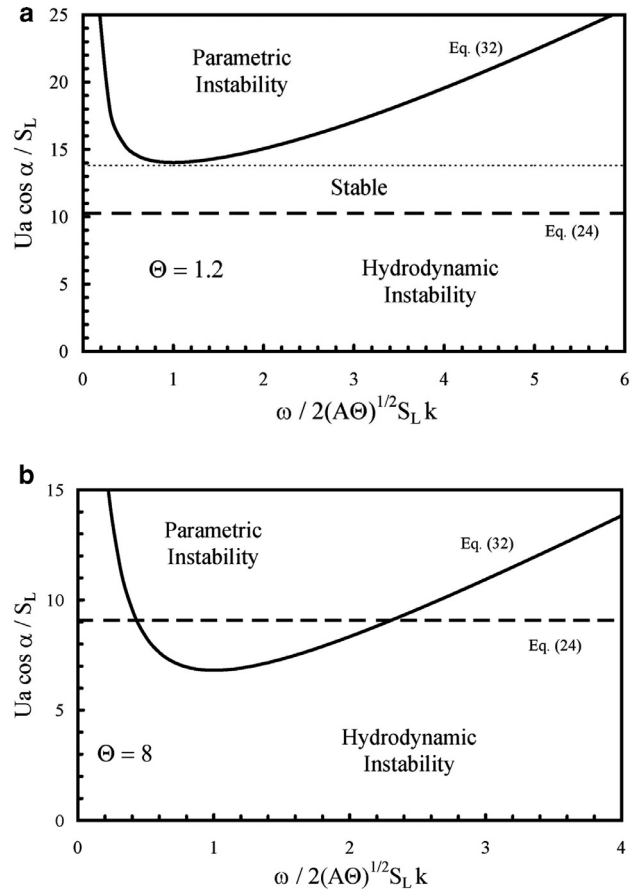


Fig. 2. Stability diagrams for flames with small,  $\Theta = 1.2$  (a), and large,  $\Theta = 8$  (b), thermal expansion in the Landau limit of zero flame thickness,  $L = 0$ .

numbers. According to Eqs. (24) and (32), there is no “absolute stability band” if  $\Theta > \frac{1}{2}(1 + \sqrt{5}) \approx 1.6$ , as demonstrated in Fig. 2b. It is noted, in this respect, that this threshold thermal expansion associated with the absolute stability is much smaller than the typical values in most flames. Therefore the absolute stability of Fig. 2 is rarely expected to occur in practical combustors. However, the “conditional stability” with respect to a limited range of perturbations (limited wavelengths/wavenumbers) is devoted to higher thermal expansions, including those occurring in the practical reality, say  $\Theta = 5 \sim 8$ .

#### 5. Effect of finite flame thickness

Analysis of flame–acoustic interaction developed in Section 3 is limited to the Landau limit of zero flame thickness,  $L = 0$ . It is noted, however, that accounting for the internal flame structure leads to qualitatively and quantitatively new effects. First of all, the finite flame thickness can stabilize the DL effects at sufficiently small scales [17,18]. Second, for non-unity Lewis number  $Le$ , the diffusional-thermal instability becomes effective, leading to cellular or pulsating behavior of  $Le < 1$  or  $Le > 1$  premixtures, respectively [1]. Finally, stretch effects are activated for  $Le \neq 1$  flames of finite thickness. A positive/negative stretch suppresses/promotes the cellular instability, while promoting/suppressing the pulsating instability [1].

Within the approach of small, but finite flame thickness,  $0 < kL \ll 1$ , Ref. [17] extended the Darrieus–Landau dispersion relation to  $\sigma = \sigma_0(1 - k/k_c)$ , where  $\sigma_0$  is the DL growth rate in the Landau limit, determined by Eq. (23) without acoustics,  $U = 0$ , and  $k_c$  the

DL cut off wavenumber given by

$$k_c L = \left[ h_b + \frac{3\Theta - 1}{\Theta - 1} Mk - \frac{2\Theta}{\Theta - 1} \int_1^\Theta \frac{h(\vartheta)}{\vartheta} d\vartheta + (2Pr - 1) \left( h_b - \frac{\int_1^\Theta h(\vartheta) d\vartheta}{\Theta - 1} \right) \right]^{-1}, \quad (35)$$

where the function  $h(\vartheta)$  describes the temperature dependence of the transport coefficients, with  $h(1) = 1$ ,  $h(\Theta) = h_b$ ,  $Pr$  the Prandtl number, and  $Mk$  the Markstein number. The latter describes the flame response to curvature and stretch, and it is related to the Zel'dovich and Lewis numbers,  $Ze$  and  $Le$ , as [17–19]

$$Mk = \frac{\Theta}{\Theta - 1} \int_1^\Theta \frac{h(\vartheta)}{\vartheta} d\vartheta - \frac{Ze(Le - 1)}{2(\Theta - 1)} \int_1^\Theta \frac{h(\vartheta)}{\vartheta} \ln\left(\frac{\vartheta - 1}{\Theta - 1}\right) d\vartheta. \quad (36)$$

It is noted that the characteristic size of the burning zone can vary with the locus,  $L = L(r)$ , because  $\Theta$ ,  $Y$  and  $\tilde{S}_L$  do. Nevertheless, similar to all these flame parameters, we assume  $L$  to be constant within any separate quasi-planar flame segment.

As a result, we readily identify a preliminary stability criterion, which also specifies the limits of the present formulation. This criterion simply states that any small quasi-planar premixed segment of constant flame parameters should nevertheless exceed the DL cut-off wavelength  $\lambda_c = 2\pi/k_c$ . Mathematically, such an estimate takes the form

$$\frac{1}{\Theta} \frac{d\Theta}{dr} < k_c, \quad \frac{1}{Y} \frac{dY}{dr} < k_c, \quad \frac{1}{\tilde{S}_L} \frac{d\tilde{S}_L}{dr} < k_c, \quad \frac{Ze}{L_{mix}} < k_c, \quad (37)$$

where  $L_{mix}$  is a characteristic size of the fuel-oxidizer mixing layer ahead of the nozzle. Of course, the result (37) is an estimate, while for a rigorous stabilization criterion we have to reproduce the analysis of Section 3 accounting for the flame thickness.

Within the approach of  $0 < kL \ll 1$ , extension of Eq. (18) takes the form

$$C_1 d^2 f/dt^2 + C_2 \tilde{S}_L k (df/dt) - C_3 \tilde{S}_L^2 k^2 f = C_4 k U \omega \cos(\omega t) f, \quad (38)$$

where

$$C_1 = 1 + AkL \left( Mk - \Theta \int_0^1 \frac{h(\vartheta) d\vartheta}{1 + (\Theta - 1)\vartheta} \right),$$

$$C_2 = \frac{2\Theta}{\Theta + 1} \left[ 1 + \Theta kL \left( Mk - \int_0^1 \frac{h(\vartheta) d\vartheta}{1 + (\Theta - 1)\vartheta} \right) \right], \quad (39)$$

$$C_3 = A\Theta(1 - k/k_c), \quad C_4 = A + 1 - C_1. \quad (40)$$

Following Section 3, we derive the counterparts of inequalities (24) and (32),

$$\left( \frac{U \cos \alpha}{\tilde{S}_L} \right)^2 > 2 \frac{C_1 C_3}{C_4^2}, \quad (41)$$

$$\left( \frac{U \cos \alpha}{\tilde{S}_L} \right)^2 - \left( \frac{C_2}{C_4} \right)^2 > \left( \frac{C_1 \omega^2 + 4C_3 \tilde{S}_L^2 k^2}{2C_4 \tilde{S}_L \omega k} \right)^2. \quad (42)$$

The results (41) and (42) are shown in Fig. 3 for  $kL = 0.1$  as compared to the Landau limit,  $L = 0$ , shown in Fig. 2b, with  $\Theta = 8$  in both events. It is seen in Fig. 3 that, unlike the Landau limit, accounting for the finite flame thickness predicts steady LPF and RPH sheets for certain conditions.

Figure 4 presents the scaled acoustic amplitude  $U \cos \alpha / \tilde{S}_L$  versus the scaled wavenumber  $kL$  for an equidiffusive premixture,  $Le =$

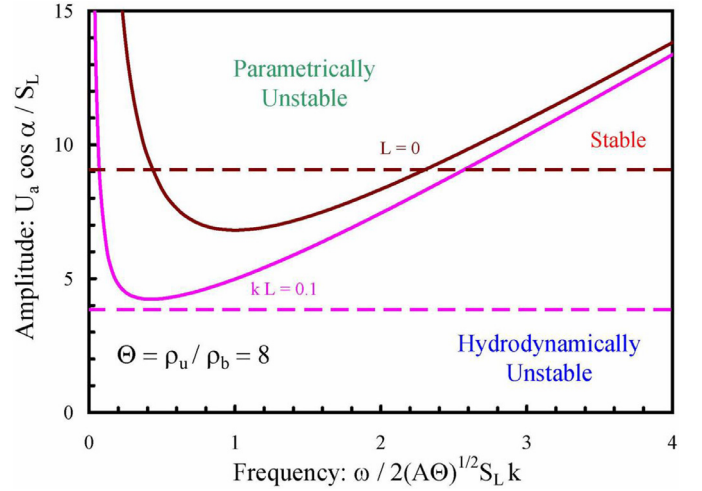


Fig. 3. Stability diagrams for zero,  $L = 0$ , and non-zero,  $kL = 0.1$ , flame thickness.

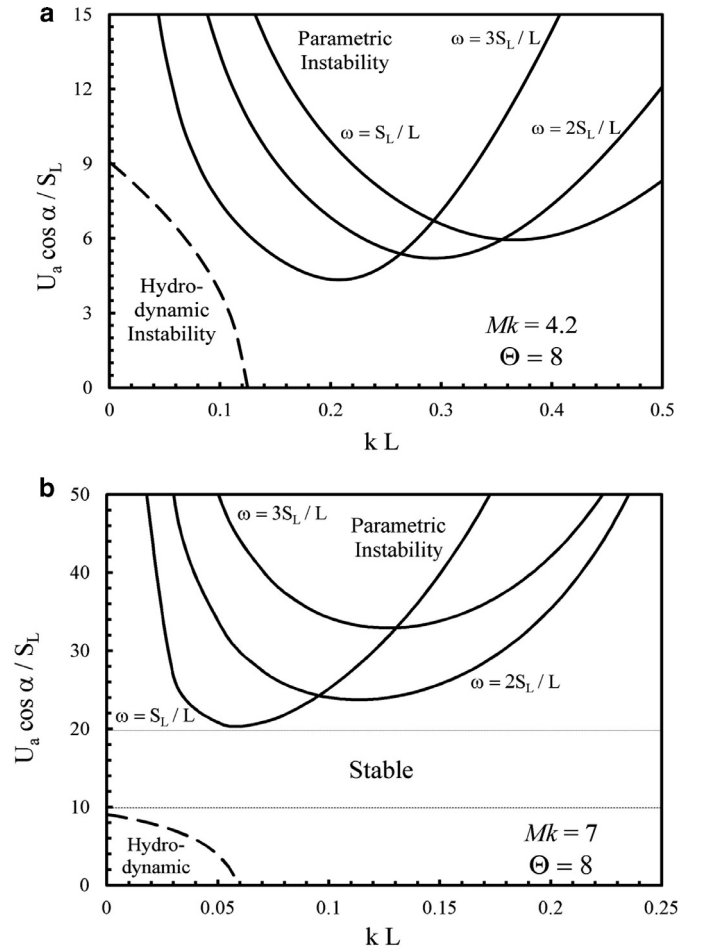


Fig. 4. Stability diagrams for a flame of finite thickness with thermal expansion  $\Theta = 8$  and various diffusivities:  $Le = 1$ ,  $Mk = 4.2$  (a), and  $Le \neq 1$ ,  $Mk = 7$  (b).

1, with  $Mk = 4.2$  (Fig. 4a), and a non-equidiffusive premixture,  $Le \neq 1$ , with  $Mk = 7$  (Fig. 4b), with the expansion factor  $\Theta = 8$  and several fixed scaled frequencies  $\omega L / \tilde{S}_L = 1; 2; 3$  in both plots. Again, we observe a “stability band” for a non-equidiffusive flame in Fig. 4b, but there is no such a band in Fig. 4a. Consequently, it is seen that the increase in the flame thickness and the Markstein number modifies the effect of the combustion instability.

Based on Figs. 3 and 4(a, b), we therefore conclude that a finite flame thickness moderates the combustion instability, due to the thermal stabilization of the DL instability mode. Furthermore, diffusional-thermal effects within a non-equidiffusive burning zone can also stabilize the flame.

## 6. Concluding remarks

In summary, we anticipate the following scenario of flame stabilization/destabilization of a triple flame. First, hydrodynamic instability increases the total burning rate, hence generating sound waves, which in turn can suppress the instability. Second, the sound wave can trigger parametric instability. Therefore, in order to retain a lifted flame stable we have to keep the flame, setup and acoustical characteristics at any point of the front within the stability range shown in Figs. 2–4.

Finally, it is noted that there are two “natures” of acoustics and flame–acoustic coupling: the pressure-wise and the velocity-wise ones. The pressure-wise nature is associated with the acoustic energy, with the stability determined by the classical Rayleigh criterion. The acoustic energy and Rayleigh criterion are beyond the primary interest of this paper. However, it may oftentimes happen that while the Rayleigh criterion predicts the stability, it does not occur in the practical reality because of the instability related to the velocity-wise nature of the flame–acoustic coupling. It is this situation that constitutes the focus of the present work.

## Acknowledgments

This work was supported by the Air Force Office of Scientific Research (AFOSR) under the technical monitoring of Dr. Mitat Birkan.

## References

- [1] C.K. Law, *Combustion physics*, Cambridge University Press, New York, NY, 2006.
- [2] S. Ducruix, T. Schuller, D. Durox, S. Candel, Combustion dynamics and instabilities: Elementary coupling and driving mechanisms, *J. Propulsion & Power* 19 (2003) 722–734.
- [3] N. Peters, F.A. Williams, Liftoff characteristics of turbulent jet diffusion flames, *AIAA J.* 21 (1983) 423–429.
- [4] J.E. Broadwell, M.G. Mungal, Large-scale structures and molecular mixing, *Phys. Fluids A* 3 (1991) 1193–1206.
- [5] F.E. Marble, T.C. Adamson, Ignition and combustion in a laminar mixing zone, *Jet Propuls.* 24 (1954) 85–94.
- [6] T.F. Lu, C.S. Yoo, J.H. Chen, C.K. Law, Three-dimensional direct numerical simulation of a turbulent lifted hydrogen jet flame in heated coflow: a chemical explosive mode analysis, *J. Fluid Mech.* 652 (2010) 45–64.
- [7] S.H. Chung, Stabilization, propagation and instability of tribrachial triple flames, *Proc. Combust. Inst.* 31 (2007) 877–892.
- [8] B.J. Lee, S.H. Chung, Stabilization of lifted tribrachial flames in a laminar non-premixed jet, *Combust. Flame* 109 (1997) 163–172.
- [9] T. Cebeci, P. Bradshaw, *Physical and computational aspects of convective heat transfer*, Springer-Verlag, New York, NY, 1984.
- [10] K.K. Kuo, *Principles of combustion*, Wiley, New York, NY, 1986.
- [11] S.H. Chung, B.J. Lee, On the characteristics of laminar lifted flames in a non-premixed jet, *Combust. Flame* 86 (1991) 62–72.
- [12] J. Buckmaster, Edge-flames, *Prog. Energy Combust. Sci.* 28 (2002) 435–475.
- [13] G.R. Ruetsch, L. Vervisch, A. Linan, Effects of heat release on triple flames, *Phys. Fluids* 7 (1995) 1447–1454.
- [14] J. Daou, A. Linan, Triple flames in mixing layers with nonunity Lewis numbers, *Symp. (Int.) Combust.* 27 (1998) 667–674.
- [15] S. Ghosal, L. Vervisch, Stability diagram for lift-off and blowout of a round jet-laminar diffusion flame, *Combust. Flame* 123 (2001) 646–655.
- [16] L.D. Landau, E.M. Lifshitz, *Fluid mechanics*, Pergamon Press, Oxford, UK, 1989.
- [17] P. Pelce, P. Clavin, Influence of hydrodynamics and diffusion upon the stability limits of laminar premixed flames, *J. Fluid Mech.* 124 (1982) 219–237.
- [18] M. Matalon, B.J. Matkowsky, Flames as gasdynamic discontinuities, *J. Fluid Mech.* 124 (1982) 239–259.
- [19] P. Clavin, P. Garcia, The influence of the temperature dependence of diffusivities on the dynamics of flame fronts, *J. Mec. Theor. Appl.* 2 (1983) 245–263.
- [20] G. Searby, D. Rochwerger, A parametric acoustic instability in premixed flames, *J. Fluid Mech.* 231 (1991) 529–543.
- [21] V. Bychkov, Analytical scalings for flame interaction with sound waves, *Phys. Fluids* 11 (1999) 3168–3173.
- [22] X. Wu, M. Wang, P. Moin, N. Peters, Combustion instability due to the nonlinear interaction between sound and flame, *J. Fluid Mech.* 497 (2003) 23–53.
- [23] X. Wu, C.K. Law, Flame-acoustic resonance initiated by vortical disturbances, *J. Fluid Mech.* 634 (2009) 321–357.
- [24] G. Searby, Acoustic instability in premixed flames, *Combust. Sci. Technol.* 81 (1992) 221–231.
- [25] A. Petchenko, V. Bychkov, V. Akkerman, L.-E. Eriksson, Violent folding of a flame front in a flame-acoustic resonance, *Phys. Rev. Lett.* 97 (2006) 164501.
- [26] A. Petchenko, V. Bychkov, V. Akkerman, L.-E. Eriksson, Flame-sound interaction in tubes with nonslip walls, *Combust. Flame* 149 (2007) 418–434.
- [27] S. Bilgili, O. Ugarte, V. Akkerman, Kelvin-Helmholtz instability interaction with sound waves in reacting viscous potential flows, 9th U.S. National Combustion Meeting, Cincinnati, OH, USA, May 17–20 (2015), Paper # 2E10.
- [28] K. Balasubramanian, R. Sujith, Nonlinear response of diffusion flames to uniform velocity disturbances, *Combust. Sci. Technol.* 180 (2008) 418–436.
- [29] N. Magina, D.H. Shin, V. Acharya, T. Lieuwen, Response of non-premixed flames to bulk flow perturbations, *Proc. Combust. Inst.* 34 (2013) 963–971.
- [30] H.C. Hottel, W.R. Hawthorne, Diffusion in laminar flame jet, *Symp. (Int.) Combust.* 3 (1948) 254–266.



# Initiation and propagation of laminar premixed cool flames



Peng Zhao<sup>1</sup>, Wenkai Liang, Sili Deng, Chung K. Law\*

Department of Mechanical and Aerospace Engineering, Princeton University, Princeton, NJ 08544, USA

## ARTICLE INFO

### Article history:

Received 6 September 2015  
Received in revised form 5 November 2015  
Accepted 8 November 2015  
Available online 14 November 2015

### Keywords:

Low-temperature chemistry  
NTC  
Premixed cool flame  
DME  
Residence time  
Chemiluminescence

## ABSTRACT

Cool flames, being essential features of chemical kinetics of large hydrocarbon fuels, are closely related to the negative temperature coefficient (NTC) phenomenon and engine knock. In this work, the coupling of cool flame chemistry and convective–diffusive transport is computationally and experimentally investigated. A 1-D planar premixed cool flame induced by a hot pocket is first simulated for DME/O<sub>2</sub>/N<sub>2</sub> mixtures with detailed chemistry and transport, demonstrating the existence of a residence time window for quasi-steady propagation. Then with residence time limited by aerodynamic straining, a steady-state premixed cool flame is simulated in a counterflow of heated N<sub>2</sub> against a DME/O<sub>2</sub>/N<sub>2</sub> mixture. It is found that with a high strain rate, corresponding to short residence time, low-temperature heat release is suppressed, resulting in a stretched low-temperature S-curve system response; and that with a sufficiently low strain rate, corresponding to long residence time, ignition induced by low-temperature chemistry would transition to a high-temperature, intensely burning flame. Consequently, a steady-state premixed cool flame exists only for residence time in a strain rate window. A symmetric counterflow configuration is then simulated to determine the cool flame temperature and flame speed at a fixed local strain rate, showing very different controlling chemistry and characteristics as compared to the normal laminar flames governed by high-temperature chemistry. In a companion experimental investigation, premixed cool flames in the counterflow were observed with a high-sensitivity CCD camera in the UV spectrum, with/without a bandpass filter corresponding to the characteristic wavelength of excited HCHO. The chemiluminescence from the cool flame is found to become more intense with increasing equivalence ratio, even for rich mixtures, while the position of the cool flame is insensitive to variation in the equivalence ratio at the same strain rate. These observations qualitatively agree with the numerical simulations, demonstrating the essential features of premixed cool flames.

© 2015 Elsevier Ltd. All rights reserved.

## 1. Introduction

Cool flames, discovered in 1817 [1], have been studied extensively [2]. Its controlling kinetics of the low-temperature chemistry [3] has been shown to be closely related to the phenomena of two-stage ignition and the negative temperature coefficient (NTC) [4], associated with the autoignition [5] and engine knock of large hydrocarbon fuels [6]. They are normally characterized by faint bluish luminescence from excited formaldehyde [7], relatively small heat release and very low CO<sub>2</sub> production. Furthermore, contrary to the normal hot flames in which chemical reactions and transport are strongly coupled, cool flames have been mostly observed in homogeneous systems such as heated closed reaction

vessels [8] and jet-stirred reactors [9], exhibiting oscillatory volumetric heat release and chemiluminescence.

Noting that gas-phase nonuniformities invariably exist in practical systems, recently there has been considerable interest in understanding the coupled effects of cool flame chemistry and transport, leading to the postulation and identification of this class of laminar flames whose flame temperature can be substantially lower than the adiabatic flame temperature corresponding to the (near-)complete consumption of the controlling reactant(s). In particular, Law and Zhao [10] and Zhao and Law [11] demonstrated computationally that with low strain rates and/or high pressures, low-temperature chemistry can strongly couple with transport to induce a secondary S-curve on the lower branch of the conventional (primary) S-curve, with its own distinct ignition and extinction states. Subsequently, using infrared detection Deng et al. [12] experimentally observed a diffusion cool flame in the nonpremixed counterflow at atmospheric pressure. Furthermore, diffusion cool flames have been suggested to explain some experimental results on microgravity droplet combustion [13,14], and have also been

\* Corresponding author.

E-mail address: [cklaw@princeton.edu](mailto:cklaw@princeton.edu) (C.K. Law).

<sup>1</sup> Present address: Department of Mechanical Engineering, Oakland University, Rochester, MI 48309, USA.

directly observed in experiments on plasma-assisted combustion [15].

Recognizing that recent investigations [10–15] on the coupled behavior of low-temperature chemistry and convective–diffusive transport have been mainly on *diffusion* flames, it behooves us to explore if steady, *premixed* cool flames can also be initiated and established, and if so, what are the associated flame structure and propagation rates, including the role of the two-stage ignition delay in establishing such flames. The relevant issue here is that while a diffusion flame is primarily controlled by the counter-diffusion of the fuel and oxidizer reactants, with chemistry playing a secondary role in the global flame characteristics, the structure and propagation of premixed flames inherently depend on the coupled influence of chemical kinetics and transport [16]. Consequently an assessment of the essential role of low-temperature chemistry on flames must necessarily involve studies on premixed flames. In fact, because of the very weak exothermicity of the low-temperature chemistry, and the inevitable heat loss in a flame system, it is not evident *a priori* that a flame embodying this chemistry can be readily initiated and support steady propagation. It is also noted that while premixed cool flames have been studied previously, for example as early as the 1960s [17,18], the increased understanding of flame structures since then is expected to yield further insight and interpretation of this important phenomenon.

The present study consists of three tasks. We first extend, in the next section, the classical NTC phenomenon describing the transient *ignition* of a *homogeneous* mixture to one in which ignition is accomplished by a localized heat source in the 1-D planar domain, which is inherently *nonhomogeneous* in nature and is affected by both chemistry and diffusive transport. Consequently the interest here is the dynamics and chemistry of the ignition process leading to low-temperature flame propagation and its subsequent transition to the high-temperature flame. We shall also show that the transient ignition event depends sensitively on the temperature of the ignition source when low-temperature chemistry is involved.

In order to capture and stabilize the low-temperature flame identified in Section 2, in Section 3 we computationally explore the possible existence of a premixed flame of low-temperature chemistry in the counterflow, with its characteristic residence time controlled by the strain rate of the flow. We shall show that such a flame is predicted to exist, with its chemical structure including the states of ignition and extinction depending sensitively on the strain rate of the flow. Our third task, presented in Section 4, provides the first experimental observation that such stretch-stabilized premixed cool flames indeed exist, thereby brings more insights on the existence and characteristics of laminar cool flames, both nonpremixed [10–15] and premixed [17–20].

The fuel selected for the study is dimethyl ether (DME), which is one of the smallest fuel molecules exhibiting the NTC behavior. The reaction mechanism adopted in the computation is a validated reduced model [21] consisting of both low- and high-temperature kinetics; the associated validation and applications are reported in [12,22].

## 2. Initiation and propagation of the 1-D planar cool flame

We first examine the adiabatic and isobaric autoignition delays of homogeneous stoichiometric DME/O<sub>2</sub>/N<sub>2</sub> mixtures, in order to select the proper conditions to study the ignition and propagation of 1-D planar flames. Fig. 1(a) shows the calculated first-stage, second-stage, and total ignition delay times for initial temperature  $T$ , denoted as  $\tau_1$ ,  $\tau_2$  and  $\tau$  respectively. It is seen that  $\tau$  varies non-monotonically with increasing  $T$ , and hence demonstrates the NTC behavior. Consequently, for an appropriate total ignition delay

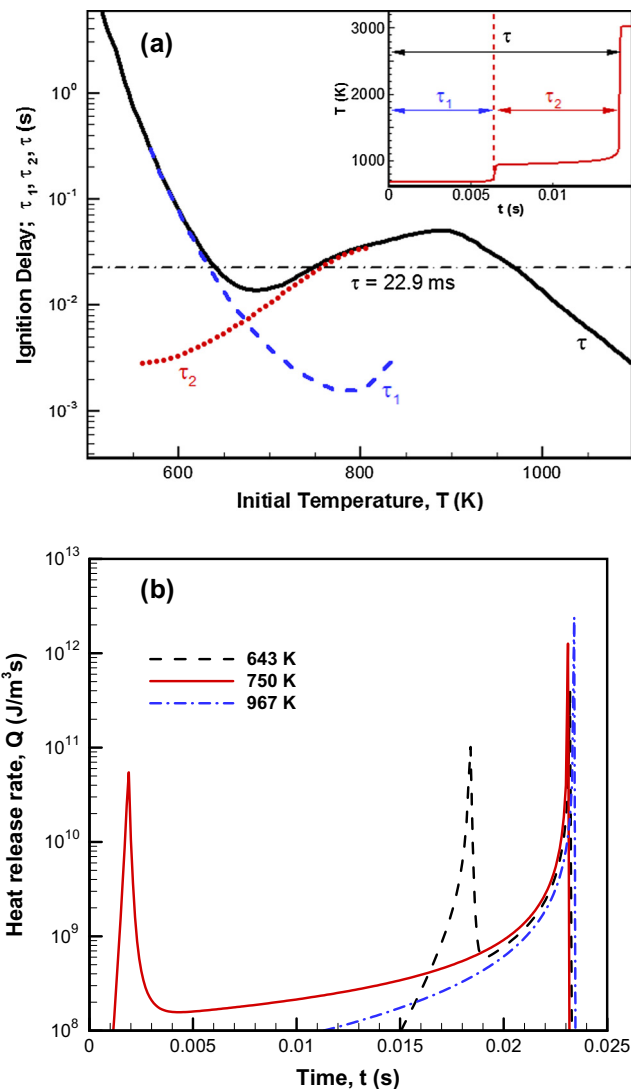


Fig. 1. (a) First-stage, second-stage, and total ignition delays of DME/O<sub>2</sub>/N<sub>2</sub> mixture with 15.8% N<sub>2</sub> in volume, under 1 atm. The inset shows the definitions of various ignition delays in a two-stage ignition process. (b) Heat release rate history for ignition processes at 643 K, 750 K and 967 K.

time, say  $\tau = 22.9$  ms, there are three distinct ignition situations: at the low temperature state of  $T = 643$  K,  $\tau_1$  is much longer than  $\tau_2$ ; at the intermediate temperature state of  $T = 750$  K,  $\tau_2$  is much longer than  $\tau_1$ ; and finally at the high temperature state of  $T = 967$  K, the two-stage ignition behavior disappears and combustion is totally taken over by the intermediate-to-high temperature chemistry, exhibiting a single-stage ignition event. These three distinct ignition situations are further characterized by their correspondingly distinct heat release rates,  $Q$ , as shown in Fig. 1(b). Specifically, for the low and intermediate temperatures of 643 K and 750 K, heat release occurs in two bursts, corresponding to the first and second stage ignition. Furthermore, the first ignition delay for the 750 K case occurs more readily than that of the 643 K case, as expected. For the high-temperature case of 967 K, there is no first-stage ignition and as such ignition occurs in a single burst, through the second ignition delay chemistry. It is also clear that  $Q$  is much lower both before and after the respective ignition bursts.

Based on these observations, we explore how NTC would affect the initiation and propagation of a 1-D planar flame induced by an ignition kernel with these three different temperatures. The

problem studied is as follows. At the initial state, a quiescent, homogeneous, stoichiometric DME/O<sub>2</sub>/N<sub>2</sub> mixture with 15.8% N<sub>2</sub> in volume, and at 300 K and 1 atm, fills a 5 cm computational domain. Then, a hot pocket of initial temperature 643 K, 750 K or 967 K, identified above, is respectively imposed from 0 to 1 cm in the domain to initialize flame propagation. Due to the heat deposition, the kernel gas not only tends to auto-ignite, it also conducts heat into the unreacted mixture causing it to ignite. It is therefore expected that if the thermal diffusion time scale is longer than the first-stage autoignition delay time  $\tau_1$  of the gas in the ignition kernel, low-temperature chemistry will be rapid enough to heat up the kernel gas to the cool flame temperature. The time evolutions starting from the initial condition will be shown in the following, under the ideal, adiabatic condition.

All simulations were carried out using the Adaptive Simulation of Unsteady Reacting Flows (A-SURF) code [23,24], which has been successfully used in various investigations of unsteady flame initiation and propagation [23–26]. It simulates the 1-D compressible multicomponent reacting flow in the planar coordinate using the finite volume method. Details of the governing equations, numerical method and code validation are given in [23,24]. A multi-level adaptive mesh with a minimum mesh size of 10  $\mu\text{m}$  is used to capture the flame structure and propagation. Zero-gradient boundary condition is imposed at the left boundary ( $x = 0$ ) and transmissive condition at the right boundary ( $x = 5$  cm). To avoid discontinuity and the associated numerical difficulties, we used the hyperbolic tangent function, *tanh*, to denote the step function in the initial temperature profile. In order to show evolution of the reaction front and the detailed thermal structure, the *T* and *Q* profiles at the representative state for each case are plotted in Figs. 2–4. For clarity in discussion, we designate the high-temperature reaction front with its temperature around the adiabatic flame temperature as the hot flame front (HFF), and a low-temperature reaction front with its temperature below or around 1000 K as the cool flame front (CFF); the reaction fronts are indicated by dashed arrows.

Fig. 2 shows evolution of the temperature and heat release rate profiles for the low-temperature case of  $T = 643$  K. It is seen that first-stage autoignition is initiated around the center region of the kernel (curve 2), which drives up the center *T* to around 900 K, with the corresponding *Q* occurring in the bulk of the kernel region. Shortly thereafter, the *Q* in the kernel region decreases as the first-stage reactions are completed (left curve 3), while at the same time a low-temperature reaction front with a distinct peak

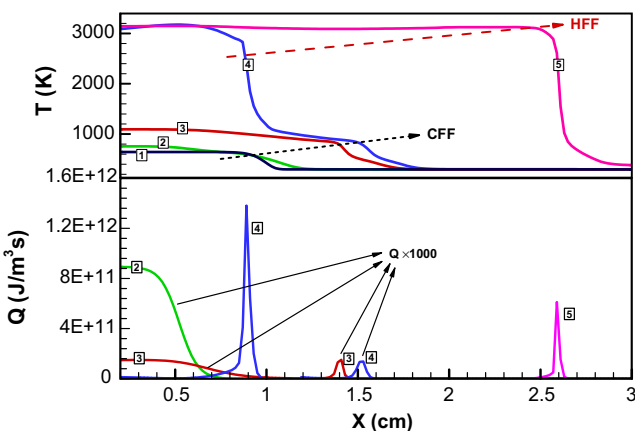


Fig. 2. Temperature and heat release profiles at various time steps for a 1-D cool flame initiated by a hot pocket of 643 K, under 1 atm. [1]: 0 ms, [2]: 16.75 ms, [3]: 22 ms, [4]: 22.236 ms, [5]: 22.286 ms. The dash arrows indicate the propagation of the cool and hot flame front segments, as CFF and HFF.

in *Q* starts to propagate into the unburnt mixture at  $x = 1.4$  cm (right curve 3), which is the CFF initiated by the low-temperature kernel. With this CFF further propagating to  $x = 1.5$  cm (right curve 4), another high-temperature front, an HFF segment with much higher *Q* (left curve 4) is induced around  $x = 0.9$  cm by the second-stage autoignition, forming an extended reaction structure consisting of distinct HFF and CFF segments. Subsequently, as autoignition ends, diffusion becomes important and gradually smooths out this combined front to approach that of the normal high-temperature premixed flame, shown as curve 5. It is noted that the instantaneous *Q* for the HFF in the (left) curve 4 is much higher than that of curve 5, because autoignition occurs much faster than diffusion, and therefore heat and species generated from autoignition cannot readily diffuse away as autoignition takes place.

For the high-temperature ignition of  $T = 967$  K, which is beyond the NTC regime, Fig. 3 shows that while the two-stage autoignition does not occur for this initial temperature as shown in Fig. 1, the initial temperature stratification, spanning from 300 K to 967 K

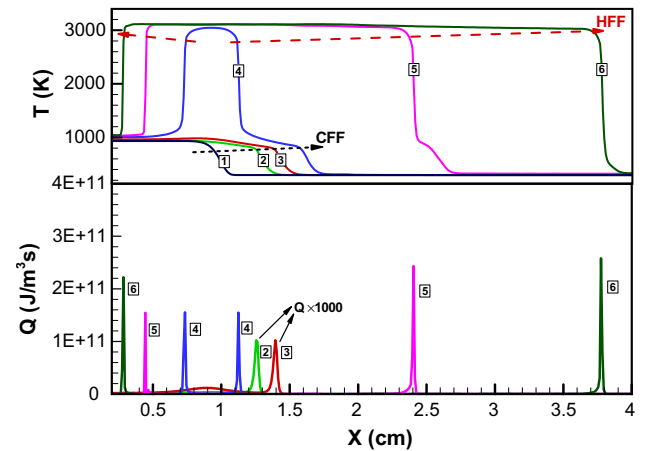


Fig. 3. Temperature and heat release profiles at various time steps for a 1-D cool flame initiated by a hot pocket of 967 K, under 1 atm. [1]: 0 ms, [2]: 20 ms, [3]: 27 ms, [4]: 29.625 ms, [5]: 29.75 ms, [6]: 29.875 ms.

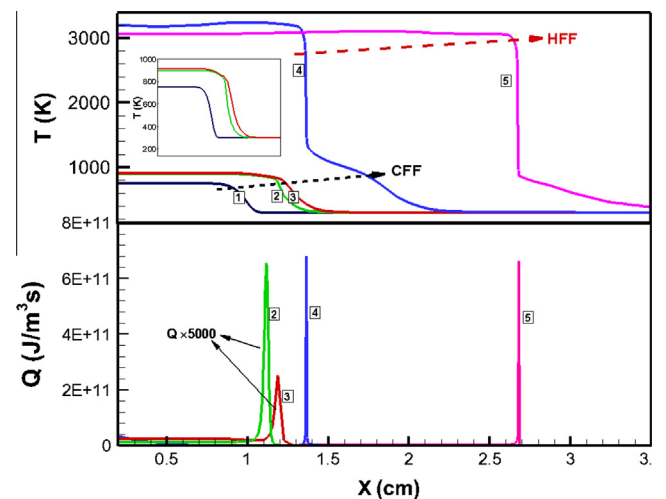


Fig. 4. Temperature and heat release profiles at various time steps for a 1-D cool flame initiated by a hot pocket of 750 K, under 1 atm. [1]: 0 ms, [2]: 7 ms, [3]: 13 ms, [4]: 23.736 ms, [5]: 23.8 ms. The zoom-in plot shows the thermal structure of propagating cool flames 1, 2 and 3.

around  $x = 1$  cm, shown as curve 1, implies that there still exists a low-temperature region favoring NTC-affected ignition, and consequently a CFF can still be initiated, as shown by curves 2 and 3. When time approaches 29 ms, while the CFF still propagates towards the unburned mixture, the main ignition event takes place at the mixing layer around  $x = 1$  cm, leading to the formation of two HFFs propagating left and right respectively, as shown in curves 4 and 5. The right-propagating reacting front with the combined CFF and HFF segments (right branches of curves 4 and 5) again is smoothed out by diffusion and eventually approaches the normal hot premixed flame (right curve 6).

Fig. 4 shows evolution of the  $T$  and  $Q$  profiles for the intermediate temperature case ( $T = 750$  K). Similar to the low- and high-temperature cases, it is seen that subsequent to the first-stage ignition, a CFF forms and propagates into the unburned mixture, as seen in curves 2 and 3 in Fig. 4. Although this front is sustained much longer due to the prolonged second-stage ignition delay  $\tau_2$ , it still lasts for only a limited residence time. After 23 ms, an HFF occurs around  $x = 1.4$  cm, as curve 4, and merges with the CFF part. Such a combined reacting front then gradually transitions to a high-temperature premixed flame, as curve 5.

These evolution processes show that a premixed cool flame is a thin thermal–chemical layer bridging the upstream ambient and downstream low-temperature quasi-equilibrium induced by low-temperature ignition, as the CFFs. Such a flame front with the inherent coupling of low-temperature chemistry and transport could generally be initiated by a hot pocket with heat deposition, regardless of the extent of the thermal stratification induced by different kernel temperatures. We have therefore demonstrated the general relevance of cool flames sustained by temperature gradients, even for hot pockets with temperatures beyond the NTC regime, as also noted in [27]. Although these cases have different durations for the self-sustained CFF propagation, eventually they all transition to the regular hot flame with the corresponding adiabatic flame temperature. In fact, by comparing Figs. 2 and 4, it is clear that kernels within the NTC regime with longer  $\tau_2$  can induce a longer self-sustained cool flame propagation period.

To further investigate the characteristics of cool flame propagation for the intermediate temperature case, evolutions of the maximum temperature and flame position are shown in Fig. 5. It is seen that the maximum temperature first stays around 750 K before the first-stage autoignition takes place. At about 3 ms, a cool flame appears and starts to propagate until 23 ms, at which it transitions to a hot flame with a much higher temperature, hence further demonstrating the existence of a much wider residence time window of 20 ms for the presence of the cool flame. A linear fitting between the flame position and the time during this stage yields the flame speed of the burnt mixture,  $S_b$ , as 23.2 cm/s. Using the thermal expansion ratio  $\sigma = 3.5$  evaluated from the unburned and burned density ratio, the unburned flame speed is then  $S_u = S_b/\sigma = 6.6$  cm/s; the magnitude is consistent with that determined from the counterflow cool flame simulation shown in Fig. 14(a) in the next section.

Comparison with the regular flame has been carried out by conducting a simple laminar flame calculation for stoichiometric DME/ $O_2/N_2$  with 15.8%  $N_2$  under 300 K and 1 atm, the same condition as the cool flame shown in Fig. 5. It is seen that the corresponding unburnt flame speed  $S_u$  for a regular hot flame is about 246.9 cm/s, with an adiabatic flame temperature 2976 K corresponding to a thermal expansion ratio of 10.0, and a thin flame thickness of about  $7.9E-03$  cm. However, the cool flame thickness similarly obtained by taking the ratio of the temperature difference on the burned and unburned side with the maximum temperature gradient in the flame structure, is about 0.137 cm, together with its much lower flame temperature of 901 K and  $S_u$  of 6.6 cm/s. From the classical thermal theory of flames, the product of the unburnt

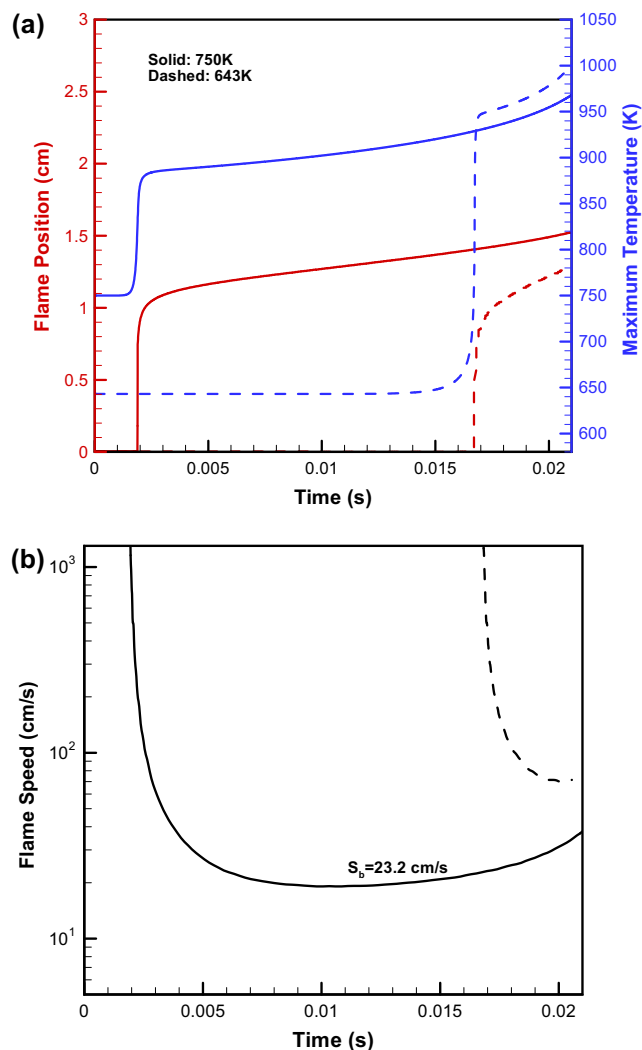


Fig. 5. (a) maximum temperature, flame position and (b) flame speed evolution for a 1-D cool flame initiated by a hot pocket of 750 K (solid) and 643 K (dash), under 1 atm.

flame speed  $S_u$  with the flame thickness  $\delta$  should scale with the mass diffusivity  $D$ , i.e.,  $S_u\delta \sim D$ . The calculated product  $S_u\delta$  for the cool flame is  $0.9$   $cm^2/s$ , while this product for the hot flame is about  $1.9$   $cm^2/s$ . Considering their largely different chemical reactivity and speciation, a difference by a factor of 2 from the flame thermal theory implies similar transport properties of the cool and regular flames, and the physical consistency of the cool flame speed.

Having determined the propagation speed for the flame identified above, it is important to recognize that a “cool flame speed” is fundamentally not a well-defined concept as compared to the well-defined laminar flame speed, even in the 1-D planar configuration. Specifically, the downstream of a cool flame is only one of quasi-chemical equilibrium in a state of transition such that, with sufficiently long residence time, it will eventually evolve to the final equilibrium state characterized by the adiabatic flame temperature of the mixture. As such, a steady-state 1-D premixed cool flame with an attendant propagation speed in the doubly-infinite domain, where infinite residence time is allowed for chemical equilibrium downstream and chemical frozen condition upstream, is not conceptually viable and as such does not exist.

Having recognized the failure of a 1-D cool flame to assume an eigen-mode of propagation in the doubly infinite regime, there are at least two scenarios in which a steadily propagating, globally-

planar cool flame can be envisioned. The first is the freezing of the downstream chemistry through radiation loss, rendering it to be asymptotically non-reactive. The problem is not unlike that of the cold-boundary difficulty in the conventional premixed flame analysis, in that given infinite time any reaction with a finite temperature will be able to completely react; in the far upstream for the conventional flame and far downstream for the cool flame, even with radiative loss. Thus the eigenvalue nature of the problem can only be defined in some asymptotic sense.

The second scenario to establish a steady cool flame is to truncate the downstream flow time so as to prevent transition of the cool flame chemistry to reach the state of chemical equilibrium. The downstream state of this flame is then in quasi-equilibrium with the cool flame chemistry. This can be readily accomplished by aerodynamically straining the flow, as in the case of a stagnation flow or counterflow. We shall therefore study in the following stretched cool flames in the counterflow, both computationally and experimentally. Indeed, since the laminar flamelets within a turbulent flame structure are mostly positively stretched, the results bear relevance to practical situations.

It is also worth noting that the artificial air we adopted with significant  $N_2$  reduction is not a necessary condition for propagating cool flames, which instead largely depends on the thermodynamic conditions. A propagating cool flame can also be observed in regular air if the pressure is high enough, as in the environments of rapid compression machine and engine experiments. As shown in the next section, ignition induced by low temperature chemistry becomes much more pronounced if the dilution effect from nitrogen is reduced. The reason is that with the same low temperature heat release, less inert content leads to higher increment of the cool flame temperature.

### 3. Stretched cool flame in counterflow – computational results

In order to explore if a steady cool flame with truncated downstream flow time can be physically realized, a premixed counterflow configuration consisting of a hot  $N_2$  stream flowing against a premixed  $DME/O_2/N_2$  stream at room temperature was studied, based on the following considerations. First, the flow along the center line is 1-D and the residence time is well characterized by the aerodynamic strain. Furthermore, by fixing the strain rate and varying the inert boundary temperature, the system could show multiple solutions corresponding to those defined by the characteristic S-shaped response curves, with the lower and upper turning points respectively designate the ignition and extinction states of the system. It is therefore of interest to explore if a premixed cool flame can be stabilized and as such also exhibit distinct ignition and extinction states, in manners similar to those of flames in practical situations with finite local residence times.

The governing equations for the counterflow flame simulation are given in [28]. The simulation employs the damped Newton's method and time integration solution scheme to solve the ordinary differential equations with boundary conditions specified on both sides of the potential flow. S-curve marching is performed using the flame-controlling method of Nishioka et al. [29], with detailed chemistry and transport database. The critical states of ignition and extinction can then be assessed through the multiple turning points of the S-curve. The simulation conditions are as follows: the upper boundary consists of a mixture of DME, oxygen and nitrogen at a fixed temperature of 300 K, while the lower boundary is nitrogen at a higher temperature. The separation distance between the nozzle exits is 2 cm. To generate an S-curve, marching is performed by changing the nitrogen-side boundary temperature with fixed strain rate.

Fig. 6 shows the S-curve for a stoichiometric  $DME/O_2$  mixture with 15.8%  $N_2$  at different strain rates, using the maximum  $CH_3$  concentration as a representative global response to the nitrogen boundary temperature. Due to the fact that the temperature variation during low-temperature ignition shows an S-curve response, all radicals show corresponding S-curve responses with the same turning point behavior, as has also been shown in Refs. [10,11]. Here  $CH_3$  is chosen as the system indicator because it can also indicate high-temperature chemistry while the low-temperature species (e.g.,  $CH_3OCH_2O_2$ ) cannot. It is seen that, for each of the two lower strain rates of  $k = 20/s$  and  $50/s$ , two distinctive ignition turning points, I1 and I2, appear, with I1 controlled by the low-temperature chemistry, and I2 by the intermediate- to high-temperature chemistry. Furthermore, when the strain rate is increased to  $100/s$ , the S-curve induced by the low-temperature chemistry loses its non-monotonicity and becomes stretched, due to the suppression of low-temperature heat release and thereby thermal feedback at reduced residence time [11]. It is also noted that, for  $k = 20/s$ , the system directly transitions to the hot flame upon attaining the state of the first-stage ignition, in that I2 is not accessed with increasing boundary temperature, and as such demonstrates the significance of low-temperature chemistry at low strain rates. This is to be contrasted with the case of  $k = 50/s$ , in that the system can actually maintain a state of steady burning characterized by the low-temperature chemistry after attaining the first stage ignition. Intense burning is attained only when the state of I2 is reached with further increase in temperature.

We next investigate the transition to ignition induced by the low-temperature chemistry. Based on the steady-state S-curve, the transition behavior is studied by including the unsteady term and introducing a 1% perturbation to the local temperature profile of the steady-state solution at the first ignition turning point. Fig. 7 shows the transition process of the low-temperature chemistry induced ignition I1, for  $k = 50/s$ . It is seen that after introducing the perturbation at  $t = 0$ , the system maximum temperature first drops due to thermal diffusion. Then both the maximum temperature and maximum formaldehyde mole fraction suddenly increase around  $t = 0.2$  s and eventually approach the steady-state cool flame solution on the upper branch of the low-temperature S-curve, with the maximum temperature in the flow field being about 100 K higher than the boundary temperature, suggesting weak combustion and heat release from the low-temperature

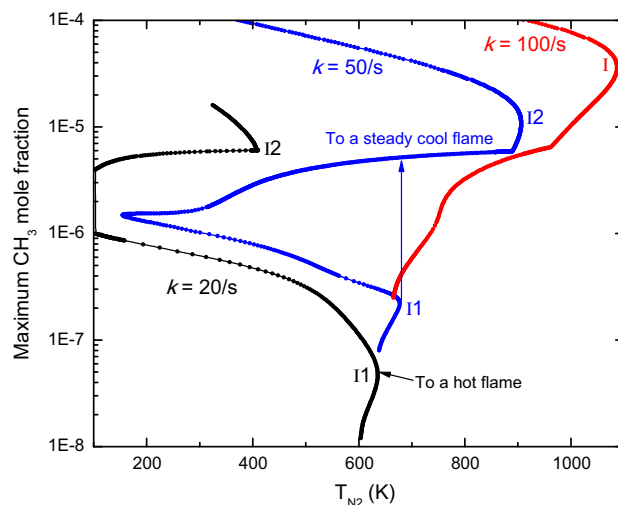


Fig. 6. S-curve response of stoichiometric  $DME/O_2$  mixture with 15.8%  $N_2$  vs. hot  $N_2$  at different strain rates 20/s, 50/s and 100/s, showing the different behavior of low temperature ignition.

chemistry. This therefore demonstrates that a steady-state cool flame can be established with a residence time corresponding to an appropriate aerodynamic strain rate. However, for the even lower strain rate of  $k = 20/s$ , shown in Fig. 8, the system evolves towards a hot flame around  $t = 0.4$  s. Such a transition process shows that, with long enough flow residence time at low strain rate, ignition induced by low-temperature chemistry can cause autoignition and eventually achieve intense burning, consistent with the steady-state S-curve interpretation of Fig. 6.

Figs. 7 and 8 together then show the different transition processes of low-temperature chemistry induced ignition under different strain rates, and further support the strain rate window identified for the appearance of a steady-state cool flame shown in Fig. 6, with longer residence time promoting autoignition and shorter residence time suppressing the thermal feedback. As such, we have demonstrated that the occurrence of steady premixed cool flames strongly depends on the flow residence time.

We next conduct a parametric study to further show the response of flames induced by the low-temperature chemistry by varying the amount of dilution and equivalence ratio. For the case of  $50/s$  strain rate within the cool flame strain rate window, effects of dilution are observed by fixing the equivalence ratio and varying the amount of the inert, as shown in Fig. 9. It is seen that with decreasing dilution, the S-curve becomes more pronounced. This is due to the fact that, with equivalence ratio and therefore heat release rate of the low-temperature chemistry fixed, the temperature increases with reduced dilution. Consequently, the nonlinear thermal feedback to the S-curve phenomena becomes stronger. On the other hand, with dilution increased to a certain amount, the S-curve induced by the low-temperature chemistry becomes stretched and the system response becomes monotonic without ignition and extinction.

To identify the dependence of low-temperature ignition on the equivalence ratio, mixtures with different equivalence ratios but the same amount of  $N_2$  dilution are simulated for  $50/s$  and 1 atm, shown in Fig. 10. It is seen that the ignition turning point is not sensitive to the equivalence ratio, yielding fairly close ignition temperatures. However, with increasing equivalence ratio, the maximum  $CH_3$  mole fraction gradually increases, indicating stronger reactivity for the low-temperature chemistry under richer conditions.

Having identified the ignition characteristics in the asymmetric counterflow, we next study the thermal and chemical structures of the cool flame in the symmetric twin-flame counterflow, using OPPDIF [30] with the same kinetic model and transport properties. The nozzles are again separated by 2 cm. A plug flow boundary

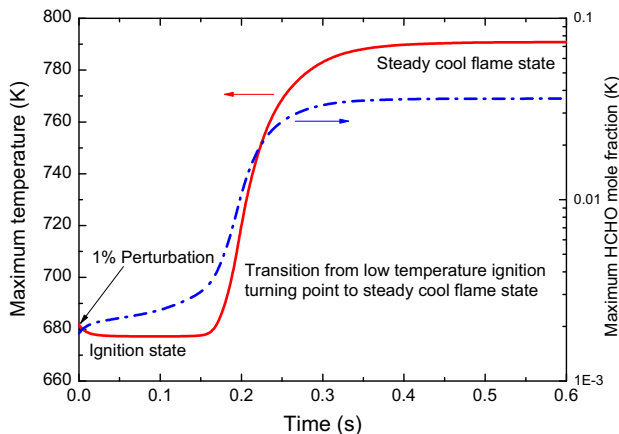


Fig. 7. Transition from low temperature chemistry induced ignition to a steady cool flame, for stoichiometric DME/ $O_2$  with 15.8%  $N_2$ , 1 atm,  $k = 50/s$ .

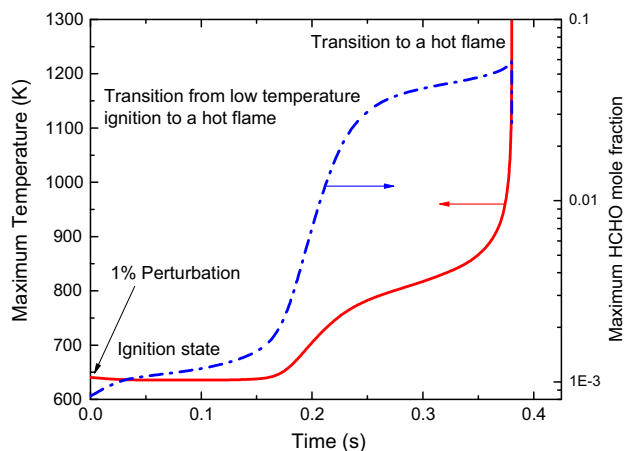


Fig. 8. Transition from low temperature chemistry induced ignition to a hot flame, for stoichiometric DME/ $O_2$  with 15.8%  $N_2$ , 1 atm,  $k = 20/s$ .

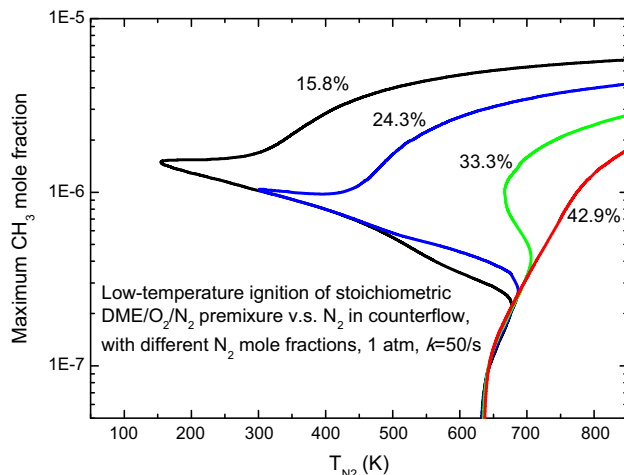


Fig. 9. Low temperature chemistry induced ignition for stoichiometric DME/ $O_2$  with various amount of  $N_2$ , 1 atm,  $k = 50/s$ .

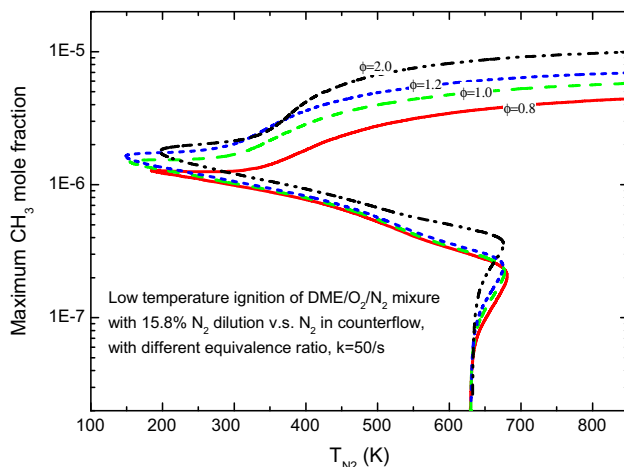
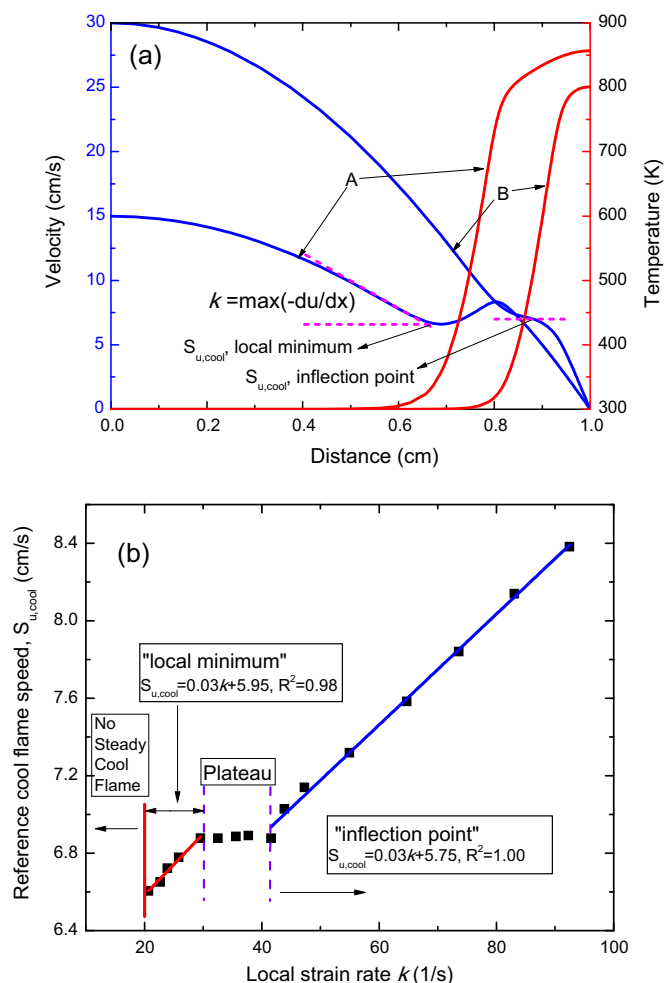


Fig. 10. Low temperature chemistry induced ignition for DME/ $O_2$  with various equivalence ratios and 15.8%  $N_2$ , 1 atm,  $k = 50/s$ .

condition is set for the boundary velocity while the boundary temperature is set at 300 K. Fig. 11(a) shows two cool flames with different boundary velocities of 15 cm/s (case A) and 30 cm/s (case B),



**Fig. 11.** (a) Velocity and temperature profiles for stoichiometric DME/O<sub>2</sub>/N<sub>2</sub> cool flames with 15.8% N<sub>2</sub> in a symmetric counterflow with plug flow boundary condition under 1 atm, showing local minimum (A) and inflection point (B) behavior for the reference cool flame speed corresponding to strong and weak thermal expansion, respectively. (b) Reference cool flame speed for the mixture of Fig. 11(a) at different strain rates, showing a linear behavior as a function of strain rate.

providing different strain rates, for stoichiometric DME/O<sub>2</sub>/N<sub>2</sub> mixture with 15.8% N<sub>2</sub> under 1 atm. It is seen that, for the low strain rate case, the flame temperature is higher such that thermal expansion is larger, resulting in a non-monotonic velocity profile in the flame zone. The local strain rate  $k$  characterizing the flame residence time can be defined as the local maximum strain rate upstream of the flame, and the local minimum flow velocity as the reference flame speed of the cool flame  $S_{u,cool}$  for the corresponding strain rate, in the same manner as that of the hot flame characterization in the counterflow configuration [31]. It is seen that in case A, the local strain rate is about 20.7/s and the local minimum velocity is 6.6 cm/s, and as such demonstrates that the reference cool flame speed  $S_{u,cool}$  is much slower than the laminar flame speed under the same condition. In case B for which the exit velocity doubles to 30 cm/s, the flame temperature and the thermal expansion effect on the flow velocity decrease. Consequently the nonmonotonic behavior in the velocity profile is reduced to an inflection point for the higher strain rate, leading to ambiguity in evaluating the cool flame speed. For such cases, the reference cool flame speed corresponding to the local maximum strain rate is defined as the flow velocity at the inflection point, as shown in Fig. 11(a). For the cases with intermediate local strain rate between

those corresponding to cases A and B, thermal expansion is also intermediate, which causes a plateau behavior in the corresponding velocity profile.

We now systematically show how a premixed cool flame responds to the strain rate variation. The reference cool flame speed as a function of local strain rate is given in Fig. 11(b), for the same mixture in Fig. 11(a). Four different regimes could be identified by varying the strain rate. For a low enough strain rate  $k$ , below 20/s, ignition induced by the low-temperature chemistry has long enough residence time to transition to an intense burning hot flame, therefore a steady-state cool flame does not exist, as demonstrated in Fig. 8. With  $k$  increased from 20 to 30/s, a steady-state cool flame can be initiated, with large enough thermal expansion to cause a nonmonotonic velocity profile in the flame zone as case A in Fig. 11(a). In this regime, the reference cool flame speed at the minimum point varies linearly with the strain rate, and hence the flame stretch rate, although in an insensitive manner. With  $k$  further increased to the range of 30–40/s, thermal expansion decreases as a result of the reduced residence time and the nonmonotonic velocity profile reduces to a plateau behavior, where the reference cool flame speed is even more insensitive to strain rate variations. With  $k$  further increased, the plateau behavior is reduced to the inflection point behavior as case B in Fig. 11(a), for which the reference cool flame speed again shows linear dependence on  $k$  with the same slope as in the regime with local minimum velocity. These calculations hence shed light on the dynamic response of laminar premixed cool flames to the variation of aerodynamic strain and flame stretch.

Fig. 12 shows the chemical structure of the calculated DME/O<sub>2</sub>/N<sub>2</sub> cool flame with 15.8% N<sub>2</sub> and 18 cm/s boundary velocity. It is seen that the major species are those involved in the first-stage autoignition process, and that both fuel and oxygen are only slightly consumed, producing H<sub>2</sub>O, CO, formaldehyde, etc., in the downstream. Important radicals in high temperature flames such as H, OH have rather small concentrations, with peak values being around 0.1 ppm. To identify the critical reactions for the cool flame propagation, dimensionless sensitivity coefficients of each reaction to the reference cool flame speed, defined as  $\partial \ln S_{u,cool} / \partial \ln A_i$  and normalized by the maximum absolute value, are calculated for the case of Fig. 9 and shown in Fig. 13. It is seen that the cool flame speed is mainly controlled by the low-temperature chemical kinetics. Reactions promoting cool flame propagation are mainly the low-temperature chain branching and propagation reactions, including H abstraction of DME, RO<sub>2</sub> isomerization into QOOH,

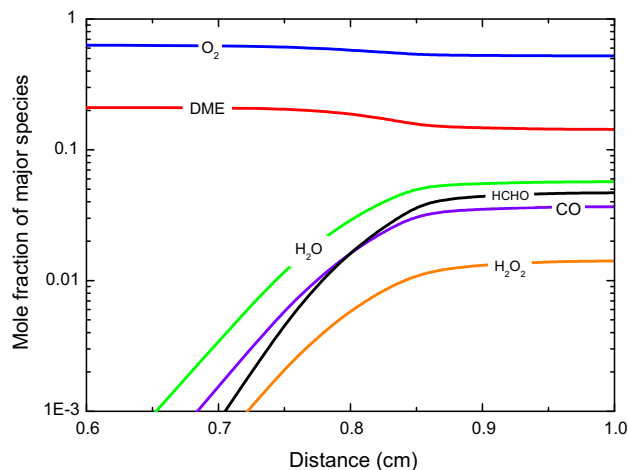


**Fig. 12.** Mole fractions of major species for a stoichiometric DME/O<sub>2</sub>/N<sub>2</sub> cool flames with 15.8% N<sub>2</sub> in a symmetric counterflow configuration with inlet velocity 18 cm/s, under 1 atm.

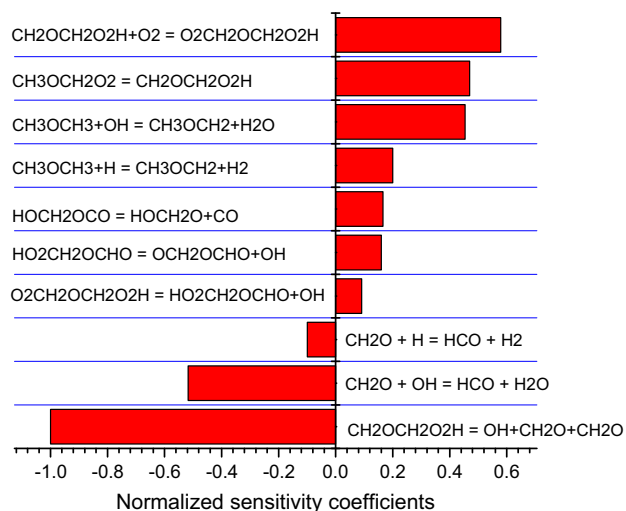


Fig. 13. Normalized sensitivity coefficients demonstrating important reactions for cool flame propagation corresponding to the case shown in Fig. 12.

and  $\text{O}_2$  addition to  $\text{QOOHO}_2$ , etc. On the contrary, a major reaction retarding cool flame propagation is the  $\beta$ -scission of the  $\text{QOOH}$  radicals forming the relatively stable intermediate  $\text{HCHO}$ , which competes with the low-temperature chain branching reactions.

It is then of interest to show the dependence of the cool flame temperature and speed on the equivalence ratio. For a fixed local strain rate of 25/s, the reference flame speeds and temperatures of  $\text{DME}/\text{O}_2/\text{N}_2$  cool flames, with  $\text{O}_2$  and  $\text{N}_2$  volume ratio 4:1 and varying equivalence ratio, are shown in Fig. 14(a). It is seen that, contrary to the hot flame cases, the cool flame temperature gradually increases with equivalence ratio and reaches a limit under rich conditions. This result is consistent with previous homogeneous autoignition studies [10,32], in that in a wide range of equivalence ratios, the richer the mixture, the larger the temperature increase at the end of the first-stage autoignition. The cool flame temperature should be bounded by the “ceiling temperature”, which is the equilibrium temperature of the  $\text{RO}_2$  radical formation reaction  $\text{R} + \text{O}_2 = \text{RO}_2$ . Under rich conditions, the dilution effect from nitrogen is weaker and can lead to a higher cool flame temperature. On the other hand, instead of the strong dependence on flame temperature for the high-temperature laminar flames [27], the cool flame speed does not follow the same trend as the cool flame temperature. Also, it shows a modest sensitivity in terms of the equivalence ratio, and the range of the flame speed is around 6–7 cm/s. The maximum value is around stoichiometric, similar to that of the laminar flame speed. The maximum  $\text{HCHO}$  mole fraction is also calculated and shown in Fig. 14(b), indicating the increase of chemical reactivity of the cool flames with increasing equivalence ratios.

#### 4. Stretched cool flame in counterflow – experimental observations

Experiments were carried out in a counterflow facility used in [12,16,33] to explore if the predicted premixed cool flame indeed exists. Briefly, the counterflow setup consists of two vertically opposing quartz tubes with 20 mm diameters and separated by 20 mm. A room-temperature  $\text{DME}/\text{O}_2$  mixture is issued from the lower tube, flowing against an  $\text{N}_2$  jet, which is directed downward by the upper tube and electrically heated by both inner and outer heaters. Both upper and lower jets are surrounded by  $\text{N}_2$  guard flows. The attempt to observe the cool flame was conducted by either gradually increasing the  $\text{N}_2$  temperature to about 700 K

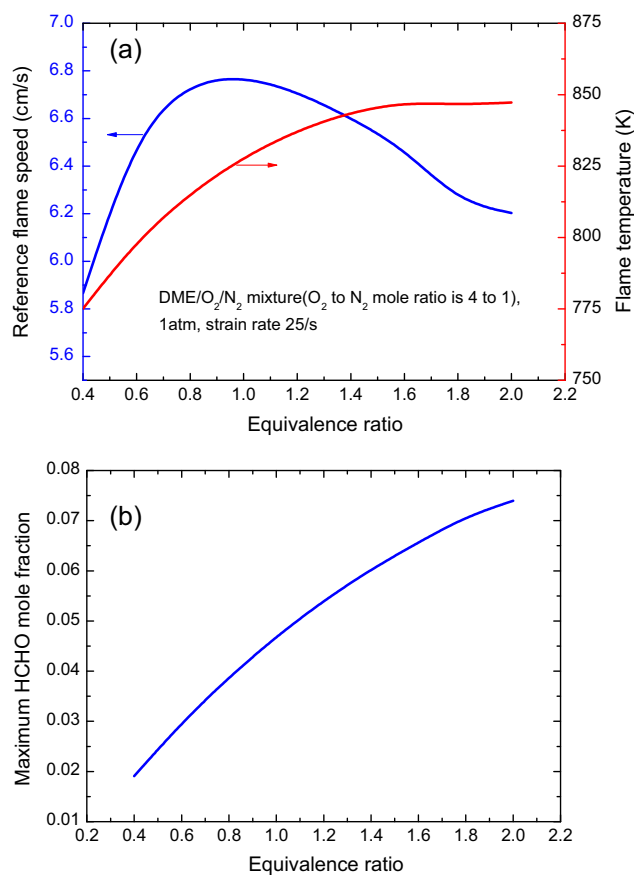


Fig. 14. (a) Flame speeds and temperatures, (b) Maximum  $\text{HCHO}$  mole fraction for the cool flame calculations for atmospheric  $\text{DME}/\text{O}_2/\text{N}_2$  mixtures with 15.8%  $\text{N}_2$  in a symmetric counterflow configuration with various equivalence ratios at 300 K, and the local strain rate is fixed around 25/s.

under proper flow rate, or gradually varying the flow rate with fixed  $\text{N}_2$  boundary temperature. Since a cool flame is hardly observable by eye or camera in the visible spectrum range, a high-sensitivity monochrome CCD camera with high relative response in the UV spectrum (CCE-B013-U, Mightex) was setup to capture the global chemiluminescence from the low temperature chemistry. It is noted that extensive work has been performed on the chemiluminescence from the excited species in flames, such as excited  $\text{HCHO}$  molecule [34], excited  $\text{CO}_2$  molecule [34–36], excited  $\text{CH}$  radical [36–38] and  $\text{OH}$  [36,37,39] radical. Since the main goal of the current experiment is to prove the existence of a steady laminar premixed cool flame in the strained flow, the global chemiluminescence from the low temperature chemistry is sufficient to be used as an indicator of the location and burning intensity of the cool flame. Consequently, a quantitative validation of the chemistry by separate measurements of the emission from each of these intermediates was not conducted and certainly merits further efforts.

To quantify the flow and temperature boundary conditions, an uncoated K-type (Chromel–Alumel) thermocouple was used to measure the maximum exit temperature of the heated  $\text{N}_2$  and the flow rate was measured by a flow calibrator (Gilibrator-2 Flow Calibrator, Standard Flow Cell, Sensidyne). From discussions in Section 2, it is noted that the dilution effect from  $\text{N}_2$  in the mixture can be essential for the existence of a premixed cool flame even at a fixed strain rate. Consequently, mixtures of  $\text{DME}$  and  $\text{O}_2$  without  $\text{N}_2$  addition were used to facilitate the experimental observation. To prevent flashback of the possible hot flames generated, two porous flame quenchers (with 1  $\mu\text{m}$  average pore size) were

connected in between the flow tubes and downstream of the mixing chamber.

To validate the observation, we first performed the experiment of a reactive case with heated  $N_2$  (686 K) flowing against a DME/ $O_2$  mixture of equivalence ratio 1.5; shown as the left image of Fig. 15. Clearly a thin layer with chemiluminescence is observed in the flow field. When  $O_2$  is replaced by the same amount of  $N_2$  to keep the same flow rate and boundary temperatures, the reactive layer disappeared as shown in the right image of Fig. 15. The cool flame would recur if the amount of  $N_2$  in the mixture was replaced by  $O_2$ . Furthermore, if the amount of DME was replaced by the same amount of  $N_2$ , the observed cool flame again disappeared and recurred when DME was changed back. From this behavior, we conclude that the observed reactive layer is induced by the chemistry between DME and  $O_2$  at low temperatures. In addition, a pass-band filter corresponding to the chemiluminescence from the excited HCHO molecules, with characteristic spectrum peaking around 400 nm [12], was utilized to verify the observation. It is seen that the chemiluminescence appears at the same location, although the intensity is much weaker with the filter and therefore is not shown.

The flow rates were also controlled to ensure that the experimental condition matches the strain rate window for the occurrence of cool flames, as discussed in Section 2. Specifically, the flow rate of the hot  $N_2$  (686 K) from the upper nozzle is about  $1826 \text{ cm}^3/\text{min}$  while that of the DME/ $O_2$  mixture with various equivalence ratios is fixed at  $960 \text{ cm}^3/\text{min}$ , from the bottom nozzle with ambient temperature, 300 K. Fig. 16 shows the images taken for the steady state counterflow cool flames observed with DME/ $O_2$  mixtures with various equivalence ratios from 0.8 to 1.8.

The above observation indicates that there are two qualitative trends for the kinetic and dynamic behavior of the premixed cool flames. First, with increasing equivalence ratio from lean to rich, the chemiluminescence from the cool flame becomes progressively more intense. This is consistent with the calculated concentration of HCHO (Fig. 14(b)), which is a characteristic species indicating the low-temperature chemistry, showing that it increases with equivalence ratio for the same flow condition, and hence stronger chemiluminescence. However, it should be noted that the chemiluminescence observed is partially from the excited HCHO molecules, instead of the ground state HCHO molecules. Since HCHO

is a major characteristic species showing the low-temperature chemistry, the qualitative agreement implies stronger low-temperature reactivity and chemiluminescence with increased equivalence ratio, even for rich mixtures. Second, the position of the reaction layer almost does not change for the same boundary flow rate. This observation then demonstrates the insensitive dependence of the cool flame speed on the mixture equivalence ratio. As shown in Fig. 14(a), for a wide range of equivalence ratios (0.4–2.0), the variation of the cool flame speed is within about 15%, which is much less than the variation of normal laminar flame speeds in terms of the equivalence ratio.

Compared with the conventional measurements of laminar flame speeds, a quantitative measurement of the cool flame speed embodies considerable difficulty. Specifically, the local flow velocity is low and the reaction layer is quite weak, and as such it responds sensitively to any flow disturbance from intrusive methods, such as thermocouple measurement. Furthermore, seeding particle loading in LDV (Laser Doppler Velocimetry) or PIV (Particle Image Velocimetry) measurements could modify the boundary conditions or the local flow field to cause flame extinction or autoignition. It is also noted that the observed reaction layer is from the chemiluminescence of the cool flame chemistry, corresponding to the position of the peak concentration of excited HCHO molecules in the downstream of the cool flame. Therefore, the observed cool flame is still at the downstream of the location for the reference velocity as shown in Fig. 11.

Fig. 17 compares the experimental image with detailed calculation for the counterflow configuration with hot  $N_2$  (upper, 686 K) flowing against DME/ $O_2$  mixture with equivalence ratio 1.6. The position of the captured chemiluminescence well corresponds to the peak of the simulated temperature profile and also the HCHO profile. It is seen that the observed chemiluminescence is at a location very close to the stagnation plane, where the corresponding flow velocity is quite low. However, from the calculation, it is seen that the location for the reference cool flame speed is about 0.4 cm away from the chemiluminescence zone, leading to large ambiguity in the estimation of the location of the reference cool flame speed and therefore the reference cool flame speed. With thermal expansion from the cool flame as an additional unknown, it is therefore not feasible to meaningfully determine the cool flame speed based on the experimental chemiluminescence observation.

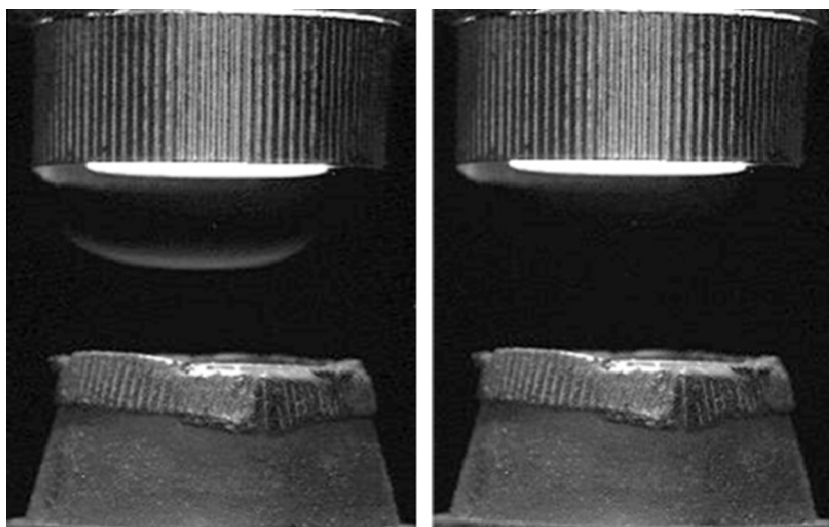


**Fig. 15.** Observations for experiments of hot  $N_2$  vs. DME/ $O_2$  mixture (left) and hot  $N_2$  vs. DME/ $N_2$  mixture (right) with the same flow rate and same boundary temperatures. The flow rate of the hot  $N_2$  (686 K) from the upper nozzle is about  $1826 \text{ cm}^3/\text{min}$  while that of the DME/ $O_2$  mixture with various equivalence ratios is fixed at  $960 \text{ cm}^3/\text{min}$ , from the bottom nozzle with ambient temperature, 300 K.

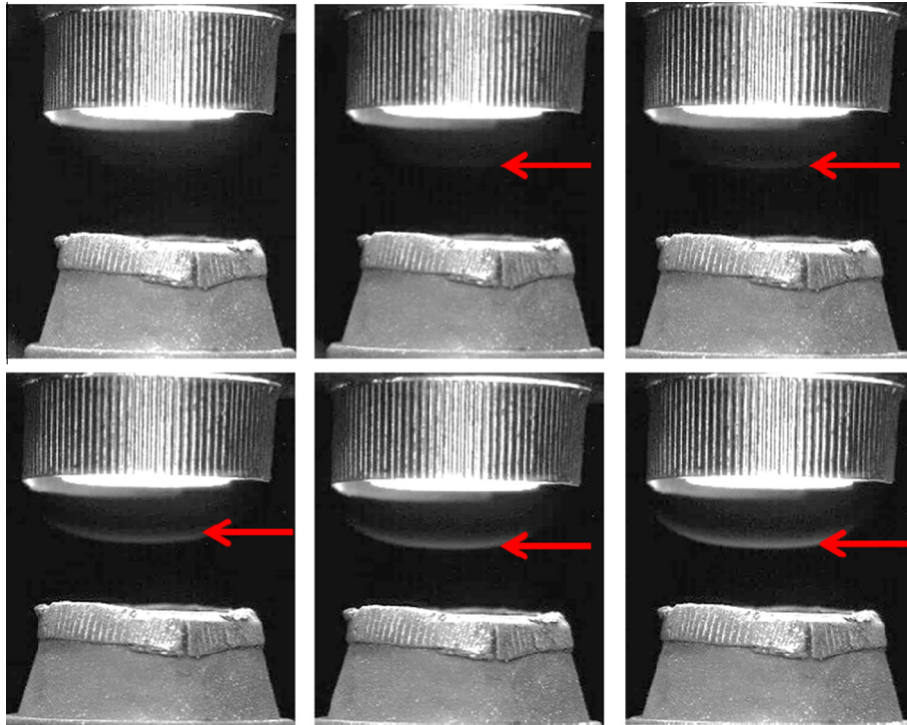


**Fig. 16.** Images taken with a CCD camera for atmospheric cool flame observations (shown as the arrow) in counterflow configuration with hot  $N_2$  (upper, 686 K) flowing against DME/ $O_2$  mixture with various equivalence ratios of 0.8, 1.0, 1.2, 1.4, 1.6, 1.8 (from left to right and from top to bottom).

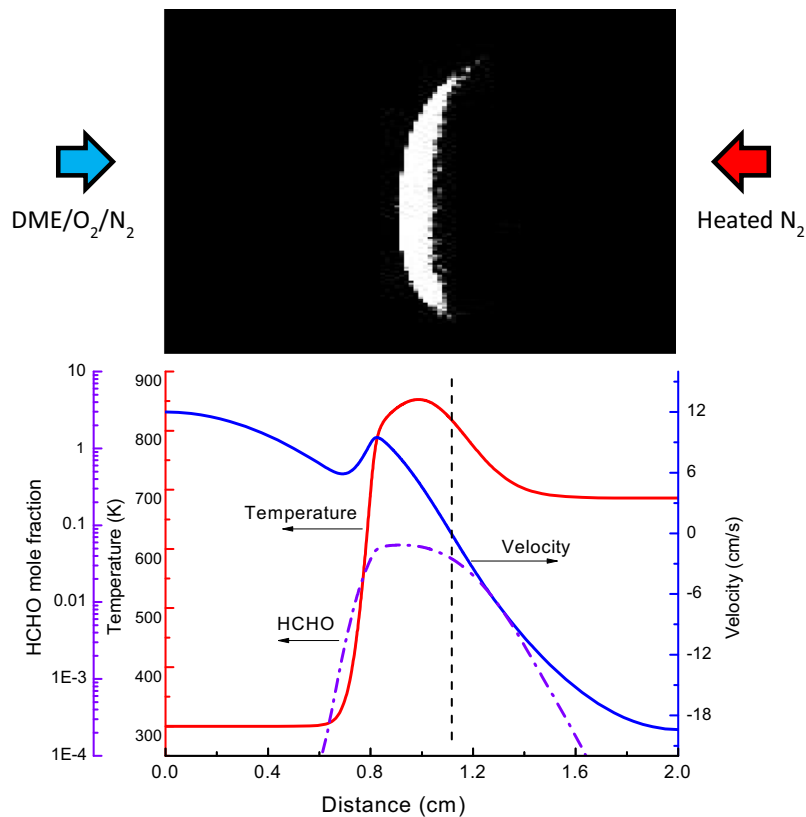


**Fig. 17.** Comparison for the premixed cool flame image in counterflow configuration with hot  $N_2$  (upper, 686 K) flowing against DME/ $O_2$  mixture with equivalence ratios of 1.6 with detailed numerical simulation. Dash line in the simulation indicates the location for the stagnation plane.

In summary, we have successfully established and observed a steady cool flame in the aerodynamically strained counterflow, whose characteristics correspond well to those obtained from

computations. Furthermore, while it is beyond the scope and experimental capability of the present investigation to probe the underlying chemistry, we have nevertheless demonstrated the fea-

sibility of using the counterflow to further study the cool flame characteristics including its chemistry with advanced laser instrumentation, such as HCHO-PLIF [40] and OH-PLIF [41].

## 5. Conclusions

In the present investigation, we have first computationally studied the initiation and propagation of premixed cool flames for DME/O<sub>2</sub>/N<sub>2</sub> mixtures in the 1-D planar configuration as well as the counterflow configuration. The results demonstrate that a residence time window exists for the occurrence of cool flames; external to this window a cool flame either cannot be initiated or will transition to a hot flame. Parametric study shows that the cool flame regime is sensitive to the amount of dilution in the flow, and that the cool flame becomes more intense at richer conditions. Global parameters such as the reference cool flame speed and cool flame temperature have been studied in a symmetric counterflow for various strain rates and equivalence ratios, with the controlling reactions identified. The results show that the premixed cool flame speeds are relatively low, around 6–7 cm/s, and are much less sensitive in terms of equivalence ratio variations. Experimental investigations have also been carried out in a counterflow, with a steady cool flame observed with a CCD camera with high sensitivity of the UV band. Such observations qualitatively demonstrate stronger cool flame chemiluminescence and insensitive change in the flame position with increasing equivalence ratios, which correspond well with the detailed numerical simulation.

## Acknowledgement

This work was supported by the Air Force Office of Scientific Research under the technical monitoring of Dr. Mitat Birkan, and the Microgravity Combustion Program of NASA.

## References

- [1] Davy H. Some new experiments and observations on the combustion of gaseous mixtures, with an account of a method of preserving a continued light in mixtures of inflammable gases and air without flame. *Philos Trans R Soc Lond* 1817;107:77–86.
- [2] Griffiths JF, Scott SK. Thermokinetic interactions: fundamentals of spontaneous ignition and cool flames. *Prog Energy Combust Sci* 1987;13:161–97.
- [3] Battin-Leclerc F. Detailed chemical kinetic models for the low-temperature combustion of hydrocarbons with application to gasoline and diesel fuel surrogates. *Prog Energy Combust Sci* 2008;34:440–98.
- [4] Ciezki HK, Adomeit G. Shock-tube investigation of self-ignition of *n*-heptane-air mixtures under engine relevant conditions. *Combust Flame* 1993;93:421–33.
- [5] Lewis B, von Elbe G. Combustion, flames and explosions of gases. 2nd ed. Academic Press Inc.; 1961.
- [6] Wang Z, Qi Y, He X, Wang J, Shuai S, Law CK. Analysis of pre-ignition to super-knock: hotspot-induced deflagration to detonation. *Fuel* 2015;144:222–7.
- [7] Sheinson RS, Williams FW. Chemiluminescence spectra from cool and blue flames. *Combust Flame* 1973;21:221–30.
- [8] Benson SW. The kinetics and thermochemistry of chemical oxidation with application to combustion and flames. *Prog Energy Combust Sci* 1981;7:125–34.
- [9] Lignola PG, Reverchon E. Cool flames. *Prog Energy Combust Sci* 1987;13:75–96.
- [10] Law CK, Zhao P. NTC-affected ignition in nonpremixed counterflow. *Combust Flame* 2012;159:1044–54.
- [11] Zhao P, Law CK. The role of global and detailed kinetics in the first-stage ignition delay in NTC-affected phenomena. *Combust Flame* 2013;160:2352–8.
- [12] Deng S, Zhao P, Zhu D, Law CK. NTC-affected ignition and low-temperature flames in nonpremixed DME/air counterflow. *Combust Flame* 2014;161:1993–7.
- [13] Nayagam V, Dietrich DL, Ferkul PV, Hicks MC, Williams FA. Can cool flames support quasi-steady droplet burning? *Combust Flame* 2012;159:3583–8.
- [14] Farouk TI, Hicks MC, Dryer FL. Multistage oscillatory “Cool Flame” behavior for isolated alkane droplet combustion in elevated pressure microgravity condition. *Proc Combust Inst* 2015;35:1701–8.
- [15] Won SH, Jiang B, Diévert P, Sohn CH, Ju Y. Self-sustaining *n*-heptane cool diffusion flames activated by ozone. *Proc Combust Inst* 2015;35:881–8.
- [16] Zhao P, Yuan W, Sun H, Li Y, Kelley AP, Zheng X, et al. Laminar flame speeds, counterflow ignition, and kinetic modeling of the butene isomers. *Proc Combust Inst* 2015;35:309–16.
- [17] Agnew WG, Agnew JT. Composition profiles of the diethyl ether-air two-stage reaction stabilized in a flat-flame burner. *Proc Combust Inst* 1965;10:123–38.
- [18] Ma ASC, Moore NPW. Auto-ignition and knock characteristics of benzene-*n*-heptane-air mixtures. *Combust Flame* 1966;10:245–58.
- [19] Ju Y, Reuter C, Won S. Numerical simulations of premixed cool flames of dimethyl ether/oxygen mixtures. *Combust Flame* 2015;162:3580–8.
- [20] Gao J, Nakamura Y. Low-temperature ignition of dimethyl ether: transition from cool flame to hot flame promoted by decomposition of HPMF (HO<sub>2</sub>CH<sub>2</sub>OCHO). *Combust Flame* 2015. <http://dx.doi.org/10.1016/j.combustflame.2015.09.034>.
- [21] Bhagatwala A, Luo Z, Shen H, Sutton JA, Lu T, Chen JH. Numerical and experimental investigation of turbulent DME jet flames. *Proc Combust Inst* 2015;35:1157–66.
- [22] Deng S, Zhao P, Mueller ME, Law CK. Autoignition-affected stabilization of laminar nonpremixed DME/air coflow flames. *Combust Flame* 2015;162:3437–45.
- [23] Chen Z. Studies on the initiation, propagation, and extinction of premixed flames, Ph.D. Thesis, Princeton University; 2008.
- [24] Chen Z. Effects of radiation and compression on propagating spherical flames of methane/air mixtures near the lean flammability limit. *Combust Flame* 2010;157:2267–76.
- [25] Chen Z, Burke M, Ju Y. Effects of Lewis number and ignition energy on the determination of laminar flame speed using propagating spherical flames. *Proc Combust Inst* 2009;32:1253–60.
- [26] Chen Z. On the extraction of laminar flame speed and Markstein length from outwardly propagating spherical flames. *Combust Flame* 2011;158:291–300.
- [27] Fairlie R, Griffiths JF, Hughes KJ, Pearlman H. Cool flames in space: experimental and numerical studies of propane combustion. *Proc Combust Inst* 2005;30:1057–64.
- [28] Smooke MD, Puri IK, Seshadri K. A comparison between numerical calculations and experimental measurements of the structure of a counterflow diffusion flame burning diluted methane in diluted air. *Proc Combust Inst* 1988;21:1783–92.
- [29] Nishioka M, Law CK, Takeno T. A flame-controlling continuation method for generating S-curve responses with detailed chemistry. *Combust Flame* 1996;104:328–42.
- [30] Lutz AE, Kee RJ, Grcar JF, Rupley FM. OPPDIF: A Fortran program for computing opposed-flow diffusion flames. Sandia National Laboratories Report SAND 96-8243; 1996.
- [31] Ji C, Dames E, Wang YL, Wang H, Egolfopoulos FN. Propagation and extinction of premixed C<sub>5</sub>–C<sub>12</sub> *n*-alkane flames. *Combust Flame* 2010;157:277–87.
- [32] Yates A, Bell A, Swarts A. Insights relating to the autoignition characteristics of alcohol fuels. *Fuel* 2010;89:83–93.
- [33] Liu W, Kelley AP, Law CK. Flame propagation and counterflow nonpremixed ignition of mixtures of methane and ethylene. *Combust Flame* 2010;157:1027–36.
- [34] Kopp M, Brower M, Mathieu O, Petersen E. CO<sub>2</sub> chemiluminescence study at low and elevated pressures. *Appl Phys B* 2012;107:529–38.
- [35] Kopp M, Mathieu O, Petersen EL. Rate determination of the CO<sub>2</sub> chemiluminescence reaction CO + O + M = CO<sub>2</sub> + M. *Int J Chem Kinet* 2015;47:50–72.
- [36] Nori VN, Seitzman JM. Chemiluminescence measurements and modeling in syngas, methane and jet-A fueled combustors. AIAA-2007-0466.
- [37] Chatelain K, Mevel R, Menon S, Blanquart G, Shepherd J. Ignition and chemical kinetics of acrolein-oxygen-argon mixtures behind reflected shock waves. *Fuel* 2014;135:498–508.
- [38] Nori VN, Seitzman JM. CH\* chemiluminescence modeling for combustion diagnostics. *Proc Combust Inst* 2009;32:895–903.
- [39] Hall JM, Petersen EL. An optimized kinetics model for OH chemiluminescence at high temperatures and atmospheric pressures. *Int J Chem Kinet* 2006;38:714–24.
- [40] Skeen SA, Manin J, Pickett LM. Simultaneous formaldehyde PLIF and high-speed schlieren imaging for ignition visualization in high-pressure spray flames. *Proc Combust Inst* 2015;35:3167–74.
- [41] Fu J, Tang C, Jin W, Thi LD, Huang Z, Zhang Y. Study on laminar flame speed and flame structure of syngas with varied compositions using OH-PLIF and spectrograph. *Int J Hydrogen Energy* 2013;38:1636–43.



# Ignition and extinction of strained nonpremixed cool flames at elevated pressures



Sili Deng<sup>1</sup>, Dong Han<sup>2</sup>, Chung K. Law<sup>\*</sup>

Department of Mechanical and Aerospace Engineering, Princeton University, Princeton, NJ 08544, USA

## ARTICLE INFO

### Article history:

Received 30 May 2016

Revised 20 October 2016

Accepted 21 October 2016

### Keywords:

Cool flame

Low-temperature chemistry

Ignition and extinction

Elevated pressure

Nonpremixed counterflow

## ABSTRACT

Cool flames, governed by low-temperature chemistry, are closely related to engine knock. Since the low-temperature chemical kinetics is promoted at elevated pressures, the ignition and extinction of nonpremixed cool flame at elevated pressures were experimentally and computationally investigated herein in the counterflow. Specifically, the hysteretic ignition and extinction behavior of the nonpremixed cool flame was for the first time observed and quantified. S-curve analysis was conducted to demonstrate the thermal and chemical structure of the cool flame and to elucidate the dominant chemical pathways during the ignition and extinction processes. The dominant low-temperature chemical reactions shift from those responsible for radical runaway to exothermic reactions that sustain the cool flame. Increasing the ambient pressure and/or the oxygen concentration in the oxidizer stream promote the heat release from the cool flame, and hence, result in an extended hysteresis temperature window between ignition and extinction. It is further noted that while the observed cool flame ignition temperatures were well predicted by computation, significant discrepancies existed for the extinction temperatures based on the well-adopted reaction mechanism used. Possible reasons were discussed to facilitate further cool flame studies and the development of the low-temperature chemistry.

© 2016 The Combustion Institute. Published by Elsevier Inc. All rights reserved.

## 1. Introduction

Cool flames, first reported in 1817 [1], are controlled by low-temperature chemical kinetics that have been extensively studied ever since [2]. Such low-temperature chemistry is ubiquitous for most large hydrocarbon fuels and has been shown to be related to the negative temperature coefficient (NTC) phenomenon observed in autoignition processes [3,4] and engine knocks [5]. The fundamental understanding of low-temperature chemistry and cool flame dynamics can also be important for combustion phasing control in the recent development of homogeneous charge compression ignition (HCCI) engines [6,7] and reactivity controlled compression ignition (RCCI) [8] engines.

Besides the potential utilization in engines, the dynamics of the cool flame are of fundamental interest. Cool flames and the NTC phenomena have been mostly observed in homogeneous systems

such as rapid compression machines [9–11], shock tubes [4,12,13], flow reactors [14,15] and stirred reactors [16,17]. Without the complexity of inhomogeneity and transport, low-temperature chemical kinetics can be studied in these systems for chemical model development. However, in practical combustors such as the diesel and gasoline direct injection (GDI) engines, combustion processes are governed by both transport and chemical kinetics. For such conditions, the characteristic mixing time scales can be comparable to the chemical reaction time scales, and the convective–diffusive processes may affect the initiation and sustenance of cool flames.

Recognizing that the inevitable presence of nonuniformities in practical combustion systems requires consideration of the coupled effects of chemistry and transport on cool flames, cool flames in nonpremixed systems have been recently studied in the counterflow [18–21] and microgravity droplet combustion [22–24]. In particular, Law and Zhao [18] and Zhao and Law [19] numerically investigated the nonpremixed counterflow cool flame of *n*-heptane, and identified the existence of a secondary S-curve dominated by low-temperature chemistry at low strain rates and/or high pressures. This secondary S-curve is grafted onto the lower branch of the primary S-curve and has its own ignition and extinction turning points. Experimentally, nonpremixed cool flames were observed in the counterflow at atmospheric pressure [20], including those employing a reactivity promoter [21,25]. The ignition

<sup>\*</sup> Corresponding author.

E-mail addresses: [silideng@stanford.edu](mailto:silideng@stanford.edu), [silideng@gmail.com](mailto:silideng@gmail.com) (S. Deng), [cklaw@princeton.edu](mailto:cklaw@princeton.edu) (C.K. Law).

<sup>1</sup> Current address: Department of Mechanical Engineering, Stanford University, Stanford, CA 94305, USA.

<sup>2</sup> Permanent address: Key Laboratory of Power Machinery and Engineering, Ministry of Education, Shanghai Jiao Tong University, Shanghai 200240, China.

temperature of dimethyl ether (DME) was quantified with infrared imaging [20], and was found to increase with increasing strain rate but was insensitive to the DME concentration in the fuel stream. In microgravity droplet combustion, it was found that the visible flame of large *n*-heptane, *n*-octane, and *n*-decane droplets could transit to a quasi-steady low-temperature burning mode after extinction of the hot flame due to radiation, suggesting the existence of steady droplet burning sustained by a cool flame [24].

Since low-temperature chemistry is more pronounced at elevated pressures, which for example could affect flame stabilization [26], we have conducted a systematic experimental and computational study on nonpremixed DME cool flames at elevated pressures. DME was chosen because it is an alternative diesel fuel that has low soot emissions due to its high cetane number and hydrogen-carbon ratio [27]. Moreover, there has been much development of DME chemical models with low-temperature chemistry that are also computationally affordable [28,29]. Furthermore, DME is a gaseous fuel, which does not require pre-vaporization and insulation in the experimentation. The first objective of the present study is to experimentally observe and quantify the ignition and extinction states of strained nonpremixed cool flames and hopefully to substantiate the computationally predicted ignition-extinction S-curve hysteresis. Upon such a validation, computation with detailed chemistry and transport are therefore able to elucidate the thermal and chemical structures of the cool flame and to demonstrate their evolution during the ignition and extinction processes. Finally, effects of the ambient pressure and oxygen concentration are investigated and compared between experiment and computation. Possible reasons for discrepancies in such comparisons are discussed to facilitate further studies.

## 2. Methodology

### 2.1. Experimental methodology

The ignition and extinction temperatures of DME nonpremixed cool flames were measured in the same counterflow system as that of Deng et al. [20], but at elevated pressures and different boundary conditions. Detailed descriptions of the experimental system are provided in [30,31]. Briefly, the counterflow facility consists of two symmetrical, vertically oriented, opposing quartz tubes with inner diameter of 2 cm and separated by 2 cm. A fuel stream consisting of 50% DME and 50% nitrogen at room temperature is issued from the lower nozzle and impinges onto the heated oxidizer stream from the upper nozzle. Both streams are shielded from the ambience by coflowing nitrogen streams. The exhaust valve of the chamber is adjusted to balance the inflow and outflow so as to maintain the desired chamber pressure.

A high-sensitivity monochrome CCD camera with high relative response in the UV spectrum (CCE-B013-U) was used to capture the global chemiluminescence from the low-temperature chemical reactions, which indicated the intensity of the cool flame [32]. The exposure time of the UV camera is the same 6 s for all cases. The ignition/extinction states of the cool flame were determined by gradually changing the oxidizer boundary temperature for a given fuel/oxidizer flow rate, until the chemiluminescence signal of the cool flame respectively emerged/disappeared as detected by the camera. The ignition and extinction temperatures were quantified with the corresponding oxidizer boundary temperatures measured with an uncoated K-type (Chromel-Alumel) thermocouple after radiation correction [30]. To measure the oxidizer temperature without the presence of cool flame, oxygen was replaced with nitrogen while the flow rates and heating power were kept the same.

The ignition and extinction states of the cool flames were studied at 2 and 3 atm ambient pressures, with the oxygen volume fraction in the oxidizer stream varied from 21% to 25%. The global

strain rate used in this study is defined as the pressure-weighted gradient of the axial flow velocity [33].

### 2.2. Computational methodology

The S-curve analysis [34], in which a system response such as the maximum temperature or maximum radical concentration is studied versus the variation of an imposed parameter, was adopted here to investigate the steady-state response of the counterflow reactive system subjected to the physical effects of flow strain or heat loss. The upper and lower turning points of the S-shaped response curve denote the system extinction and ignition states, respectively.

The S-curve analysis was conducted computationally. The governing equations for the counterflow flame computation are provided in [35]. *A posteriori* analysis based on the optically thin radiation model, with radiative properties based on the RADCAL model by Grosshandler of NIST [36] shows that the radiative heat loss is minimal, and therefore radiation is not included in the current computation. The damped Newton method and time integration solution scheme were adopted in a modified numerical code of Smooke et al. [37], solving the differential equations with boundary conditions specified on both sides of the potential flow. S-curve marching is conducted using a flame controlling method [38]. A skeletal DME mechanism [29], reduced from the detailed mechanism of Zhao et al. [28] with detailed transport properties, was used. Details about the reduction method and validation results against the full mechanism under a wide range of conditions were provided as supplementary material of that work.

In the computation, the nozzle separation distance was held at 2 cm to match the experimental system. The temperature and composition boundary conditions were consistent with the experiments. To generate the S-curve, the boundary temperature of the heated oxidizer stream was changed at a given strain rate. The critical ignition and extinction states of the cool flame were predicted based on the turning points of the secondary S-curve [18,20].

## 3. Results and discussion

In the following discussion, the experimental affirmation of the distinctive ignition and extinction behavior of cool flame is first demonstrated, and thereby validate the computational prediction. Furthermore, the thermal and chemical structures of the reacting layer in the counterflow at cool flame ignition, steady burning, and extinction conditions are demonstrated, elucidating the dominant chemical pathways for each condition. Finally, the effects of ambient pressure and oxygen concentration on ignition and extinction are discussed.

### 3.1. Hysteretic ignition and extinction behavior

What differentiates a strained cool flame from a reacting mixture going through slow oxidation in a heated flow is the hysteretic ignition and extinction behavior. Such hysteretic behavior is illustrated with an S-curve analysis shown in Fig. 1. Since the hot ignition of DME in the counterflow configuration has already been reported in the literature [39], only the cool flame portion of the S-curve is included. At a fixed strain rate, by gradually increasing the air boundary temperature and hence the reactivity and heat generation rate within the flow, at some point within the flow the temperature will exceed the boundary temperature and eventually lead to self-sustained burning. Such a transition state I is defined as the ignition point, and the condition after ignition that is located on the upper steady branch of the S-curve is designated as point S, representing a steady cool flame. The difference in the maximum temperatures between points S and I primarily

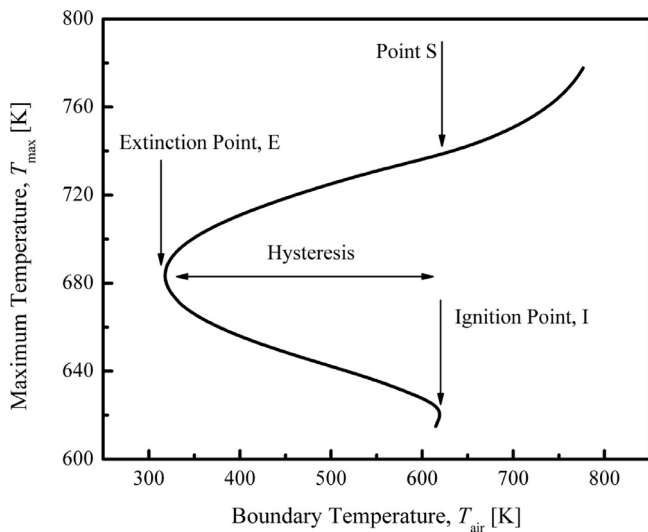


**Fig. 1.** S-Curve analysis of the response of nonpremixed counterflow of 50% DME and 50% nitrogen versus heated air at the 2 atm and pressure-weighted strain rate of  $80 \text{ s}^{-1}$ .

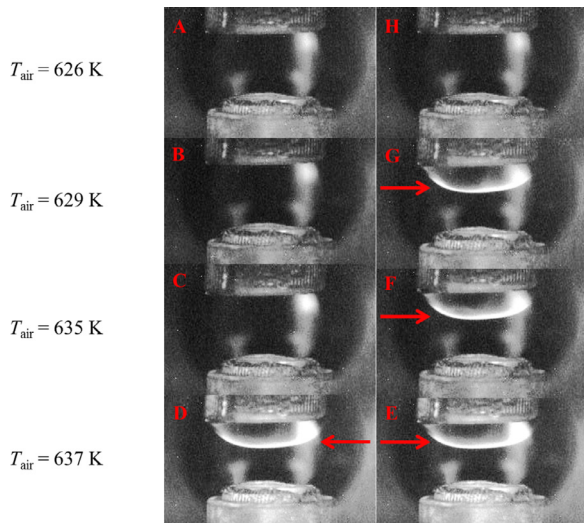


**Fig. 2.** Flame images demonstrating the hysteretic nature of ignition and extinction of cool flames with air temperature. DME cool flame at 2 atm and pressure-weighted strain rate of  $84 \text{ s}^{-1}$ ; DME volume fraction in the fuel stream is 50%, and the oxidizer stream is air.

results from the heat release from the cool flame. As this temperature decreases from point S, the maximum temperature in the flow field also decreases, following the upper branch trajectory, until the flame extinguishes at point E. The difference in the air boundary temperature between points I (or S) and E demonstrates the hysteresis between the ignition and extinction of the flame.

To capture this computationally predicted hysteresis, the ignition and extinction temperatures were experimentally measured in the counterflow based on the chemiluminescence of the cool flame. Figure 2 shows representative images of the ignition and extinction detection for the DME/air cool flame at 2 atm and pressure-weighted strain rate of  $84 \text{ s}^{-1}$ . Ignition of the cool flame is achieved by gradually increasing the oxidizer boundary temperature. As shown in the left column of Fig. 2, when the oxidizer boundary temperature is slowly increased from 626 K to 637 K (A–D), the chemiluminescence from the low-temperature chemistry suddenly becomes detectable by the UV camera, indicating onset of the cool flame. The oxidizer boundary temperature is

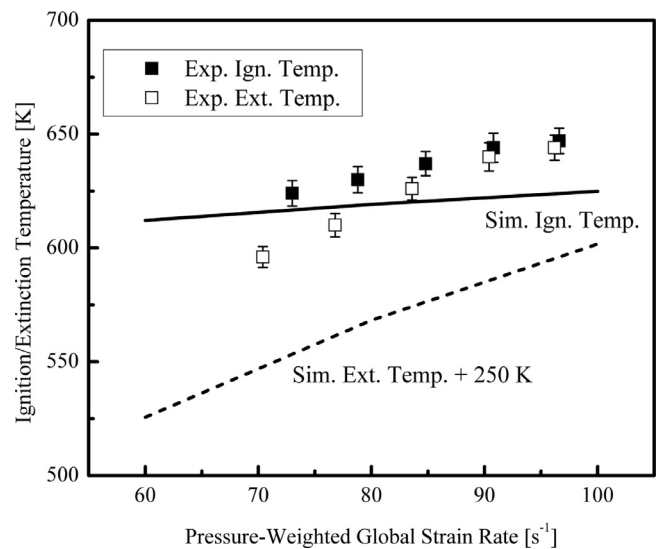


**Fig. 3.** Experimental and computed ignition and extinction temperatures at 2 atm and various strain rates. The computed extinction temperature is shifted up by 250 K for better illustration. DME volume fraction in the fuel stream is 50%, and the oxidizer stream is air.

then gradually reduced with a temperature interval of 1 K, while maintaining quasi-steadiness at each step. The right column of Fig. 2 then shows that although the cool flame chemiluminescence remains as the boundary temperature is decreased from 637 K to 626 K (E to H), it suddenly vanishes at 626 K, which was thus defined as the extinction temperature.

The same procedure was followed to obtain the ignition and extinction temperatures at various strain rates for comparisons with the computationally predicted values, as shown in Fig. 3. Results from experiment and computation then both show that the ignition and extinction temperatures increase with increasing strain rate, due to reduced residence time. Furthermore, the ignition temperature not only is higher than the extinction temperature at a given strain rate, it is also less sensitive to the strain rate, resulting in a less pronounced ignition-extinction hysteresis. Noting that the repeatability of the measurement is within 2 K, which is within the marker size in the figure, and the error bar represents the uncertainty of the radiation correction using different models, comparison between the experimental data should be made based on the upper or lower bound of the uncertainty bar across all the measurements.

It is also apparent from Fig. 3 that while the experimental and computational results separately exhibit the anticipated physics, namely the extinction temperature is lower than the ignition temperature, and they both increase with increasing strain rate, the quantitative comparison between them is overall poor, both in magnitude as well as the strain-rate sensitivity. We shall defer the detailed analysis of these discrepancies to Section 3.3.

### 3.2. Analysis of thermal and chemical structures

In order to elucidate the dominant chemical pathways and evolution of the ignition and extinction processes, the three characteristic points on the S-curve of Fig. 1, which respectively represent the states prior to ignition (point I), steady burning (point S), and prior to extinction (point E), were chosen for structural analysis.

As shown in Fig. 4, the heat release just prior to the initiation of the cool flame is negligible, and the maximum temperature in the flow field is set by the oxidizer boundary. For both steady flames at points S and E, there are reaction kernels delineated by the heat release profiles. Based on the full width at half

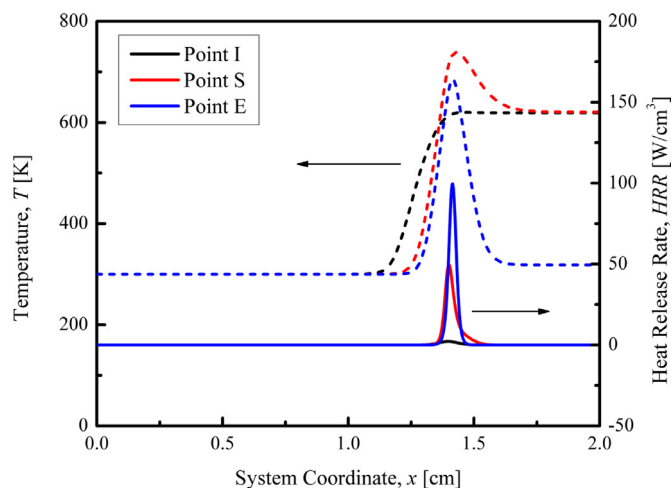


**Fig. 4.** Thermal structures in the computed flow field at three representative points on the S-curve shown in Fig. 1. The solid lines refer to heat release rate, while the dashed lines refer to temperature. Fuel stream boundary conditions are specified at  $x = 0$  in the computation.

maximum of the heat release profile, a typical cool flame thickness is about 0.05 cm for the present conditions. At point E, the heat release rate of the cool flame is higher than that at point S, for low-temperature chemistry is favored at relatively lower temperatures. However, the steep gradient of the heat release profile indicates that heat loss due to strain at point E is more pronounced compared to point S. As the boundary temperature further decreases, such heat loss increases, and chemical reactions cannot keep up with heat loss from the reaction zone, leading to extinction due to the limited residence time in the strained flow.

The profiles of three representative species, namely methoxymethylperoxy ( $\text{CH}_3\text{OCH}_2\text{O}_2$ ), formaldehyde ( $\text{CH}_2\text{O}$ ), and hydroxyl ( $\text{OH}$ ), were then investigated to elucidate the chemical structures at these three points, I, S, and E, as shown in Fig. 5. The methoxymethylperoxy radical was chosen because it is a representative species for the low-temperature chemistry [40,41]. Comparing the species profiles of the three states, it is seen that the  $\text{CH}_3\text{OCH}_2\text{O}_2$  mass fraction increases upon flame initiation, and similar to the heat release rate profile, its peak increases as extinction is approached. Moreover, the profile broadens for low-temperature chemistry is favored at reduced oxidizer boundary temperature. Formaldehyde was selected because it is a major product of the cool flame, with its intensity manifested through its chemiluminescence [32]. It is then seen that: negligible  $\text{CH}_2\text{O}$  is formed prior to ignition; significant amount is formed in the steady flame; and the concentration and hence the intensity of chemiluminescence is reduced as extinction is approached. Finally, the hydroxyl radical was chosen because it represents high-temperature flame chemistry and is also an important radical formed during the chain branching reactions of the low-temperature chemistry. It is then noted that the peak mass fraction of  $\text{OH}$  is several orders of magnitude smaller than those in a typical hot flame [41]. The ignition of cool flame is initiated with a peak formation of  $\text{OH}$ , which subsequently decreases upon ignition. With subsequent heat release from the cool flame, a second peak of  $\text{OH}$  mass fraction emerges on the oxidizer side of the cool flame peak, which is responsible for the initiation of the hot flame at higher boundary temperatures [18].

Finally, sensitivity analysis was conducted to elucidate the evolution of the dominant chemical pathways during the ignition and extinction processes. The maximum temperature was chosen as the target for sensitivity analysis, and the ratio of the relative change of the maximum temperature to that of the Arrhenius

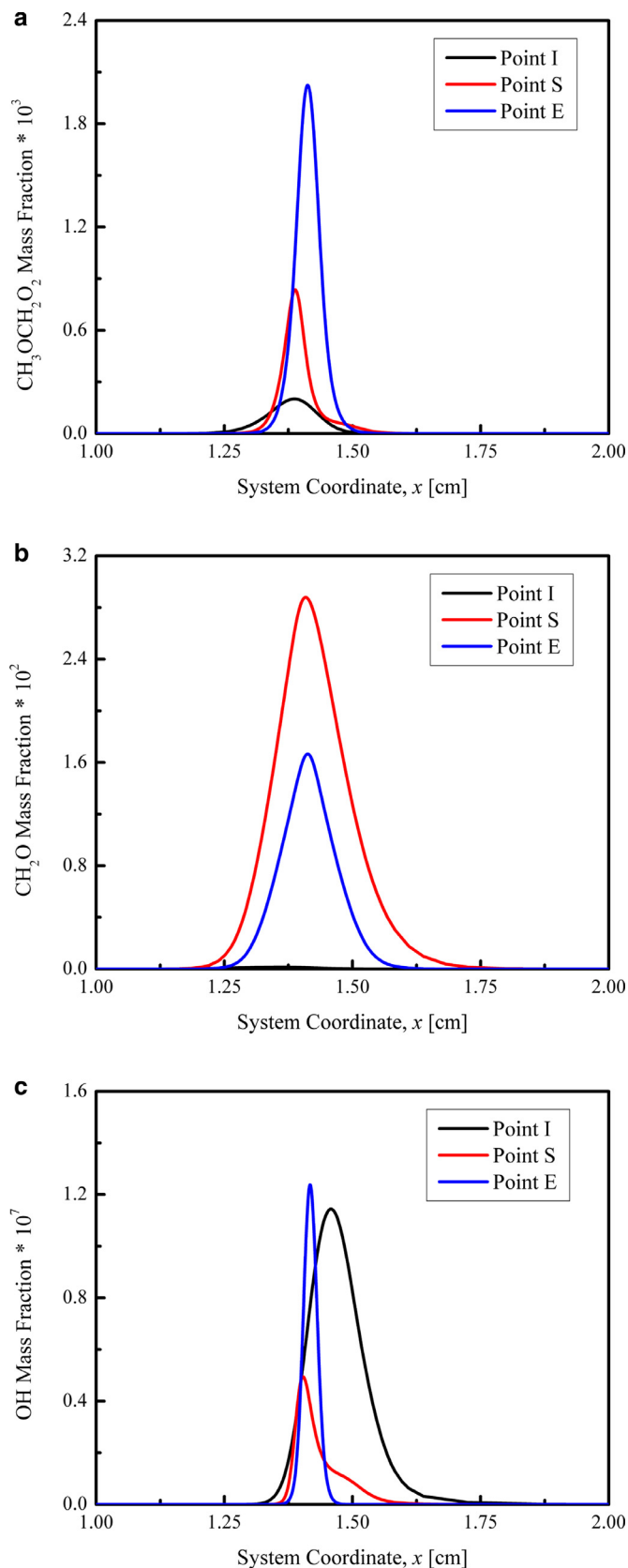


**Fig. 5.** (a) Methoxymethylperoxy radical, (b) formaldehyde, and (c) hydroxyl radical profiles in the computed flow field at three representative points on the S-curve shown in Fig. 1. Fuel stream boundary conditions are specified at  $x = 0$  in the computation.

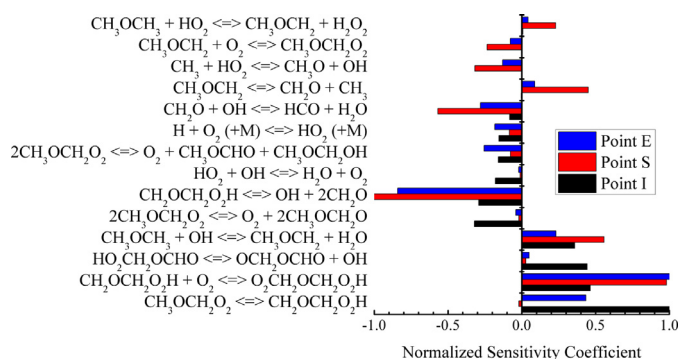


Fig. 6. Reaction sensitivity analysis at three representative points on the S-curve shown in Fig. 1.

factor of each reaction being perturbed was defined as the sensitivity coefficient. The sensitivity coefficients of all the reactions considered in the chemical mechanism were normalized by the maximum value such that the normalized sensitivity coefficient is bounded by  $-1$  and  $1$  to allow for comparisons between the cases.

The normalized sensitivity coefficients ranked by their absolute values for states I, S, and E in Fig. 1 are shown in Fig. 6. At all three states, low-temperature chemistry is dominant, with the absence of the typical high-temperature chain branching reactions such as  $\text{H} + \text{O}_2 \rightleftharpoons \text{OH} + \text{O}$ . Similar to the ignition analysis in Deng et al. [20], the isomerization reaction  $\text{CH}_3\text{OCH}_2\text{O}_2 \rightleftharpoons \text{CH}_2\text{OCH}_2\text{O}_2\text{H}$  and the oxygen addition reaction  $\text{CH}_2\text{OCH}_2\text{O}_2\text{H} + \text{O}_2 \rightleftharpoons \text{O}_2\text{CH}_2\text{OCH}_2\text{O}_2\text{H}$  promote ignition, while the reaction  $\text{CH}_2\text{OCH}_2\text{O}_2\text{H} \rightleftharpoons \text{OH} + 2\text{CH}_2\text{O}$  retards it. The species profiles demonstrated in Fig. 5 also support such findings, for the mass fraction of  $\text{CH}_3\text{OCH}_2\text{O}_2$  for the extinction state E is higher than that for the steady state S, while the opposite trend is observed for  $\text{CH}_2\text{O}$ . Near the extinction state E, low-temperature chemistry is favored as the boundary temperature decreases, and therefore, more  $\text{CH}_3\text{OCH}_2\text{O}_2$  and less  $\text{CH}_2\text{O}$  is formed. However, for the steady cool flames corresponding to points S and E, the relative importance of these reactions shifts. First,  $\text{CH}_2\text{OCH}_2\text{O}_2\text{H} + \text{O}_2 \rightleftharpoons \text{O}_2\text{CH}_2\text{OCH}_2\text{O}_2\text{H}$  becomes even more important in steady cool flames. Since the maximum temperature was chosen as the target to evaluate the sensitivity, the exothermic reaction  $\text{CH}_2\text{OCH}_2\text{O}_2\text{H} + \text{O}_2 \rightleftharpoons \text{O}_2\text{CH}_2\text{OCH}_2\text{O}_2\text{H}$  demonstrates a large positive sensitivity coefficient. Conversely, at ignition, reactions that finally lead to radical runaway are more important, for heat release from the mixing layer is negligible at this state, as shown in Fig. 4. Second, the isomerization reaction  $\text{CH}_3\text{OCH}_2\text{O}_2 \rightleftharpoons \text{CH}_2\text{OCH}_2\text{O}_2\text{H}$  becomes important again near extinction, for, at extinction, the radical production rates barely keep up with the transport losses and the chain carrying limiting step becomes crucial again.

### 3.3. Uncertainty analysis

As noted in Fig. 3, while the computation is able to capture the experimental observation of the hysteretic feature of ignition and extinction, as well as the increasing trend of ignition and extinction temperatures with increasing strain rate, the quantitative agreement is rather poor. Specifically, the ignition temperature is slightly overpredicted; its sensitivity to strain rate, indicated by the slope of the ignition temperature profile, is substantially underpredicted; and, most importantly, the extinction temperature is significantly underpredicted. Upon extensive exploration of the various experimental and modeling factors that could contribute to such substantial disagreements, the uncertainty of the low-temperature chemistry used in the computation has surfaced to be the dominant factor.

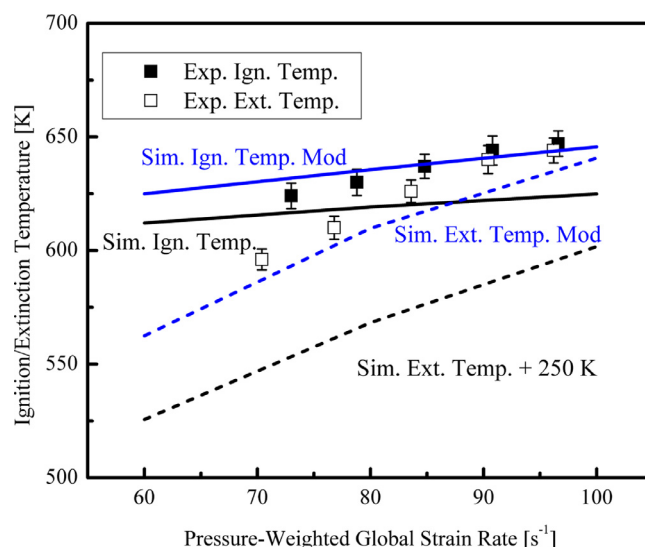
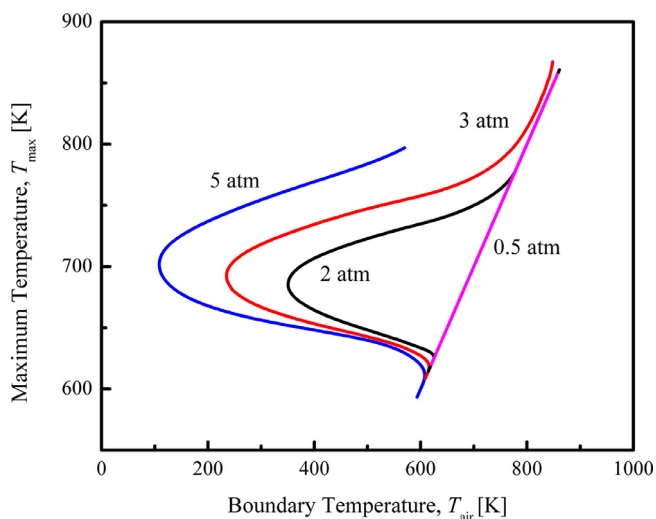


Fig. 7. Revisit of Fig. 3 with modified reaction rates in the chemical mechanism. Note that the line plots with the modified reaction rates are presented without shifting.

To demonstrate the effects of such uncertainty and since the ignition temperatures of the cool flames are fairly well captured, it is reasonable to inspect reactions with large sensitivity coefficients in Fig. 6 for the cool flames. This leads to the identification of the reactions:  $\text{CH}_2\text{OCH}_2\text{O}_2\text{H} + \text{O}_2 \rightleftharpoons \text{O}_2\text{CH}_2\text{OCH}_2\text{O}_2\text{H}$  and  $\text{CH}_2\text{OCH}_2\text{O}_2\text{H} \rightleftharpoons \text{OH} + 2\text{CH}_2\text{O}$ . Since cool flames appear to be more robust to extinguish, we have repeated the calculation by modifying the preexponential factors of these two reactions by respectively reducing and increasing to 70% and 200% of their original values.

Figure 7 then shows that both qualitative and quantitative agreements between experiments and computations are achieved with the modified reaction parameters. Specifically, although the magnitude of the ignition temperature is not very sensitive to the modifications, as expected, its sensitivity to increasing strain rate is enhanced, for the modifications essentially slow down the low-temperature chemistry such that the sensitivity to finite residence time is more pronounced. More importantly, it is seen that good agreement is also achieved for the highly sensitive extinction temperatures, significantly boosting their values but without changing the sensitivity to the strain rate variation.

While the above results appear to be encouraging, we hasten to clarify that we are not suggesting modified kinetic parameters for certain reactions. What we have demonstrated is the sensitive nature and potential uncertainty of the low-temperature chemistry, in that substantial change in the global response can result from even small changes in these preexponential factors. It is noted that while the Zhao et al. model, based on which the adopted skeletal model was developed, was still the most well accepted, additional experimental data have become available recently to guide the modification of the low-temperature chemical pathways and kinetic parameters [42,43]. It is nevertheless also noted that, during the development of the low-temperature chemical model, the validation data is limited to those from homogeneous systems. The current study aims at providing validation targets in inhomogeneous systems by substantiating the existence of the nonpremixed cool flame and revealing the evolution of low-temperature chemistry during the ignition and extinction processes. Clearly, additional validation data on cool flames covering a wider range of conditions, which are inherently present in flame systems, is needed.



**Fig. 8.** S-curve analysis for various ambient pressures and pressure-weighted strain rate of  $100 \text{ s}^{-1}$ . DME volume fraction in the fuel stream is 50%, and the oxidizer stream is air.

Another factor that could potentially affect the accuracy of the comparison between the experimental and computational results is the experimental detection limit of the UV camera, which could be too high compared to the chemiluminescence emission of the cool flame near extinction. Since the hysteresis temperature window was observed in the experiment at various conditions, the detection threshold of the UV camera should be lower than the chemiluminescence intensity of the steady cool flame upon ignition. Consequently, the ignition temperatures for these cases should be well captured. However, the lower bound of the hysteresis temperature window could be limited by the detection threshold, and therefore, the actual extinction temperatures might not be captured accurately.

It is further noted that Shan and Lu conducted a computational study on the ignition and extinction of DME/air mixtures at high pressures in a perfectly stirred reactor (PSR) [44]. In their work, eigen-analysis of the chemical Jacobian matrix was performed, and physically unstable segments were observed on the branches of an S-curve for DME/air corresponding to both strong and cool flames. Oscillations were observed in the simulation for the unstable cases under perturbation. In the present experiments, such oscillations were not observed when extinction occurred even in the presence of unavoidable system perturbations such as fluctuations from the heat supply and flow meters, with the repeatability of ignition and extinction temperature measurements within 2 K, as indicated in Section 3.1. Consequently, oscillation was not observed when extinction occurred in the current study. Therefore, we do not expect that the large discrepancy between the current experimental and computational cool flame extinction results is due to the instability of the cool flame.

### 3.4. Effects of pressure and oxygen concentration

The effects of ambient pressure and oxygen concentration in the oxidizer stream on the ignition and extinction of the cool flames were also investigated. Pressure effects were first computationally studied by fixing the oxygen mole fraction in the oxidizer stream at 21% and fixing the pressure-weighted strain rate at  $100 \text{ s}^{-1}$ , as shown in Fig. 8. It is seen that, as the pressure increases from 2 to 5 atm, the ignition temperature decreases and the heat release from the cool flame becomes more pronounced, as indicated by the temperature differences between the ignition turning point and the point on the cool flame branch with

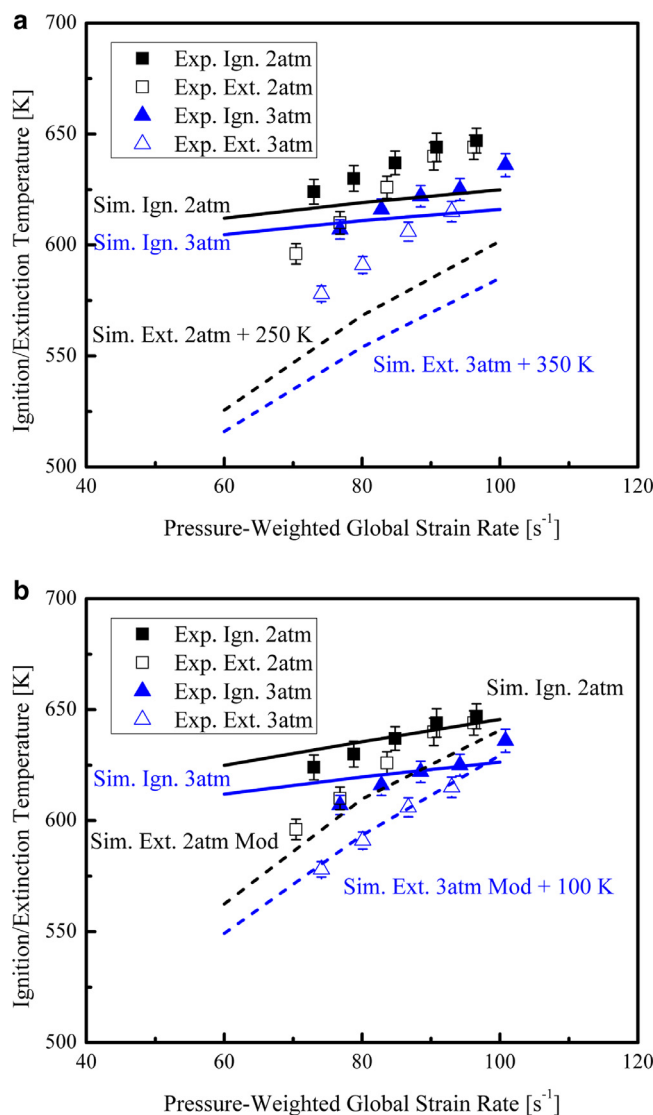


**Fig. 9.** Ignition and extinction temperatures at various strain rates and pressures in experiments and computations with (a) the original and (b) modified chemical models. Some of the computed extinction temperatures are shifted up for better illustration. DME volume fraction in the fuel stream is 50%, and the oxidizer stream is air.

the same boundary temperature. Moreover, the extinction turning point shifts to a lower boundary temperature, resulting in an extended hysteresis temperature window. Conversely, the extent of the low-temperature chemistry governed S-curve hysteresis diminishes with decreasing pressure, leading to its absence at 0.5 atm.

The conclusion that elevated pressure promotes low-temperature chemistry is consistent with previous studies with *n*-heptane [4,18] and more generally discussed in Pilling's book [45]. Such promotion effect can be explained with the sensitivity analysis in Section 3.2. Qualitatively, sensitivity analysis conducted for elevated pressures shows similar dominant chemical pathways as Fig. 6. At elevated pressures, the balance of the reaction  $\text{CH}_2\text{OCH}_2\text{O}_2\text{H} + \text{O}_2 \rightleftharpoons \text{O}_2\text{CH}_2\text{OCH}_2\text{O}_2\text{H}$  shifts forward and promotes the formation of the important intermediate radicals for low-temperature chemistry. Moreover, the  $\text{CH}_2\text{OCH}_2\text{O}_2\text{H} \rightleftharpoons \text{OH} + 2\text{CH}_2\text{O}$  reaction is retarded at elevated pressures.

Figure 9 further shows that the experimental ignition and extinction temperatures decrease at elevated pressures. It is seen

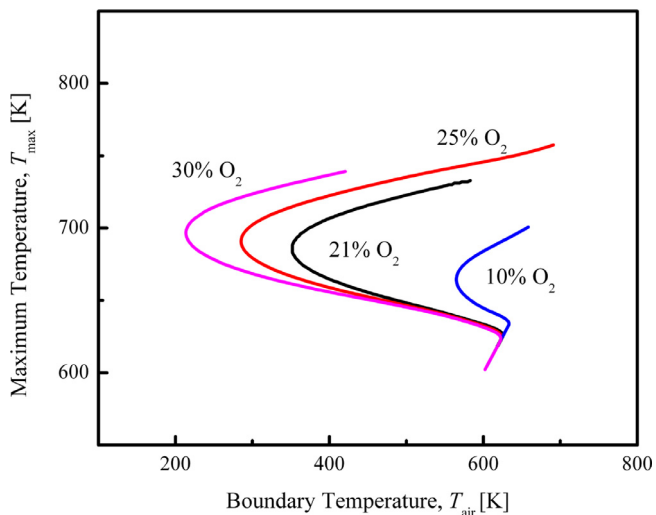


**Fig. 10.** S-curve analysis for various oxygen concentrations and the pressure-weighted strain rate of  $100 \text{ s}^{-1}$ . DME volume fraction in the fuel stream is 50%, and the ambient pressure is 2 atm.

that, while the effects of elevated pressure on ignition temperatures are predicted by computations qualitatively, the effects on extinction temperatures are significantly overpredicted when using the original mechanism (Fig. 9a). The comparison is improved by using the two modified reactions (Fig. 9b), although the degree of improvement is less satisfactory as for the case of 2 atm pressure, shown in Fig. 7. We emphasize again that we prefer leaving the comparison as is, without further tuning the reactions as we do not believe it is justified within the scope of the present study.

Figure 10 shows that increasing the oxygen concentration extends the hysteresis temperature window of the cool flame at the same ambient pressure and strain rate, while the ignition temperature is almost unaffected except at very low concentrations. This is because, with increased oxygen concentration and hence decreased inert concentration, the heat release from the cool flame becomes more pronounced, which results in decreased extinction temperature. Dominant chemical pathways for these conditions are similar to those in Fig. 6.

The insensitivity of the cool flame ignition temperature is further confirmed with the experimental measurements, as shown in Fig. 11a. However, the reduction effect of increased oxygen concentration on the cool flame extinction temperature is again overpredicted by the computation, while improved agreements are achieved with the two modified preexponential factors (Fig. 11b).

#### 4. Conclusions

The ignition and extinction of nonpremixed DME/air cool flames at elevated pressures were experimentally and computationally investigated in the counterflow. For the first time, the hysteretic ignition and extinction behavior of the nonpremixed cool flame was experimentally observed and quantified. Results further show that although low-temperature chemistry is crucial for the initiation and sustain of the cool flame, the dominant chemical pathways shift from reactions responsible for low-temperature radical runaway to cool flame heat release reactions upon ignition. The heat release from the cool flame is able to sustain itself at lower oxidizer boundary temperature, and, therefore, results in the hysteresis temperature window between ignition and extinction.

Increasing ambient pressure and/or oxygen concentration in the oxidizer stream promotes the heat release from low-temperature chemistry and extends the hysteresis between ignition and

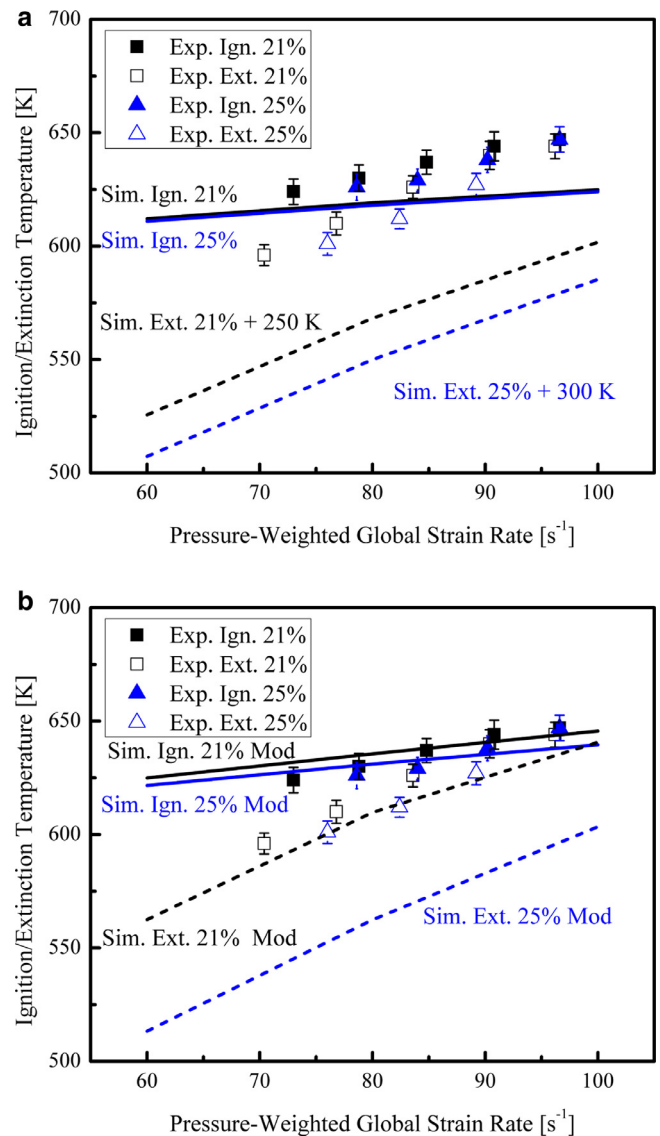


**Fig. 11.** Ignition and extinction temperatures at various strain rates and oxygen concentrations in experiments and computations with (a) the original and (b) modified chemical models. Some of the computed extinction temperatures are shifted up for better illustration. DME volume fraction in the fuel stream is 50%, and the ambient pressure is 2 atm.

extinction. Although the influences on the cool flame ignition temperature were well predicted by computation, the influences on extinction were significantly overpredicted. Possible reasons for such discrepancies were discussed, including the uncertainties from experiments and chemical models. The need for improved comprehensiveness of the chemical kinetics model is emphasized.

#### Acknowledgments

This work was supported in part by the Air Force Office of Scientific Research under the technical monitoring of Dr. Mitat Birkan, and the Combustion Energy Frontier Research Center, an Energy Frontier Research Center funded by the US Department of Energy, Office of Basic Energy Sciences under Award Number DE-SC0001198. Dong Han acknowledges the support from the China Postdoctoral Council via the International Postdoctoral Exchange Fellowship Program.

## References

- [1] H. Davy, Some new experiments and observations on the combustion of gaseous mixtures, with an account of a method of preserving a continued light in mixtures of inflammable gases and air without flame, *Philos. Trans. R. Soc. Lond.* 107 (1817) 77–86.
- [2] J.F. Griffiths, S.K. Scott, Thermokinetic interactions: fundamentals of spontaneous ignition and cool flames, *Prog. Energy Combust. Sci.* 13 (1987) 161–197.
- [3] W. Leppard, The chemical origin of fuel octane sensitivity, SAE Technical Paper 902137, SAE, 1990.
- [4] H.K. Ciezki, G. Adomeit, Shock-tube investigation of self-ignition of *n*-heptane–air mixtures under engine relevant conditions, *Combust. Flame* 93 (4) (1993) 421–433.
- [5] J.F. Griffiths, J.P. MacNamara, C.G.W. Sheppard, D.A. Turton, B.J. Whitaker, The relationship of knock during controlled autoignition to temperature inhomogeneities and fuel reactivity, *Fuel* 81 (2002) 2219–2225.
- [6] S. Kong, C. Marriott, R. Reitz, M. Christensen, Modeling and experiments of HCCI engine combustion using detailed chemical kinetics with multidimensional CFD, SAE Technical Paper 2001-01-1026, SAE, 2001.
- [7] X. Lu, D. Han, Z. Huang, Fuel design and management for the control of advanced compression-ignition combustion modes, *Prog. Energy Combust. Sci.* 37 (2011) 741–783.
- [8] S.L. Kokjohn, R.M. Hanson, D.A. Splitter, R.D. Reitz, Fuel reactivity controlled compression ignition (RCI): a pathway to controlled high-efficiency clean combustion, *Int. J. Engine Res.* 12 (2011) 209–226.
- [9] J.F. Griffiths, J.P. MacNamara, C.G.W. Sheppard, D.A. Turton, B.J. Whitaker, The relationship of knock during controlled autoignition to temperature inhomogeneities and fuel reactivity, *Fuel* 81 (2002) 2219–2225.
- [10] E.J. Silke, H.J. Curran, J.M. Simmie, The influence of fuel structure on combustion as demonstrated by the isomers of heptane: a rapid compression machine study, *Proc. Combust. Inst.* 30 (2005) 2639–2647.
- [11] H. Di, X. He, P. Zhang, Z. Wang, M.S. Wooldridge, C.K. Law, C. Wang, S. Shuai, J. Wang, Effects of buffer gas composition on low temperature ignition of iso-octane and *n*-heptane, *Combust. Flame* 161 (2014) 2531–2538.
- [12] S.S. Vasu, D.F. Davidson, R.K. Hanson, Jet fuel ignition delay times: shock tube experiments over wide conditions and surrogate model predictions, *Combust. Flame* 152 (2008) 125–143.
- [13] J. Herzler, L. Jerig, P. Roth, Shock tube study of the ignition of lean *n*-heptane/air mixtures at intermediate temperatures and high pressures, *Proc. Combust. Inst.* 30 (2005) 1147–1153.
- [14] D.N. Koert, D.L. Miller, N.P. Cernansky, Experimental studies of propane oxidation through the negative temperature coefficient region at 10 and 15 atmospheres, *Combust. Flame* 96 (1994) 34–49.
- [15] H.J. Curran, S.L. Fischer, F.L. Dryer, Reaction kinetics of dimethyl ether. II. Low-temperature oxidation in flow reactors, *Int. J. Chem. Kinet.* 32 (12) (2000) 741–759.
- [16] P. Dagaut, M. Reuillon, M. Cathonnet, Experimental study of the oxidation of *n*-heptane in a jet stirred reactor from low to high temperature and pressures up to 40 atm, *Combust. Flame* 101 (1995) 132–140.
- [17] S. Kikui, T. Kamada, H. Nakamura, T. Tezuka, S. Hasegawa, K. Maruta, Characteristics of *n*-butane weak flames at elevated pressures in a micro flow reactor with a controlled temperature profile, *Proc. Combust. Inst.* 35 (2015) 3405–3412.
- [18] C.K. Law, P. Zhao, NTC-affected ignition in nonpremixed counterflow, *Combust. Flame* 159 (3) (2012) 1044–1054.
- [19] P. Zhao, C.K. Law, The role of global and detailed kinetics in the first-stage ignition delay in NTC-affected phenomena, *Combust. Flame* 160 (11) (2013) 2352–2358.
- [20] S. Deng, P. Zhao, D. Zhu, C.K. Law, NTC-affected ignition and low-temperature flames in nonpremixed DME/air counterflow, *Combust. Flame* 161 (8) (2014) 1993–1997, doi:10.1016/j.combustflame.2014.01.020.
- [21] S.H. Won, B. Jiang, P. Dievart, C.H. Sohn, Y. Ju, Self-sustaining *n*-heptane cool diffusion flames activated by ozone, *Proc. Combust. Inst.* 35 (2015) 881–888.
- [22] V. Nayagam, D.L. Dietrich, P.V. Ferkul, M.C. Hicks, F.A. Williams, Can cool flames support quasi-steady alkane droplet burning? *Combust. Flame* 159 (2012) 3583–3588.
- [23] T.I. Farouk, M.C. Hicks, F.L. Dryer, Multistage oscillatory “cool flame” behavior for isolated alkane droplet-combustion in elevated pressure microgravity condition, *Proc. Combust. Inst.* 35 (2015) 1701–1708.
- [24] V. Nayagam, D.L. Dietrich, M.C. Hicks, F.A. Williams, Cool-flame extinction during *n*-alkane droplet combustion in microgravity, *Combust. Flame* 162 (2015) 2140–2147.
- [25] Y. Ju, J.K. Lefkowitz, C.B. Reuter, S.H. Won, X. Yang, S. Yang, W. Sun, Z. Jiang, Q. Chen, Plasma assisted low temperature combustion, *Plasma Chem. Plasma Process* 36 (2016) 85–105.
- [26] S. Deng, P. Zhao, M.E. Mueller, C.K. Law, Flame dynamics in oscillating flows under autoignitive conditions, *Combust. Flame* 168 (2016) 75–82.
- [27] A. McIlroy, T.D. Hain, H.A. Michelsen, T.A. Cool, A laser and molecular beam mass spectrometer study of low-pressure dimethyl ether flames, *Proc. Combust. Inst.* 28 (2000) 1647–1653.
- [28] Z. Zhao, M. Chaos, A. Kazakov, F.L. Dryer, Thermal decomposition reaction and a comprehensive kinetic model of dimethyl ether, *Int. J. Chem. Kinet.* 40 (1) (2008) 1–18.
- [29] A. Bhagatwala, Z. Luo, H. Shen, J.A. Sutton, T. Lu, J.H. Chen, Numerical and experimental investigation of turbulent DME jet flames, *Proc. Combust. Inst.* 35 (2015) 1157–1166.
- [30] C.G. Fotache, T.G. Kreutz, D.L. Zhu, C.K. Law, An experimental study of ignition in nonpremixed counterflowing hydrogen versus heated air, *Combust. Sci. Technol.* 109 (1995) 373–393, doi:10.1080/00102209508951910.
- [31] W. Liu, D. Zhu, N. Wu, C.K. Law, Ignition of *n*-heptane pool by heated stagnating oxidizing flow, *Combust. Flame* 157 (2010) 259–266.
- [32] P. Zhao, W. Liang, S. Deng, C.K. Law, Initiation and propagation of laminar premixed cool flames, *Fuel* 166 (2016) 477–487.
- [33] R. Seiser, H. Pitsch, K. Seshadri, W.J. Pitz, H.J. Curran, Extinction and autoignition of *n*-heptane in counterflow configuration, *Proc. Combust. Inst.* 28 (2000) 2029–2037.
- [34] C.K. Law, *Combustion physics*, Cambridge University Press, New York, 2006.
- [35] V. Giovangigli, M.D. Smooke, Calculation of extinction limits for premixed laminar flames in a stagnation point flow, *J. Comput. Phys.* 68 (2) (1987) 327–345, doi:10.1016/0021-9991(87)90061-1.
- [36] W.L. Grosshandler, RADCAL: a narrow-band model for radiation calculations in a combustion environment, NIST Technical Note 1402, NIST, 1993.
- [37] M.D. Smooke, I.K. Puri, K. Seshadri, A comparison between numerical calculations and experimental measurements of the structure of a counterflow diffusion flame burning diluted methane in diluted air, *Symp. (Int.) Combust.* 21 (1988) 1783–1792.
- [38] M. Nishioka, C.K. Law, T. Takeno, A flame-controlling continuation method for generating S-curve responses with detailed chemistry, *Combust. Flame* 104 (1996) 328–342.
- [39] X.L. Zheng, T.F. Lu, C.K. Law, C.K. Westbrook, H.J. Curran, T. Berces, F.L. Dryer, Experimental and computational study of nonpremixed ignition of dimethyl ether in counterflow, *Proc. Combust. Inst.* 30 (2005) 1101–1109.
- [40] S. Deng, P. Zhao, M.E. Mueller, C.K. Law, Autoignition-affected stabilization of laminar nonpremixed DME/air coflow flames, *Combust. Flame* 162 (2015a) 3437–3445.
- [41] S. Deng, P. Zhao, M.E. Mueller, C.K. Law, Stabilization of laminar nonpremixed DME/air coflow flames at elevated temperatures and pressures, *Combust. Flame* 162 (2015b) 4471–4478.
- [42] U. Burke, K.P. Somers, P. O’Toole, C.M. Zinner, N. Marquet, G. Bourque, E.L. Petersen, W.K. Metcalfe, Z. Serinyel, H.J. Curran, An ignition delay and kinetic modeling study of methane, dimethyl ether, and their mixtures at high pressures, *Combust. Flame* 162 (2015) 315–330.
- [43] A. Rodriguez, O. Frottier, O. Herbinet, R. Fournet, R. Bounaceur, C. Fittschen, F. Battin-Leclerc, Experimental and modeling investigation of the low-temperature oxidation of dimethyl ether, *J. Phys. Chem. A* 119 (2015) 7905–7923.
- [44] R. Shan, T. Lu, Ignition and extinction in perfectly stirred reactors with detailed chemistry, *Combust. Flame* 159 (2012) 2069–2076.
- [45] M.J. Pilling, *Low-temperature combustion and autoignition*, Elsevier Science, 1997.

# AFOSR Deliverables Submission Survey

Response ID:7409 Data

1.

**Report Type**

Final Report

**Primary Contact Email**

Contact email if there is a problem with the report.

cklaw@princeton.edu

**Primary Contact Phone Number**

Contact phone number if there is a problem with the report

6092585271

**Organization / Institution name**

Princeton University

**Grant/Contract Title**

The full title of the funded effort.

Flame Dynamics and Chemistry in LRE Combustion Instability

**Grant/Contract Number**

AFOSR assigned control number. It must begin with "FA9550" or "F49620" or "FA2386".

FA9550-15-1-0338

**Principal Investigator Name**

The full name of the principal investigator on the grant or contract.

Chung K. Law

**Program Officer**

The AFOSR Program Officer currently assigned to the award

Mitat Birkan

**Reporting Period Start Date**

09/01/2015

**Reporting Period End Date**

08/31/2016

**Abstract**

Nonpremixed jet flames have been extensively studied to understand the combustion processes in rocket engines. The stabilization and structure of jet flames determine the lift-off height of the flame and are therefore integral to engine design. In view of the nonpremixed nature of the fuel and oxidizer jets, stabilization can be achieved through either auto-ignition or the so-called tribrachial flame, in which a lean and a rich premixed flame wing with a trailing diffusion flame branch. The point where the three branches intersect, the triple point, is considered to be the stabilization point. Regardless of the mechanisms, assessment of flame stabilization must necessarily include the simultaneous and coupled considerations of the fluid flow in the combustion chamber, the mixing between the fuel and oxidizer jets, and the chemistry and dynamics either of the mixing layer or of the flame. The research has been conducted along two thrusts, namely: (1) the dynamics of flame stabilization in environments of various thermodynamic and dynamics characterizations, and (2) the chemistry and dynamics of strained flames, particularly those involving the cool flame, NTC (negative temperature coefficient) chemistry, noting that interests in cool flame chemistry and dynamics have been a major activity in recent fundamental combustion research. The accomplishments are reported in a total of six papers, published in leading journals.

DISTRIBUTION A: Distribution approved for public release.

**Distribution Statement**

This is block 12 on the SF298 form.

Distribution A - Approved for Public Release

**Explanation for Distribution Statement**

If this is not approved for public release, please provide a short explanation. E.g., contains proprietary information.

**SF298 Form**

Please attach your SF298 form. A blank SF298 can be found [here](#). Please do not password protect or secure the PDF. The maximum file size for an SF298 is 50MB.

[CK+Law+Final+Report+AFOSR.pdf](#)

**Upload the Report Document. File must be a PDF. Please do not password protect or secure the PDF. The maximum file size for the Report Document is 50MB.**

[AFOSR+Report\\_Grant+FA9550-15-1-0338+\\_Flame+Dynamics+and+Chemistry.pdf](#)

**Upload a Report Document, if any. The maximum file size for the Report Document is 50MB.**

**Archival Publications (published) during reporting period:**

1. "Autoignition-affected stabilization of laminar nonpremixed DME/air coflow flames," by Sili Deng, Peng Zhao, Michael E. Mueller and Chung K. Law, Combustion and Flame, Vol. 162, pp. 3437-3445 (2015).
2. "Stabilization of laminar nonpremixed DME/air coflow flames at elevated temperatures and pressures," by Sili Deng, Peng Zhao, Michael E. Mueller and Chung K. Law, Combustion and Flame, Vol. 162, pp. 4471-4478 (2015).
3. "Flame dynamics in oscillating flows under autoignitive conditions," by Sili Deng, Peng Zhao, Michael E. Mueller and Chung K. Law, Combustion and Flame, Vol. 168, pp. 75-82 (2016).
4. "Coupling of harmonic flow oscillations to combustion instability in premixed segments of triple flames," by Vyacheslav Akkerman and Chung K. Law, Combustion and Flame, Vol. 172, pp. 342-348 (2016).
5. "Initiation and propagation of laminar premixed cool flames," by Peng Zhao, Wenkai Liang, Sili Deng and Chung K. Law, Fuel, Vol. 166, pp. 477-487 (2016).
6. "Ignition and extinction of strained nonpremixed cool flames at elevated pressures," by Sili Deng, Dong Han and Chung K. Law, Combustion and Flame, Vol. 176, pp. 143-150 (2017).

**New discoveries, inventions, or patent disclosures:**

**Do you have any discoveries, inventions, or patent disclosures to report for this period?**

No

**Please describe and include any notable dates**

**Do you plan to pursue a claim for personal or organizational intellectual property?**

**Changes in research objectives (if any):**

**Change in AFOSR Program Officer, if any:**

**Extensions granted or milestones slipped, if any:**

**AFOSR LRIR Number**

**LRIR Title**

**Reporting Period**

**Laboratory Task Manager**

**Program Officer**

**Research Objectives**

**Technical Summary**

**Funding Summary by Cost Category (by FY, \$K)**

	Starting FY	FY+1	FY+2
Salary			
Equipment/Facilities			
Supplies			
Total			

**Report Document**

**Report Document - Text Analysis**

**Report Document - Text Analysis**

**Appendix Documents**

**2. Thank You**

**E-mail user**

Dec 22, 2016 14:01:00 Success: Email Sent to: cklaw@princeton.edu